Iowa Research Online
The University of Iowa's Institutional Repository

University of Iowa
Iowa Research Online

Theses and Dissertations

Spring 2012

An analytic approach to tensor scale with efficient computational solution and applications to medical imaging

Ziyue Xu
University of Iowa

Copyright 2012 Ziyue Xu

This dissertation is available at Iowa Research Online: http://ir.uiowa.edu/etd/3016

Recommended Citation
Xu, Ziyue. "An analytic approach to tensor scale with efficient computational solution and applications to medical imaging." PhD (Doctor of Philosophy) thesis, University of Iowa, 2012.
http://ir.uiowa.edu/etd/3016.

Follow this and additional works at: http://ir.uiowa.edu/etd

Part of the Electrical and Computer Engineering Commons

AN ANALYTIC APPROACH TO TENSOR SCALE WITH EFFICIENT COMPUTATIONAL SOLUTION AND APPLICATIONS TO MEDICAL IMAGING

by

Ziyue Xu

An Abstract

Of a thesis submitted in partial fulfillment
of the requirements for the Doctor of
Philosophy degree in Electrical and Computer Engineering
in the Graduate College of
The University of Iowa

May 2012

Thesis Supervisor: Associate Professor Punam K. Saha

ABSTRACT

Scale is a widely used notion in medical image analysis that evolved in the form of scale-space theory where the key idea is to represent and analyze an image at various resolutions. Recently, a notion of local morphometric scale referred to as “tensor scale” was introduced using an ellipsoidal model that yields a unified representation of structure size, orientation and anisotropy. In the previous work, tensor scale was described using a 2-D algorithmic approach and a precise analytic definition was missing. Also, with previous framework, 3-D application is not practical due to computational complexity.

The overall aim of the Ph.D. research is to establish an analytic definition of tensor scale in *n*-dimensional (*n*-D) images, to develop an efficient computational solution for 2- and 3-D images and to investigate its role in various medical imaging applications including image interpolation, filtering, and segmentation.

Firstly, an analytic definition of tensor scale for *n*-D images consisting of objects formed by pseudo-Riemannian partitioning manifolds has been formulated. Tensor scale captures contextual structural information which is useful in local structure-adaptive anisotropic parameter control and local structure description for object/image matching. Therefore, it is helpful in a wide range of medical imaging algorithms and applications.

Secondly, an efficient computational solution of tensor scale for 2- and 3-D images has been developed. The algorithm has combined Euclidean distance transform and several novel differential geometric approaches. The accuracy of the algorithm has been verified on both geometric phantoms and real images compared to the theoretical results generated using brute-force method. Also, a matrix representation has been derived facilitating several operations including tensor field smoothing to capture larger contextual knowledge.

Thirdly, an inter-slice interpolation algorithm using 2-D tensor scale information of adjacent slices has been developed to determine the interpolation line at each image

location in a gray level image. Experimental results have established the superiority of the tensor scale based interpolation method as compared to existing interpolation algorithms.

Fourthly, an anisotropic diffusion filtering algorithm based on tensor scale has been developed. The method made use of tensor scale to design the conductance function for diffusion process so that along structure diffusion is encouraged and boundary sharpness is preserved. The performance has been tested on phantoms and medical images at various noise levels and the results were quantitatively compared with conventional gradient and structure tensor based algorithms. The experimental results formed are quite encouraging.

Also, a tensor scale based *n*-linear interpolation method has been developed where the weights of neighbors were locally tuned based on local structure size and orientation. The method has been applied on several phantom and real images and the performance has been evaluated in comparison with standard linear interpolation and windowed Sinc interpolation methods. Experimental results have shown that the method helps to generate more precise structure boundaries without causing ringing artifacts.

Finally, a new anisotropic constrained region growing method locally controlled by tensor scale has been developed for vessel segmentation that encourages axial region growing while arresting cross-structure leaking. The method has been successfully applied on several non-contrast pulmonary CT images. The accuracy of the new method has been evaluated using manually selection and the results found are very promising.

Abstract Approved: _____
Thesis Supervisor

_____
Title and Department

_____
Date

AN ANALYTIC APPROACH TO TENSOR SCALE WITH EFFICIENT COMPUTATIONAL SOLUTION AND APPLICATIONS TO MEDICAL IMAGING

by

Ziyue Xu

A thesis submitted in partial fulfillment
of the requirements for the Doctor of
Philosophy degree in Electrical and Computer Engineering
in the Graduate College of
The University of Iowa

May 2012

Thesis Supervisor: Associate Professor Punam K. Saha

Graduate College
The University of Iowa
Iowa City, Iowa

CERTIFICATE OF APPROVAL

PH.D. THESIS

This is to certify that the Ph.D. thesis of

Ziyue Xu

has been approved by the Examining Committee
for the thesis requirement for the Doctor of Philosophy
degree in Electrical and Computer Engineering at the May 2012 graduation.

Thesis Committee: _____
Punam K. Saha, Thesis Supervisor

_____
Milan Sonka

_____
Joseph M. Reinhardt

_____
Xiaodong Wu

_____
Mona K. Garvin

ACKNOWLEDGMENTS

The journey of life has always been a mystery to me. It is my great fortune to come to the University of Iowa and met the outstanding people here, and I heartily appreciate all the help, advice and guidance they endowed me.

First of all, I would like to thank my advisor, Dr. Punam K. Saha, for the guidance, encouragement and support throughout the five years of my Ph.D. study. The invaluable insights, in-depth knowledge and excellent mentorship have greatly promoted my study and research, and will continue inspiring me in my future career. I greatly appreciate the help and efforts he gave me and I am touched by his carefulness and patience. It is my great honor to have this opportunity working under his instruction.

I would also like to give my hearty gratitude to Dr. Milan Sonka who has always been a significant help for his valuable suggestions and consistent support, especially at the most critical time when I first entered the realm of medical image processing and analysis. Knowledge gained from his lectures and discussions has paved my road over the path of research.

Special thanks also go to Dr. Joseph M. Reinhardt who provided valuable instructions on the research projects and has always been supportive to me. Also I deeply appreciate Dr. Soura Dasgupta for his suggestions on our paper, and Dr. Eric Hoffman for sharing the data for the study.

I cordially appreciate Dr. Xiaodong Wu and Dr. Mona K. Garvin for serving on my defense committee and providing me valuable suggestions. Moreover, I would like to give my thanks to all the faculties for their brilliant courses I attended in the Department of Electrical and Computer Engineering and other departments.

Sincere acknowledgement goes to all my lab members, Zhiyun Gao, Yinxiao Liu, Guoyuan Liang, Yan Xu, Weichen Gao, Cheng Li, Dakai Jin, Cheng Chen and other colleagues Qi Song, Kunlin Cao, Ying Wei, Mingqing Chen, Honghai Zhang, Shanhui

Sun, Ping Yu and Cheng Zhang. I cherish the memory of the wonderful life with them during the five years.

I would also like to thank the department secretary Catherine Kern and the administrative assistant Dina Blanc for their patient assistance.

Most of all thanks are for my fiancée Rong Wang for her love, encouragement and support, and last but not least, I would take this opportunity to thank my parents and other family members. It is impossible for me to go this far without their love and support.

This work has been partially supported by internal funds from the Departments of Radiology and Electrical & Computer Engineering at the University of Iowa and the NIH grant R01 AR054439

ABSTRACT

Scale is a widely used notion in medical image analysis that evolved in the form of scale-space theory where the key idea is to represent and analyze an image at various resolutions. Recently, a notion of local morphometric scale referred to as “tensor scale” was introduced using an ellipsoidal model that yields a unified representation of structure size, orientation and anisotropy. In the previous work, tensor scale was described using a 2-D algorithmic approach and a precise analytic definition was missing. Also, with previous framework, 3-D application is not practical due to computational complexity.

The overall aim of the Ph.D. research is to establish an analytic definition of tensor scale in *n*-dimensional (*n*-D) images, to develop an efficient computational solution for 2- and 3-D images and to investigate its role in various medical imaging applications including image interpolation, filtering, and segmentation.

Firstly, an analytic definition of tensor scale for *n*-D images consisting of objects formed by pseudo-Riemannian partitioning manifolds has been formulated. Tensor scale captures contextual structural information which is useful in local structure-adaptive anisotropic parameter control and local structure description for object/image matching. Therefore, it is helpful in a wide range of medical imaging algorithms and applications.

Secondly, an efficient computational solution of tensor scale for 2- and 3-D images has been developed. The algorithm has combined Euclidean distance transform and several novel differential geometric approaches. The accuracy of the algorithm has been verified on both geometric phantoms and real images compared to the theoretical results generated using brute-force method. Also, a matrix representation has been derived facilitating several operations including tensor field smoothing to capture larger contextual knowledge.

Thirdly, an inter-slice interpolation algorithm using 2-D tensor scale information of adjacent slices has been developed to determine the interpolation line at each image

location in a gray level image. Experimental results have established the superiority of the tensor scale based interpolation method as compared to existing interpolation algorithms.

Fourthly, an anisotropic diffusion filtering algorithm based on tensor scale has been developed. The method made use of tensor scale to design the conductance function for diffusion process so that along structure diffusion is encouraged and boundary sharpness is preserved. The performance has been tested on phantoms and medical images at various noise levels and the results were quantitatively compared with conventional gradient and structure tensor based algorithms. The experimental results formed are quite encouraging.

Also, a tensor scale based *n*-linear interpolation method has been developed where the weights of neighbors were locally tuned based on local structure size and orientation. The method has been applied on several phantom and real images and the performance has been evaluated in comparison with standard linear interpolation and windowed Sinc interpolation methods. Experimental results have shown that the method helps to generate more precise structure boundaries without causing ringing artifacts.

Finally, a new anisotropic constrained region growing method locally controlled by tensor scale has been developed for vessel segmentation that encourages axial region growing while arresting cross-structure leaking. The method has been successfully applied on several non-contrast pulmonary CT images. The accuracy of the new method has been evaluated using manually selection and the results found are very promising.

TABLE OF CONTENTS

LIST OF TABLES viii

LIST OF FIGURES ix

CHAPTER 1 INTRODUCTION 1

1.1 Introduction and Project Definition 1
1.2 Literature Survey 5
1.2.1 Scale-space Theory and Tensor Scale 5
1.2.2 Curvature Analysis 7
1.2.3 Image Interpolation 9
1.2.4 Image Filtering 11
1.2.5 Fuzzy Region Growing and Image Segmentation 13
1.3 Organization of the Thesis 15

CHAPTER 2 ANALYTIC DEFINITION TO TENSOR SCALE AND EFFICIENT COMPUTATIONAL ALGORITHM 17

2.1 Introduction 17
2.2 Analytic Definition of Tensor Scale 17
2.3 Computational Solution 20
2.3.1 Edge Detection and Distance Transform Computation 21
2.3.2 Tensor Scale Computation 23
2.3.3 Tensor Scale Smoothing 27
2.3.4 Direct Implementation of the Analytic Definition 28
2.4 Experimental Methods and Results 29
2.4.1 Robustness 31
2.4.2 Accuracy 34
2.4.3 Efficiency 38
2.5 Conclusion 39

CHAPTER 3 TENSOR SCALE BASED INTER-SLICE INTERPOLATION 40
3.1 Introduction 40
3.2 Tensor Scale Based Inter-Slice Interpolation 40
3.2.1 Computation of Normal Vectors Using Tensor Scale 42
3.2.2 Interpolation Algorithm 44
3.2.3 Algorithm Challenges and Their Solutions 47
3.3 Experimental Methods and Results 50
3.4 Conclusion 60

CHAPTER 4 TENSOR SCALE BASED DIFFUSION IMAGE FILTERING 61

4.1 Introduction 61
4.2 Tensor Scale Based Diffusion Filtering 61
4.2.1 Anisotropic Diffusion Filtering 61
4.2.2 Tensor Scale Based Conductance 63
4.3 Experimental Methods and Results 65
4.4 Conclusion 73

CHAPTER 5 TENSOR SCALE BASED *N*-LINEAR INTERPOLATION 74

5.1 Introduction.....74
5.2 Tensor Scale Based *n*-linear Image Interpolation 74
5.3 Experimental Methods and Results.....76
5.4 Conclusion 81

CHAPTER 6 TENSOR SCALE BASED ANISOTROPIC REGION GROWING 83

6.1 Introduction.....83
6.2 Tensor Scale Based Anisotropic Region Growing.....83
6.2.1 Fuzzy connectedness Based Region Growing.....84
6.2.2 Tensor Scale Based Anisotropic Fuzzy Region Growing.....86
6.2.3 Vessel Enhancement and Automatic Seeding 89
6.3 Experimental Methods and Results.....91
6.4 Conclusion 97

CHAPTER 7 CONCLUSION AND FUTURE DIRECTIONS.....98

7.1 Conclusion 98
7.2 Future Directions.....100
7.2.1 Tensor Scale Based Features in Computer Vision Applications.....100
7.2.2 Tensor Scale Based Shape Analysis Algorithms.....103
7.2.3 Tensor Scale Based Similarity Measurements for Image Registration 104

REFERENCES.....106

LIST OF TABLES

Table 1 Performance of tensor scale computation algorithm based on analytic definition at various levels of noise and blurring. 32

Table 2 Comparison between the performance of the analytic and algorithmic tensor scale computation algorithms at various levels of noise and blurring. 33

Table 3 Performance of the 3-D tensor scale computation algorithm based on analytic definition at various levels of noise and blurring. 38

Table 4 Results of quantitative comparison among three different methods in terms of residual noise after filtering on different images. 71

Table 5 Results of quantitative comparison among three different methods in terms of relative contrast after filtering on 3-D phantom image. 72

Table 6 Results of accuracy analyses of vessel segmentation by the two methods. 96

LIST OF FIGURES

Figure 1 A schematic description of tensor scale computation. The method starts with edge locations (blue and yellow dots) on sample lines emanating from the candidate image point (red dot). Following the axial symmetry of an ellipse, the edge points on each pair of radially opposite sample lines are repositioned (yellow dots to green dots). Finally, tensor scale ellipse is computed from repositioned edge points (green and blue dots). 6

Figure 2 An illustration of tensor scale using a rabbit femur bone surface (dark off-white) forming a 2-D manifold m_1. The candidate spel p is shown as a red dot; the point on m_1 closest to p gives the primary tensor vector $\boldsymbol{\tau}_1(p)$ (red). The orthogonal complement plane $W_1^{\perp}$ and the 1-D manifold $W_1^{\perp} \cap m_1$ are shown in blue and cyan, respectively. Secondary tensor vector $\boldsymbol{\tau}_2(p)$ is defined by the point on $W_1^{\perp} \cap m_1$ closest to p; finally, $\boldsymbol{\tau}_3(p)$ is given by the closest point on $W_1^{\perp} \cap m_1$ along the line orthogonal to $\boldsymbol{\tau}_2(p)$. It may be noted that projections of the two lines (dotted yellow and green) on m_1 along $\boldsymbol{\tau}_1(p)$ provide principal directions of m_1 at r, the meeting location with $\boldsymbol{\tau}_1(p)$; this idea is used in our computational solution in 3-D. 18

Figure 3 Illustration of different patterns of sign alteration of LoG values $2 \times 2 \times 2$ neighborhood. Spels in a $2 \times 2 \times 2$ neighborhood are marked with $\pm$ or $\mp$ (light gray) indicating that if the sign of LoG for spels marked with $\pm$ is positive then that for spels marked with $\mp$ is negative or vice versa. (a) All possible geometric classes of sign alterations with a valid zero crossing of LoG. (b) A few examples of sign alterations without a zero crossing of LoG. 22

Figure 4 Illustration of the scheme for locating target manifold along specified direction. (a) Distance and primary vector information is investigated at sample points $p + i\Delta_{L_p}$ on a line L_p. (b) Sample point is considered as sufficiently close to the target manifold if distance transform value is sufficiently small and the angular difference for primary vector with its successor is greater than a preset threshold. 24

Figure 5 Illustration of the computation of secondary t- vector $\boldsymbol{\tau}_2(p)$ in 3-D. (a) A partitioning surface with primary t-vector $\boldsymbol{\tau}_1(p)$ (black) and $\boldsymbol{\tau}_1(q)$ (green) for several qs (green dots) in the neighborhood of p (black dot). (b) Projection vectors $\boldsymbol{\tau}_1'(q)$ of normalized vectors $\boldsymbol{\tau}_1(q)/|\boldsymbol{\tau}_1(q)|$ on P along with the curve at the intersection of P and the partitioning surface. (c) Computation of principal directions using $\boldsymbol{\tau}_1'(q)$ (solid) and $-\boldsymbol{\tau}_1'(q)$ (dotted). (d) Projection of principal directions onto partitioning surfaces. 26

Figure 6 Results of tensor scale computation. (a) A 2-D image slice from the BrainWeb MR brain phantom data. (b) Computed edge locations (red) and gray scale distance transform. (c) A color coded illustration of 2-D tensor scale. (d) Color coding disk at full intensity. (e-g) Same as (a-c) but for 3-D tensor scale computation. Results are shown on one image slice; see text for further explanation. (h-j) Same as (e-g) but from another view. 30

Figure 7 Results of 2-D phantom image computation. (a) An original phantom image (2) Tensor scale result produced by algorithmic method. (c) Tensor scale result produced by analytic method. 34

Figure 8 Tensor scale computation result comparison between differential geometric method and spatial sampling method. (a) An original slice from BrainWeb image (2) Image after threshold showing white and grey matter that defines absolute boundary for spatial sampling methods to be considered as ground truth. (c) 3-D tensor scale computation result from spatial sampling method for (b). (d) phantom with blur and noise (e) 3-D tensor scale computation result from differential geometric method for (d). (f, g) same as (d, e) but for another level of blur and noise. 35

Figure 9 Same as Figure 8 but from another view. 36

Figure 10 Schematic descriptions of the principle of tensor scale based image interpolation. (a) Examples of normal vectors at different points inside and outside of a shape. (b) A closed form solution exists for computing the deformation vector using normal vectors. 41

Figure 11 Computation of the normal vector from local tensor scale. (a) An ambiguity in selecting the normal vector between pb and pb' – the opposite vectors along the minor axis of tensor scale. (b) This ambiguity is solved by analyzing tensor scale-derived isotropic scales along the direction of the minor axis bb'. 42

Figure 12 Intermediate results of tensor scale based image interpolation on MR brain data. (a-c) Three successive slices from the BrainWeb MR phantom data. (d,e) Normal vector fields computed from (a,c). (f) Color-coded deformation vector field computed from (d,e) on the slice plane located at the middle of the slice of (a,c). (g) Image interpolated from (a) and (c). Compare the result with (b). (h) Interpolation error computed from (b) and (g). (i) Magnitude of the deformation field. 43

Figure 13 Illustration of computing the interpolation line $l(t)$ associated with an image point p on the interpolation plane with the information from tensor scale in images of sl_A and sl_B. (a) p locates halfway between two slices. (b) Same as (a) except that p is close to the lower slice sl_B. Although, the line $l'(t)$ is same in both (a) and (b), the final interpolation line $l(t)$ is changed due to different shifts required under the two cases. Note that the point c_B is close to p_B in (b). 45

Figure 14 Illustration of tensor scale derived local structure width. (a) A binary phantom image. (b) Tensor scale-derived isotropic scale image. (c) Local structure width map. (d) Computed medialness. 47

Figure 15 A schematic description to solve ambiguities of selecting normal vectors at medial points. At a medial point p_A, there is an ambiguity of the true normal vector between $\overrightarrow{p_A a}$ and $\overrightarrow{p_A a'}$. With the assumption that a local deformation is less than half the structure width, the magnitude of the deformation using the correct correspondence of a and b must be less than that of the wrong correspondence of a' and b. Therefore, $\overrightarrow{ab}$ is selected as the correct correspondence to generate the interpolation line. 49

Figure 16 Performance of three interpolation methods on the BrainWeb phantom dataset with additive white Gaussian noise at various levels of signal-to-noise ratio. The mean error was computed as the MAD value over the entire image while the standard deviation of errors was computed as the standard deviation of $\mathrm{MAD_i}$ values from individual slices. As compared with the two registration based methods, the new method outperforms both of them except for the four cases for which the differences between the B-spline and the new method are statistically identical - marked with "NS" (non-significant). 53

Figure 17 Performance of three interpolation methods on the BrainWeb phantom dataset with different multiplicative Gaussian intensity inhomogeneity added. The mean error was computed as the MAD value over the entire image while the standard deviation of errors was computed as the standard deviation of $\mathrm{MAD_i}$ values from individual slices. $\mathrm{MAD_i}$ represents the average interpolation errors on the i-th slice for three different inhomogeneity maps at a fixed percentage of inhomogeneity. 54

Figure 18 Results of applications of different interpolation methods on the ankle CT data Ankle1. (a-c) Three consecutive image slices from the original data. (d-f) Interpolated results for the central image slice (b) from the two adjacent slices (a,c) using B-spline (d) and Demons (e) based registration methods and the tensor scale based method (f). (g-i) Absolute errors by corresponding interpolation method as computed by comparing with the original image slice. Interpolation error is reduced using the tensor scale method (p-value < 0.01).....56

Figure 19 Same as Figure 18 but for three consecutive image slices from the pulmonary CT image Lung1 at 0.5 mm slice thickness. 57

Figure 20 Same as Figure 18 but for three consecutive image slices from the lower abdominal CT image Abdomen1 at 1mm slice thickness.....58

Figure 21 Performance of three interpolation methods on sixteen different medical images selected from different clinical applications. The mean error was computed as the MAD value over the entire image while the standard deviation of errors was computed as the standard deviation of MAD_i values from individual slices. For all examples, the tensor scale based method has outperformed the two registration based methods (p-value < 0.01).....59

Figure 22 The shapes of diffusion conductance (A) and diffusion flow magnitude (B) functions, respectively, with gradient magnitudes complying with the basic idea behind anisotropic diffusion.....62

Figure 23 Behavior of the Gaussian mapping involved in the conductance function calculation: (a) controlling parameter is kept fixed over the entire image and the mapping is isotropic everywhere; (b) tensor scale controlled conductance function helps to achieve anisotropic dynamic conductance value so that the diffusion process is guided in a direction variant manner.....64

Figure 24 A qualitative comparison among different diffusion filtering methods. (a) The original digital image with natural noise. (b-d) Smooth images obtained by using gradient (b), structure tensor (c) and tensor scale (d) based diffusion filtering methods. (e-h) Zoomed in displays of the matching region cropped from (a-d), respectively. It may be noted that the tensor scale based method has outperformed the other two methods in smoothing along the structures while preserving boundaries and effect is more prominent in the zoomed displays in (e-h). 68

Figure 25 Comparative results of image filtering in a 2-D phantom. (a) The original phantom image. (b) Degraded image after adding Gaussian white noise. (c-e) Results of gradient (c), structure tensor (d) and tensor scale based (e) anisotropic diffusion filtering methods.....69

Figure 26 Results of 3-D image filtering. (a) An original image slice from a pulmonary CT image of a patient. (b) Degraded image after adding Gaussian white noise. (c-e) Results of 3-D image filtering using gradient (c), structure tensor (d) and tensor scale (e) based diffusion.....70

Figure 27 2-D illustration of tensor scale based n-linear interpolation algorithm. Conventional linear interpolation calculates the intensity at p_c based on linear distance weight so that p_1 will be assigned with the greatest weight value. From the observation, such weight leads to cross region mixing. By incorporating tensor scale, weight for p_2 and p_4 will be encouraged and smoother structure boundary will be generated. 75

Figure 28 Results of image interpolation on a phantom data. (a) An original image slice. (b) Sub-sampled image at the rate 4. (c-e) Result using standard n-linear (c), windowed Sinc (d) and tensor scale based n-linear image interpolation. (f-j) Same as (a-e) but for a zoomed part marked in (a). (k-o) Same as (a-e) but for another zoomed region. It may be observed that tensor scale helps preserving small structures and it produces smooth edges without causing ringing artifacts which is visible for result produced by the windowed Sinc method. 77

Figure 29 Results of image interpolation on the BrainWeb MR phantom image. (a) An original image slice. (b)An image slice from sub-sampled image at the rate of 3. (c-e) Results using standard n-linear (c), windowed Sinc (d) and tensor scale based n-linear (e) interpolation methods. It may be observed that tensor scale has produced crisper edges as compared to the standard n-linear interpolation without causing ringing artifact associated with the windowed Sinc method. 78

Figure 30 Performance of three interpolation methods on the different phantom and medical images selected from various clinical applications at sub-sampling rate of $2 \times 2 \times 2$. The percentage error was computed over the entire 3-D image while a paired t-test was performed based on the percentage error from individual slices. As compared with the standard n-linear and windowed Sinc methods, the tensor scale based n-linear method has outperformed the first method while comparative performance with the windowed Sinc method varies for different images. An "NS" (non-significant) mark is used to indicate statistical insignificance of difference in results by two methods. 80

Figure 31 Same as Figure 30 but for subsample rate of $3 \times 3 \times 3$.....80

Figure 32 Same as Figure 30 but for subsample rate of $4 \times 4 \times 4$.....81

Figure 33 Illustration of fuzzy connectedness computation between two points p and p_1. For affinity, points belongs to the same structure have greater value than points of different structures, which means $\mu_\kappa(p,q) > \mu_\kappa(p_1,q_1)$. There are two paths, solid and dashed is shown in the figure, based on the definition of the path strength, $\mu_\mathcal{N}(\pi_{\text{solid}}) > \mu_\mathcal{N}(\pi_{\text{dashed}})$. Finally, the fuzzy connectivity between p and p_1 is defined as the strength of the strongest 85

Figure 34 A schematic representation of a vascular tree structure in 2-D. Tensor scale at a point p is indicated by the ellipse in red. The proposed constrained region growing algorithm uses this knowledge to facilitate growth along the structure while restricting growth across the local structure to stop leaking. 86

Figure 35 An example of vessel enhancement result in (b) for a pulmonary image (a). It can be observed that we reduce undesired structures such as fissure (as shown within rectangles) and airway wall (as shown within circle) by enhancing the tubular vessel structures. 90

Figure 36 Seed points selected on part of an illustration slice. Seed points (red) locate approximately on the centerline of lung vessels. 91

Figure 37 2-D Segmentation results on an image of coral reef (a); the red dot indicates the seed. The new anisotropic region growing has captured more branches (c) as compared to the conventional algorithm (b). (d-f) Zoomed-in display of (a-c) over the regions marked by the red box in (a). 93

Figure 38 One slice in 3-D Segmentation for pulmonary CT image; as shown within the circle, one branch missed by fuzzy connectedness segmentation method without tensor scale (a) is captured by incorporating tensor scale information (b). 94

Figure 39 Results of vascular segmentation in non-contrast human pulmonary CT imaging. (a) A 2-D CT image slice with overlapped vessel segmentation result using Shikata's method. (b) Matching slice with overlapped vessel segmentation result using tensor scale (c-e) 3-D renditions of vasculature using Shikata's (c), conventional region growing (d) and the tensor scale (e) methods.. 95

Figure 40 Two retinal fundus images with different field of view to a single object ... 101

Figure 41 Features extracted from tensor scale from vessel map (a) of the original image (h): distance to edges (b), local structure size (c), local structure orientation (d), local anisotropy (e), center/edge point label (f) and convexity of distance map (g) 102

Figure 42 Correspondence between two images, a set of points are selected in (a) and their correspondent point is identified in (b). Correspondent points are then clustered for estimation of transformation between images and final result is shown in (c). 103

Figure 43 Tensor scale based shape analysis, a trabecular bone structure with rods and plates is shown in (a) and the structure evaluation result is provided in (b). 104

Figure 44 Illustrations of different shapes during deformation of a Y-like target shape (a) onto a disk (h) via an intermediate shape (e) using the tensor scale based method. Intermediate shapes during warping from (a) to (e) are shown in (b-d) while (f-g) illustrate intermediate shapes between (e) and (h). 105

CHAPTER 1

INTRODUCTION

1.1 Introduction and Project Definition

Scale is a widely used notion in medical image analysis that evolved in the form of scale-space theory [1] where the key idea is to represent and analyze an image at various resolutions. Although, the basic notion of scale-space theory is widely applicable in imaging applications [2, 3], it suffers from the lack of a scale localization that led to the evolution of the "local scale" [4-7]. Later, Saha *et al.* [8, 9] introduced local morphometric scale and recently, we have generalized it to "tensor scale" – a local morphometric scale using an ellipsoidal model that yields a unified representation of local structure size, orientation, and anisotropy. In previous works from our laboratory, tensor scale [10] was described using an algorithmic approach and a precise analytic definition was missing. Also, its computational solution in 3- or higher- dimensional images was unrealistic. The overall aim of this Ph.D. research is **to establish an analytic definition of tensor scale in *n*-Dimensional (*n*-D) images, develop an efficient computational solution and investigate its role in various medical imaging applications including image interpolation, filtering and segmentation**. The research brings contextual structural information captured by tensor scale in a wide range of medical imaging algorithms and applications, and achieves performance improvement. Two major classes of applications of tensor scale in image processing were studied – (1) local structure-adaptive anisotropic parameter control and (2) local structure descriptor in image object/image matching. The Ph.D. research project was accomplished by completing the following six specific aims:

Aim 1: Establish an analytic approach to define tensor scale in *n*-D images with objects formed by pseudo-Riemannian partitioning manifolds.

Aim 2: Develop an efficient computational algorithm for 2- and 3-D images combining Euclidean distance transform and several novel differential geometric approaches. Perform experiments to evaluate the accuracy of the computational algorithm.

Aim 3: Design and develop an inter-slice interpolation algorithm based on tensor scale. Perform experiments to evaluate the performance of the method in comparison with existing interpolation algorithms.

Aim 4: Design and develop an anisotropic diffusion filtering algorithm based on tensor scale. Perform experiments to evaluate the performance of tensor scale guided anisotropic diffusion filtering method in comparison with conventional gradient and structure tensor based diffusion filtering algorithms.

Aim 5: Design and develop a tensor scale based *n*-linear interpolation method. Perform experiments to evaluate the performance of tensor scale based interpolation method in comparison with standard linear interpolation and windowed Sinc interpolation methods.

Aim 6: Design and develop a new anisotropic constrained region growing method locally controlled by tensor scale for vessel segmentation. Perform experiments to evaluate the accuracy of tensor scale guided region growing method for vasculature segmentation.

The analytic definition and efficient computational algorithm for tensor scale has been developed and reported in [11]. We first introduce a new analytic approach to define tensor scale as a set of orthogonal vectors by modeling an image as a set of objects defined by partitioning manifolds. To compute tensor scale, a direct algorithmic realization of the analytic definition faces two fundamental challenges: (1) object partitions are not known in real images and (2) computational complexities in three- or higher-dimensions. These challenges are addressed by combining techniques involving edge detection, distance transform, and differential geometric approaches. In short, it is realistic to assume that edge points given by edge detection algorithm are dense samples

on the theoretical partitioning manifolds, and that the distance transform from these edge points is a close approximation of distance transform from partitioning manifolds. Therefore, tensor scale may be computed by using gradient analyses and computational geometric approaches to the distance transform map from edge points in an image. Efficiency and effectiveness of the tensor scale computation algorithm is examined in terms of computation time and Log-Euclidean distance [12] on phantom images with known ground truth.

Our tensor scale based slice-interpolation algorithm presents a closed form solution to determine the interpolation line at each image location in a gray level image [13]. A fundamental challenge in slice-interpolation for medical images is to determine the structure correspondence between adjacent slices to restore voxel isotropy. The challenge is met by utilizing tensor scale information of adjacent slices. The basic idea is to derive normal vector at each image location from tensor scale that yields trans-orientation of the local structure and points to the closest edge point, which are further used to compute the interpolation line using a closed form equation. The method has been applied to several medical image datasets from clinical applications and its accuracy and response to noise and other image-degrading factors have been examined and compared with those of current state-of-the-art interpolation methods.

The tensor scale based anisotropic diffusion filtering has been developed to govern the diffusion process in a space-variant and orientation-dependent fashion to optimally fit with local image structures captured in the form of tensor scale. Anisotropic diffusion [14] was originally described to encourage diffusion within a region (characterized by low intensity gradients) while discouraging it across object boundaries (characterized by high intensity gradients). The tensor scale based method uses a new approach to solve the fundamental challenge that the control parameter determining the degree of filtering is isotropic and fixed over the whole image which limits the performance of the algorithm. The performance of tensor scale based image filtering is

compared with gradient and structure tensor based diffusion filtering algorithms on several phantom and real images based on noise and structure preservation measurements.

A new tensor scale based *n*-linear interpolation method has been developed that helps to improve the performance of interpolation method. The fundamental challenge for basic *n*-linear interpolation that the weight is determined by voxel distance only, which leads to rough edges and mixing. Tensor scale based approach addresses this problem by bringing the notion of an anisotropic space where distance increases slower along the direction of the local structure while it increases faster in the cross-structure direction. The performance of tensor scale based *n*-linear image interpolation method is examined and compared with standard linear and windowed Sinc interpolation method using a 3-D phantom and a set of medical images selected from different applications.

Our vascular segmentation algorithm is based on the region growing technique [8, 15-20]. The algorithm constructs the segmentation result with initial seeds on pulmonary vasculature. A fundamental challenge in region growing techniques for segmenting vascular structures is that, the continuity of structures are often broken by noise and artifacts especially at finer scales. For human experts, on the other hand, the continuity can be reconstructed using local structure geometry. Our method solves this problem using the local structure orientation and geometry information captured by tensor scale. The basic idea behind our method is to facilitate region growing along a structure while restricting the growth across it. This method models an anisotropic fuzzy region growing process using tensor scale, and its performance is tested on a set of human non-contrast pulmonary CT image.

The proposed Ph.D. research project involves research works related to the following major areas – (1) scale-space theory and multi-scale approaches, (2) curvature analysis, (3) image interpolation, (4) image filtering, and (5) fuzzy region growing and image segmentation. In the following section, a brief literature survey on each of the

above research topics is presented with emphasis on the contribution from the current research study.

1.2 Literature Survey

1.2.1 Scale-space Theory and Tensor Scale

Scale [21-23] may be thought of as the spatial resolution, or, more generally, a range of resolutions needed to ensure a sufficient yet compact representation of target information [21]. Scale plays an important role in image processing applications. It is useful in determining the optimum trade-off between noise smoothing and perception/detection of structures, and is also helpful in breaking a computer vision and image processing task into a hierarchy of tasks where tasks at higher levels deal with larger structures. Witkin [22] and Koenderink [23] mathematically formulated the concept of scale in the form of scale-space theory. Discrete scale-space representations [24] have been used in several imaging applications including segmentation [25], clustering [26], classification [27], and structural analysis [28]. Although, scale-space image representations have provided significant insight, it is not obvious – (1) how to unify the information from images at different scales, and (2) how to identify the optimal scale at each individual image point. A knowledge of "local scale" [4-7] would allow us to spatially tune the neighborhood size in different processes leading to selection of small neighborhoods in regions containing fine detail or near an object boundary, versus large neighborhoods in deep interiors [8]. Also, local scale would be useful in developing an effective space-variant parameter controlling strategies [9].

The notion of local morphometric scale was introduced using a spherical model in [8, 9] and was applied to different image processing algorithms, see [10] for a survey on local scale. Although the preliminary results have demonstrated effectiveness of this notion of local scale in different image processing applications, a major limitation of the spherical model is that it ignores orientation and anisotropy of local structures. Recently,

we [10] proposed a new local morphometric scale, called “tensor scale” using an ellipsoidal model which gives a unified local parametric representation of structure size, orientation, and anisotropy. The algorithmic definition is shown in Figure 1. At every point in an image, tensor scale is defined as the largest ellipse centered at the candidate point within the homogenous region around it. The algorithm first locates edge on sample lines, then repositions the edge points following the axial symmetry of an ellipse, and finally fits an ellipse to the repositioned edge points, which defines tensor scale.

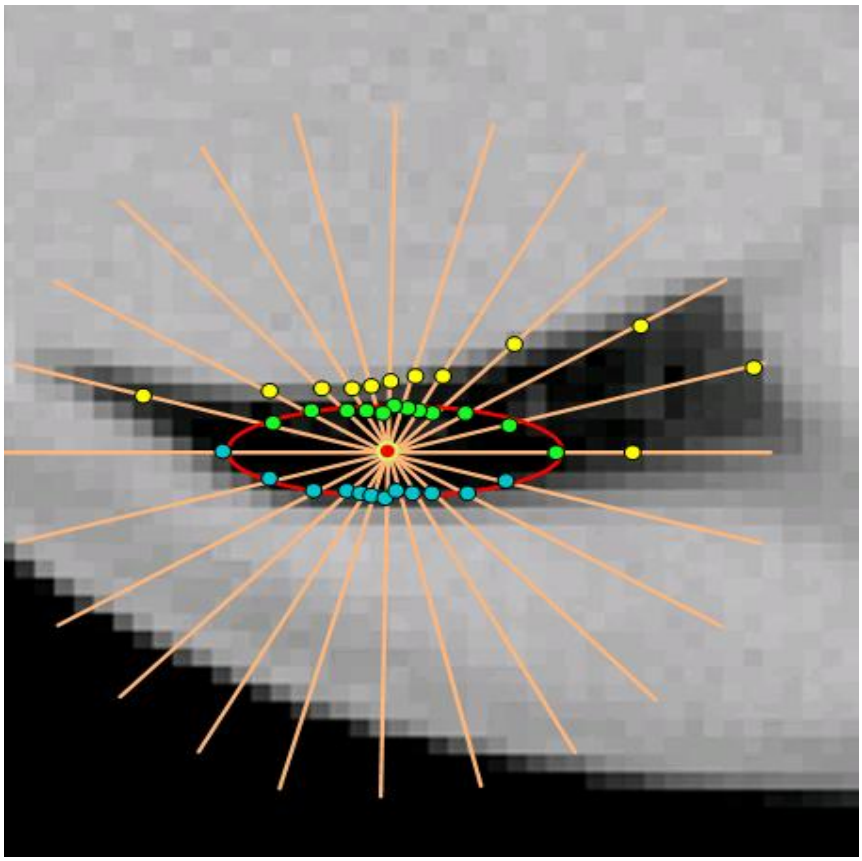

Figure 1 A schematic description of tensor scale computation. The method starts with edge locations (blue and yellow dots) on sample lines emanating from the candidate image point (red dot). Following the axial symmetry of an ellipse, the edge points on each pair of radially opposite sample lines are repositioned (yellow dots to green dots). Finally, tensor scale ellipse is computed from repositioned edge points (green and blue dots).

Tensor scale is a valuable feature associated with every image point and is potentially useful in several image processing and computer vision applications, especially the medical imaging applications where local structural and scale information may play important roles. A few works have been reported on representing local orientation using gradient structure tensor [29] and its applications have been demonstrated in image filtering [29] and adaptive image morphological analysis [30]. Although, structure tensor is a useful concept and efficiently provides orientation information near edges, it primarily captures information derived from local gradient field and may not directly relate to local structure geometry that yields shape and size or thickness information. For example, in a homogeneous region, structure tensor may not carry meaningful information related to local structure. We formulate tensor scale from a geometric perspective where, at each image point, the tensor scale captures information related to local structure geometry.

Effectiveness of tensor scale in image segmentation [31], registration [32], filtering [10] and also in quantifying local morphometry in complex quasi random networks of trabecular bone [33, 34] have been studied. Andalo [35, 36] presented an efficient computational solution for tensor scale and demonstrated its usefulness in detecting salient points on a given contour.

1.2.2 Curvature Analysis

Curvature refers to multiple related concepts in different areas of geometry. Intuitively in the context of curve/surface embedded in a Euclidean space, curvature at a point is the amount by which the local object deviates from being straight/flat. From differential geometry [37], curvature provides fundamental information for local shape. The notion of curvature is one of the most powerful tools in representing object and interpreting structure in an image and of great importance in many computer vision and image processing applications.

Riggs [38] investigated the potential of curvature for human visual system in perception of structure, specifically, to divide contours to meaningful segments. Parent [39] showed that tangent and curvature information are sufficient in estimation of local models for a curve and recovery of its trace. Kehtarnavaz [40] presented a scheme for 3-D contour segmentation using curvature and torsion. The application of curvature in segmentation is further studied by others: Trucco [41] studied range image segmentation system that partitions range data to homogeneous surface patches using mean and Gaussian curvatures; Zana [42] presented an algorithm based on mathematical morphology and curvature evaluation for detection of vessel-like patterns which are common in medical images; and Soldea [43] developed a method to globally segment volumetric images into regions that contain elliptic iso-surfaces v.s. regions with hyperbolic iso-surfaces relying on globally compute, bound and analyze the Gaussian and mean curvatures. Curvature is also useful in signal filtering. Hodson [44] proposed an adaptive filtering technique for smoothing noisy sampled data to reduce the distortion of the information content with Gaussian kernels, and local curvature was estimated for determining Gaussian width. In [45], El-Fallah developed an inhomogeneous diffusion algorithm by representing the image as a surface and evolving it according to its mean curvature. For specific task of vessel enhancement, Chapman [46] evaluated the use of voxel intensity curvature measurements to enhance vessels in 3-D MRA images. As an important feature extracted from the image, curvature can be applied in object recognition and image registration. Goldgof [47] used curvature profile for extraction special points on terrain which were further utilized for recognition of particular regions of the terrain. Mokhtarian [48] developed an isolated object recognition system which is robust with respect to scale, position and orientation changes with curvature scale space representation. Shi [49] studied the use of curvature of the gray scale character image to improve the accuracy of handwritten numeral recognition. Friets [50] provided an alternative to the use of fiducials for the registration of a patient’s head position during

surgery with diagnostic images from computed tomography (CT) or magnetic resonance imaging (MRI). In [51], Fischer developed a fully automated, non-rigid image registration algorithm based on minimizing a measure subject to a curvature based constraint.

Multiple methods exist in estimating curvature by employing several different representations. Most intuitive way is to fit an analytic surface to the neighborhood of the candidate point and evaluate its second derivative to get curvature estimation. The fitting algorithm varies from least squares error with orthogonal polynomials [52], linear regression [53] and spline-based approximation [54]. Discrete methods exist measuring the change in the normal within neighborhood and Flynn [55] gave an overview and evaluation of these approaches. Contemporary research focuses mainly on polygonal meshes. Symmetric matrix was defined integrating the normal curvature around each vertex in [56], in this work, the neighborhood points were used to approximate the curvatures. Further, for input data with high noise, techniques computing the sign and direction of principal curvatures are employed [57]. In our work, we utilize the curvature analysis theory in determining the directions of principal curvatures on a surface that relate to the max/min change of the normal vectors. Meanwhile, we investigate the information of the curvature value that contributes to local structure size.

1.2.3 Image Interpolation

Image interpolation has many applications in computer vision, medical imaging and image processing tasks. For medical imaging tasks, it is often necessary for image generation and further processing. Image reconstruction for CT or MRI uses interpolation techniques in discrete back projection for inverse Radon transform. After acquisition, zooming or rotating is often performed for diagnosis. Further, interpolation is needed in resampling which is desired for multiple image manipulations including registration and compression. Simple algorithms such as nearest neighbour and linear interpolation are

widely used from early ages till now for their simplicity. The Sinc function is considered ideal based on information theory introduced by Shannon, whereas Taylor or Lagrange polynomial approximations are usually applied in real applications due to infinite impulse response (IIR) nature of Sinc function. Later, different spline functions are used for their computational efficiency. Unser [58] described efficient algorithms for continuous representation of a discrete signal in B-splines. Lehmann [59] provided a comparison among the methods of truncated and windowed Sinc, nearest neighbor, linear, quadratic, cubic B-spline, cubic, Lagrange and Gaussian interpolation techniques.

Medical images are commonly collected and thus represented as stacks of slices. Often, slice thickness is larger than in-plane resolution leading to anisotropic voxels. Moreover, spacing between slices may even not be the same among all slice. However, isotropic data commonly facilitates most image visualization, manipulation and analysis tasks and re-discretization is needed in circumstances such as multi-modality registration where for the same object of study, data sets are often different in their resolution. Therefore, inter-slice image interpolation has become a popular and indispensable processing step to restore voxel isotropy and to generate image with the desired resolution for medical images.

Medical image interpolation techniques may be classified into two groups [60]: (1) image-based and (2) object-based methods. Image-based interpolation approaches including nearest neighbor, linear and spline interpolation methods are primarily based on local image intensities in adjacent slices and require no structural correspondence between two slices. Herman [61] reported on experimental study comparing linear and cubic spline interpolation methods in mathematical properties as well as performance in reconstruction and efficiency. Stytz [62] discussed the use of kriging for interpolation in 3-D medical image surface rendering and slice interpolation. Although image-based techniques are computationally faster, such methods often suffer from several artifacts caused by nonlinear structural deformities in the slice direction. On the other hand,

object-based interpolation techniques determine point-wise structural deformation in successive slices to capture structural alterations in the slice direction. The primary difference among algorithms within this group is essentially in the method of building structural correspondence between successive slices. Many methods were proposed in this category. As one example, shape-based interpolation scheme for multidimensional image was discussed by Raya [63] in the motivation of saving user time in segmentation process in which an image is first segmented then interpolated. Similar procedure was studied by others. Herman [64] provided a generalization of the chamfer distance calculation and evaluated the performance of several variants of the method. Higgins [65] studied application of shape-based interpolation method in tree-like structures such as the coronary arteries in which case the low slice resolution problem is particularly acute. The method was later generalized from binary objects to grey-level scenes by Grevera in [66] where scene was treated as an object in a higher-dimensional space. Lee [67, 68] proposed a morphology-based algorithm to interpolate and improved the shape based method by integrating feature line-segments to guide the process for better shape interpolation. Penney [69] presented a method establishing spatial correspondence between adjacent slices using non-rigid registration algorithm. In our work, we utilize the structure information in tensor scale to build correspondence and the performance is evaluated in comparison of state-of-the-art methods.

1.2.4 Image Filtering

The theory of anisotropic diffusion was originally proposed by Perona and Malik [14]. It was described to encourage diffusion within a region (characterized by low intensity gradients) while discouraging it across object boundaries (characterized by high intensity gradients). The aim is to reduce noise while preserving edges, lines and detailed parts of the image that are important for image interpretation. Subsequently, the theory was studied by others. Gerig [70] applied anisotropic diffusion in MRI data postprocess,

supporting 3-D and multi-echo MRI and demonstrated efficient noise reduction and sharpening of object boundaries. Luo [71] presented an approach that derived the threshold for the conductance function from local geometry of image and applied it to simulated single photon emission computed tomography (SPECT) images. Sapiro [72] built a general framework for anisotropic diffusion of multivalued images and applied it to color images. Parker [73] investigated the use of entropy in determining local pixel intensity regularity that further measures image structure. Weickert introduced a non-linear diffusion filter based on structure tensor in [74] to enhance flow-like structure, he also gave an overview for variations of anisotropic diffusion methods and application in image processing in [29]. Frangakis [75] assessed the signal reconstruction performance of the anisotropic filtering and wavelet filtering on multi-dimensional biomedical data. Saha [9] introduced a scale based filtering method using local structure size to arrest smoothing around fine structures.

Anisotropic diffusion filtering has been applied in multiple applications and modalities. Ford [76] applied anisotropic diffusion as a directional smoothing technique that preserves structure in resampling. Orkisz [77] recovered small low-intensity vessels in magnetic resonance angiography images with a nonlinear spatial filtering technique based on anisotropic diffusion. You [78] developed an anisotropic regularization technique for blind restoration of blurred images. The technique adapted both degree and direction of regularization to structures in the image and consequently produced good restoration quality. Atzori [79] proposed an adaptive anisotropic filter aiming to unify different sources of perceptive distortion in MPEG sequences and to enhance visual quality. Demirkaya [80] made use of anisotropic diffusion filtering in smoothing the PET attenuation data to reduce random noise and streak artifacts. Miao [81] integrated adaptive anisotropic diffusion in Monte Carlo method for radiotherapy dose calculation. The dose distribution was smoothed according to local statistical noise levels. Yu [82] investigated a diffusion method for ultrasonic and radar imaging applications where

speckle noise rather than additive noise presented. In [83], anisotropic diffusion was used to smooth ultrasound images and extract an initial pre-segmentation of breast tumors for the active contour technique. Krissian [84] provided a new filtering method to remove Rician noise from MRI images. The standard deviation of the noise was robustly estimated by the filter. Local linear minimum mean square error filters and partial differential equations for MRI were combined. Xu [85] presented an efficient smoothing algorithm for reducing noise in diffusion tensor images and improved the accuracy of structural and architectural characterization of living tissue. Rodrigues [86] applied anisotropic filtering to suppress Poisson noise in fluorescence confocal microscopy images by considering different spatial and temporal correlations.

In our work, we use geometric information of local structures from tensor scale to control the conductance parameter in filtering that facilitates along-structure smoothing while preserving boundary sharpness.

1.2.5 Fuzzy Region Growing and Image Segmentation

Segmentation has remained a salient task in most imaging applications, in particular, those involving object classification, geometry, shape, and motion analysis. Despite major advances in imaging science, image quality as well as resolution is often limited, particularly in medical imaging, posing further challenges to image segmentation. Several segmentation approaches, including manual outlining [87], boundary based [88, 89], regio*n*-based [90], and shape and model-based [91, 92] techniques have been introduced and subsequently modified and investigated in different applications.

Rosenfeld introduced the notion of fuzzy geometry and topology in the context of image processing and pattern recognition [18, 19]. He defined several geometric and topologic concepts in a fuzzy digital image including adjacency, separation, and connectedness. More recently, Buckley [93] have formulated some fundamental definitions related to fuzzy lines and planar geometry using the notion of a fuzzy point

and have studied their properties. In our current research, we primarily use fuzzy geometric and topology features related to distance and connectedness. The notion of the degree of connectedness between two image pixels/voxels was first introduced by Rosenfeld in the context of studying the topology and geometry of fuzzy images. Rosenfeld's degree of connectedness was further studied to understand the topological, geometrical, and morphological properties of fuzzy subsets [19]. Dellepiane [94, 95] and Udupa [20] were the first to suggest the use of fuzzy connectedness in image segmentation. Udupa introduced a different framework for fuzzy connectedness bringing in a key concept of a local fuzzy relation called affinity on image voxels to capture their local hanging-togetherness. They showed how affinity can incorporate various image features in defining fuzzy connectedness, presented a general framework for the theory of fuzzy connectedness, and demonstrated how dynamic programming can be utilized to bring the otherwise seemingly intractable notion of fuzzy connectedness into segmentation. Saha [8, 96-98] further advanced the theory of fuzzy connectedness considerably, bringing in notions of scale [8] and iterative relative fuzzy connectedness [96, 97] which was further extended by Herman [99]. Saha [98] axiomatically proved that the basic min-max construct used in fuzzy connectedness is the only possible formulation and studied the issue of how to construct effective affinities and the use of local scale for this purpose. Aspects related to the computational efficiency of fuzzy connectedness algorithms have also been studied [100, 101]. The fuzzy connectedness methods have been utilized for image segmentation extensively in several applications, including multiple sclerosis lesion quantification [102-107], late life depression [108, 109], MR angiography [110, 111], CT angiography [112, 113], breast density quantification via mammograms [114].

Our presented methods are essentially designed and built using various notions of fuzzy geometry and topology. It is based on the region growing technique [8, 15-20] initiated with a set of seeds. A fundamental challenge faced in a region growing

technique for tracing vascular structures, especially at finer scales, is that the continuity of structures are often broken by noise and other imaging artifacts at in vivo imaging regime. However, a human expert may reconstruct the continuity using local structure geometry of vascular tree. Our method solves this fundamental problem using tensor scale that captures local structure orientation and geometry. A new anisotropic constrained region growing algorithm is formulated that combines tensor scale with fuzzy connectedness which facilitats region growth along local structure while arresting cross-structure leakages.

1.3 Organization of the Thesis

The thesis is organized as follows.

- **Chapter 1:** In this chapter, an overview of the specific aims and the proposed methods is presented. Also, the significance and innovation of the research is discussed and a literature survey of related work is conducted.
- **Chapter 2:** In this chapter, the theory of tensor scale is described and the analytic definition is presented which is the basis of the research project. Also, the theory and algorithm to efficiently compute tensor scale are described, and the experimental plans, methods, and results evaluating the accuracy and efficiency of the computational framework are presented. Specifically, this chapter describes the research methods, results, and observations related to Aims 1 and 2.
- **Chapter 3:** In this chapter, the description of the theory and algorithms related to tensor scale based inter-slice interpolation algorithm is provided, as well as the experimental plans, methods, and results evaluating the accuracy of the new interpolation method. Specifically, this chapter describes the research methods, results, and observations related to Aim 3.
- **Chapter 4:** In this chapter, I present an anisotropic diffusion filtering algorithm based on tensor scale, and describe the experimental plans and results evaluating

the performance of tensor scale guided filtering method in comparison with conventional algorithms. Specifically, this chapter describes the research methods, results, and observations related to Aim 4.

- **Chapter 5:** In this chapter, the algorithm incorporating tensor scale for *n*-linear interpolation is described. Experimental plans and results evaluating the accuracy of the algorithm are presented. Specifically, this chapter describes the research methods, results, and observations related to Aims 5.
- **Chapter 6:** In this chapter, the theory and algorithms of a new fully automatic anisotropic constrained region growing method locally controlled by tensor scale for vessel segmentation are presented with experiments and results evaluating the accuracy of the new vasculature segmentation method. Specially, this chapter describes the research methods, results, and observations related to Aims 6.
- **Chapter 7:** In this chapter, a general conclusion is drawn and potential future directions are discussed with preliminary results.

CHAPTER 2

ANALYTIC DEFINITION TO TENSOR SCALE AND EFFICIENT COMPUTATIONAL ALGORITHM

2.1 Introduction

In this chapter, a new analytic approach to define a local morphometric scale using tensor model and an effective computational solution in 2- and 3-D is introduced. Then I will describe experimental plans to examine the accuracy performance of the computation method. Specifically, we examine the robustness of 2-D tensor scale computation under noise and blur quantitatively in comparison with that of our previous method using brain phantoms. Then we evaluate the accuracy of our tensor scale computation method based on differential geometry quantitatively on 3-D phantoms and compare its performance with that of direct implementation of spatial sampling method.

In the following, I will first present basic definitions and notions of tensor scale followed by detailed descriptions for computation algorithms used in the research project. For experimental methods and results, I describe the plan and methods related to experiments evaluating the accuracy and efficiency of the method. Finally, the experimental results are given and conclusion is drawn.

2.2 Analytic Definition of Tensor Scale

Let $\mathbb{R}$ denote the set of real numbers, for analytic definition, we consider an image $\mathbb{I}$ in continuous space $\mathbb{R}^n$. Image $\mathbb{I}$ is considered as the union of multiple objects which are defined as partitions by M $(n-1)$-D pseudo-Riemannian manifolds, say, $m_1, m_2, \cdots, m_M$; we refer to these manifolds as partitioning manifold. Now, let us first consider a point $p \in \mathbb{R}^n$ and the subspace W_i formed by a set of i orthogonal vectors $\boldsymbol{\tau}_1(p), \boldsymbol{\tau}_2(p), \ldots, \boldsymbol{\tau}_i(p)$ with p being the origin. An image with partitioning manifolds $W_i^{\perp} \cap m_1, W_i^{\perp} \cap m_2, \ldots, W_i^{\perp} \cap m_M$ is formed over the orthogonal complement $W_i^{\perp}$ of W_i. Let us refer to this image as orthogonal complement image of the vectors $\boldsymbol{\tau}_1(p), \boldsymbol{\tau}_2(p), \ldots, \boldsymbol{\tau}_i(p)$ at p. Finally, tensor scale

at a point $p \in \mathbb{R}^n$ is an ordered sequence of orthogonal vectors $\langle \boldsymbol{\tau}_1(p), \boldsymbol{\tau}_2(p), \ldots, \boldsymbol{\tau}_n(p) \rangle$ inductively defined as follows:

1. $\boldsymbol{\tau}_1(p)$ is the vector from p to the closest point on the nearest partitioning manifold.
2. Given the first i orthogonal vectors, $\boldsymbol{\tau}_1(p), \boldsymbol{\tau}_2(p), \ldots, \boldsymbol{\tau}_i(p)$, the $(i+1)$th vector $\boldsymbol{\tau}_{i+1}(p)$ points from p to the closest point on the nearest partitioning manifold in the orthogonal complement image of $\boldsymbol{\tau}_1(p), \boldsymbol{\tau}_2(p), \ldots, \boldsymbol{\tau}_i(p)$ at p.

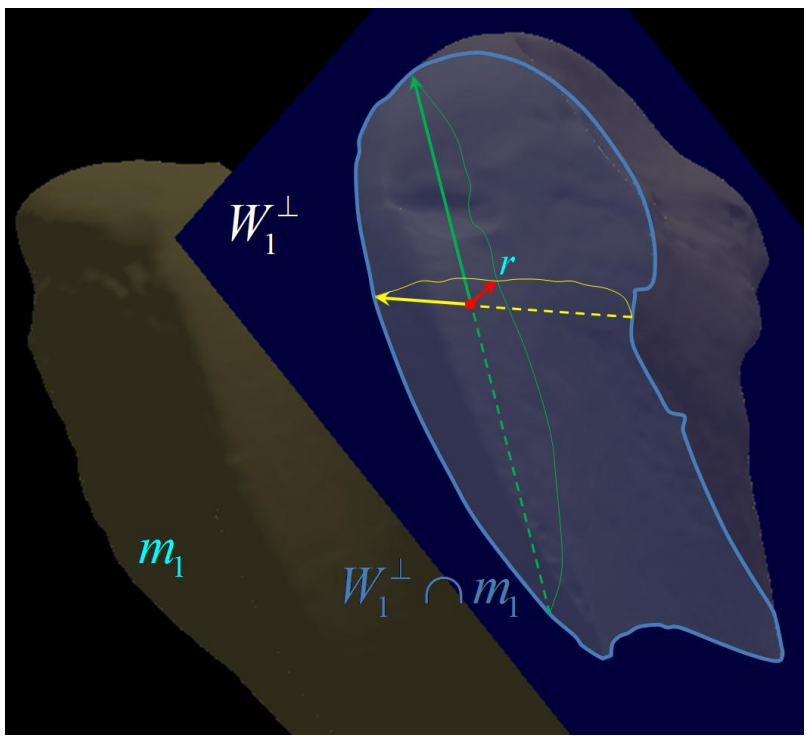

Figure 2 An illustration of tensor scale using a rabbit femur bone surface (dark off-white) forming a 2-D manifold m_1. The candidate spel p is shown as a red dot; the point on m_1 closest to p gives the primary t-vector $\boldsymbol{\tau}_1(p)$ (red). The orthogonal complement plane $W_1^{\perp}$ and the 1-D manifold $W_1^{\perp} \cap m_1$ are shown in blue and cyan, respectively. Secondary t-vector $\boldsymbol{\tau}_2(p)$ is defined by the point on $W_1^{\perp} \cap m_1$ closest to p; finally, $\boldsymbol{\tau}_3(p)$ is given by the closest point on $W_1^{\perp} \cap m_1$ along the line orthogonal to $\boldsymbol{\tau}_2(p)$. It may be noted that projections of the two lines (dotted yellow and green) on m_1 along $\boldsymbol{\tau}_1(p)$ provide principal directions of m_1 at r, the meeting location with $\boldsymbol{\tau}_1(p)$; this idea is used in our computational solution in 3-D.

In 2- and 3-D, we refer to $\boldsymbol{\tau}_1(p)$, $\boldsymbol{\tau}_2(p)$ and $\boldsymbol{\tau}_3(p)$ (only, for 3-D) as primary, secondary and tertiary (only for 3-D) as *primary*, *secondary* and *tertiary t-vectors* of p; in general, "t-vector" will refer to any of the three vectors. The notion of tensor scale defined as above is schematically illustrated in Figure 2 with a 3-D rabbit femur bone surface m_1. As illustrated in the Figure, tensor scale at a point p (red dot) in a 3-D image is an ordered sequence $\langle \boldsymbol{\tau}_1(p), \boldsymbol{\tau}_2(p), \boldsymbol{\tau}_3(p) \rangle$ of three orthogonal t-vectors. The primary t-vector $\boldsymbol{\tau}_1(p)$ (red) defines the direction and distance to the closest point on the femur surface. The orthogonal complement plane $W_1^{\perp}$ and the 1-D partitioning manifold $W_1^{\perp} \cap m_1$ on $W_1^{\perp}$ are shown in the figure; note that the 1-D partitioning manifold (cyan) is essentially the intersection between the plane $W_1^{\perp}$ (blue) and the partitioning surface m_1 (the femur bone surface) in the 3-D image. The secondary vector $\boldsymbol{\tau}_2(p)$ (yellow) is defined by the point on $W_1^{\perp} \cap m_1$ that is closest to p. Once $\boldsymbol{\tau}_1(p)$ and $\boldsymbol{\tau}_2(p)$ are found, the line (dotted green) on which the tertiary vector $\boldsymbol{\tau}_3(p)$ (green) lie is confirmed; the final direction and the length of $\boldsymbol{\tau}_3(p)$ is defined by finding the closest point on the partitioning surface along the line. It may be noted that projections of the two dotted lines (yellow and green) on m_1 along the primary vector $\boldsymbol{\tau}_1(p)$ provides two principal directions on m_1 where it meets $\boldsymbol{\tau}_1(p)$; this observation is used in our computational solution for tensor scale in 3-D.

Here, we will present a matrix representation $T(p)$ of tensor scale at p derived from the ordered sequence of orthogonal t-vectors $\langle \boldsymbol{\tau}_1(p), \boldsymbol{\tau}_2(p), \dots, \boldsymbol{\tau}_n(p) \rangle$ facilitating use of conventional tensor algebra. Let $\mathbf{i}_j(p)$ denote the unit vector along $\boldsymbol{\tau}_j(p)$ and let $\lambda_j(p)$ be the magnitude of $\boldsymbol{\tau}_j(p)$. The matrix tensor scale is defined as follows:

$$T(p) = [\mathbf{i}_1(p), \mathbf{i}_2(p), \dots, \mathbf{i}_n(p)] \begin{bmatrix} \lambda_1^2(p) & \cdots & 0 \\ \vdots & \ddots & \vdots \\ 0 & \cdots & \lambda_n^2(p) \end{bmatrix} [\mathbf{i}_1(p), \mathbf{i}_2(p), \dots, \mathbf{i}_n(p)]^{\mathrm{T}}.$$

It may be shown that $\lambda_1(p) \leq \lambda_2(p) \leq \cdots \leq \lambda_n(p)$ and therefore, although, the ordering of vectors $\langle \boldsymbol{\tau}_1(p), \boldsymbol{\tau}_2(p), \dots, \boldsymbol{\tau}_n(p) \rangle$ is ignored in matrix representation, it may be recovered from the matrix representation by analyzing eigenvalues.

2.3 Computational Solution

A direct approach to formulate a tensor scale computation algorithm from its definition faces two major hurdles – (1) object partitions are unknown in real images and (2) high computational complexity in three- or higher-dimensions. Here, we outline our algorithmic solution in 3-D images involving edge detection, distance transform, and differential geometric approaches which may be extended to higher dimensions. In an image, often, we don't know the partitioning manifolds used to define tensor scale. However, we may realistically assume that detected edge points in an image lie on these hypothetical manifolds. Also, because of the fact that these edge points are dense samples on these manifolds, the distance transform from these edge points is a close approximation to distance transform from the hypothetical partitioning manifolds. With this understanding, tensor scale may be computed by using gradient analysis and computational geometric approaches to the distance transform map from edge points in an image.

The basic idea behind our algorithm is to first locate edge points in an image and use those as sample points on partitioning manifolds. As mentioned earlier the distance transform from edge locations in an image is an approximation of that from unknown partitioning manifolds. Thus, the gradient of the distance transform map at any given point presents the direction to the nearest partitioning manifold, i.e., the direction of the primary t-vector. The magnitude of the primary t-vector is defined by the distance transform value at the candidate point. Once the primary t-vector is determined, in 2-D, the secondary t-vector may be computed by locating the closest manifold along the line perpendicular to primary t-vector. However, this computation is not that trivial in 3-D where the first step is to determine the principal direction on the local partitioning manifold (Figure 2). This job is accomplished using a new based on computational geometric analysis of distance transform from discrete sample points of a hypothetical

manifold. In the following we describe different steps in tensor scale computation starting with basic definitions and notations.

In this work, all computational and algorithmic developments are confined to 2- and 3-D images, although, the methods may generalize to higher dimensions. Let $\mathbb{Z}$ denote the set of integers. Thus, $\mathbb{R}^2$ and $\mathbb{R}^3$ represent a *2*-D *plane* and a *3*-D *space* while $\mathbb{Z}^2$ or $\mathbb{Z}^3$ denote a *digital space* in 2- or 3-D, respectively. In our discussion, $\mathbb{Z}^n$ will be used where $\mathbb{Z}^2$ and $\mathbb{Z}^3$ are referred commonly. An n-D *digital image* is defined with an image intensity function $f: \mathbb{Z}^n \to \mathbb{R}$. Each element of an n-D digital space is referred to as a *spel* (an abbreviation of "spatial element") whose position is denoted by Cartesian coordinates (x_1, x_2) or (x_1, x_2, x_3) where $x_1, x_2, x_3 \in \mathbb{Z}$. For any two spels $p, q \in \mathbb{Z}^n$, $|p - q|$ denotes the Euclidean distance between the two spels. For any vector $\mathbf{v} \in \mathbb{R}^n$, $|\mathbf{v}|$ gives its magnitude.

2.3.1 Edge Detection and Distance Transform Computation

The purpose of edge detection is to compute sample points on unknown partitioning manifolds in a digital image representation. Here, we have adopted an edge detection approach combining both Laplacian of Gaussian (LoG) and Derivative of Gaussian (DoG) operators. Specifically, an edge is located at the zero crossing of LoG if absolute value of its DoG is above a predefined threshold. It may be noted that edge locations in an image form a set of points in $\mathbb{R}^n$, therefore, a zero crossing of LoG often does not coincide with a spel having integral coordinates. This problem is solved by analyzing topological consistency of alterations of signs in LoG values at spels over 2×2 (in 2-D) or $2 \times 2 \times 2$ neighborhood; an illustration of different geometric classes of possible alteration patterns over a $2 \times 2 \times 2$ neighborhood is presented in Figure 3.

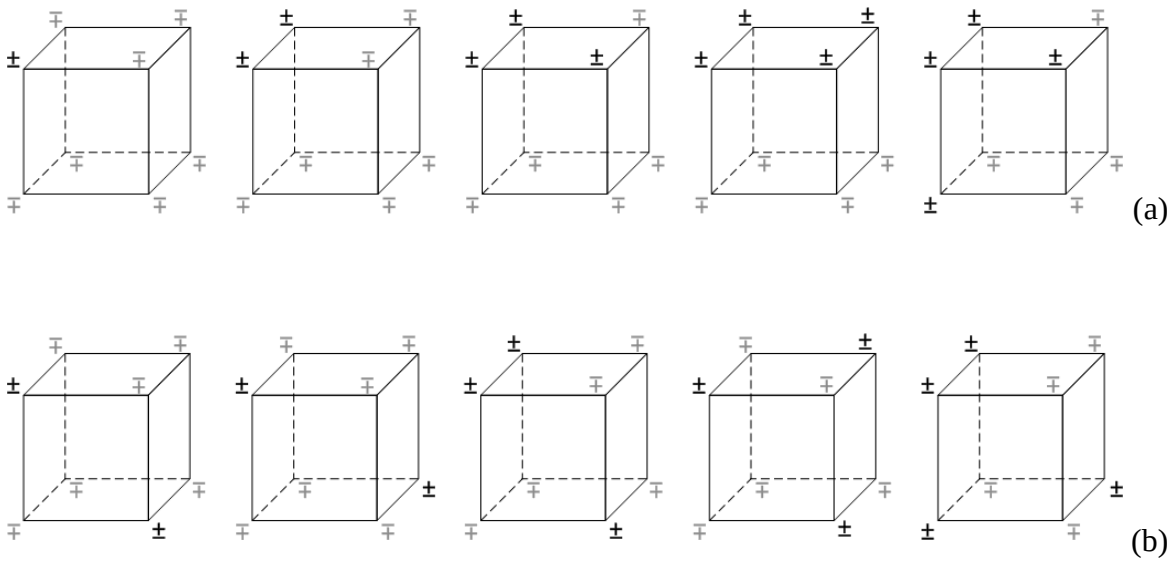

Figure 3 Illustration of different patterns of sign alteration of LoG values $2 \times 2 \times 2$ neighborhood. Spels in a $2 \times 2 \times 2$ neighborhood are marked with $\pm$ or $\mp$ (light gray) indicating that if the sign of LoG for spels marked with $\pm$ is positive then that for spels marked with $\mp$ is negative or vice versa. (a) All possible geometric classes of sign alterations with a valid zero crossing of LoG. (b) A few examples of sign alterations without a zero crossing of LoG.

Alteration patterns in a geometric class are identical under mirror reflection and/or rotations by integral multiple of 90 degrees. Topological consistent cases of LoG sign alterations are shown in Figure 3(a) where the points with identical LoG sign are 6-connected; a few examples of topologically non-consistent alteration patterns are shown in Figure 3(b). A zero crossing of LoG is identified for topologically consistent cases, only. To determine the edge location, first, a zero crossing is located for each pair of points with alternating LoG values in the $2 \times 2 \times 2$ neighborhood. Finally, the edge is located at the mean of these zero crossings. The DoG value at the edge location is determined using *n*-linear interpolation of DoG values at grid locations in 2×2 or $2 \times 2 \times 2$ neighborhood depending upon image dimensionality. As far our knowledge goes, the idea of using topological consistency in detecting zero-crossing is original and was not used before. Finally, two thresholds thr_{high} and thr_{low} of DoG values and a

technique similar to hysteresis, presented in Canny's edge detection algorithm [115], are used to select both strong and weak edges while avoiding noisy zero-crossings. The two thresholds $\mathrm{thr}_{\mathrm{high}}$ and $\mathrm{thr}_{\mathrm{low}}$.were determined using the hysteresis threshold detection algorithm for the Canny edge detector [115, 116]. Saha *et al.* [117] described an application-dependent training approach to determine different gradient parameters.

Distance transform is defined as a function or an image $DT: \mathbb{Z}^n \rightarrow \mathbb{R}$, where, $DT(p)|p \in \mathbb{Z}^n$ gives its Euclidean distance at p from the closest partitioning manifold represented by edge points. Here, the basic idea is to use zero crossing locations in $\mathbb{R}^n$ and then compute Euclidean distance transform from these locations. Let E denote the set of all zero crossings in an image; an edge location $e \in E$ falls inside a 2×2 (in 2-D) or $2 \times 2 \times 2$ (in 3-D) neighborhood which will be referred to as the *binding box* of e. For each edge location $e \in E$, a distance transform value is initialized at four (in 2-D) or eight (in 3-D) spels at the vertices of the binding box of e by directly computing their distances from e. After this initialization, the Euclidean distance transform values are propagated inside using a wave propagation algorithm similar to the approach adopted in [118, 119].

2.3.2 Tensor Scale Computation

Tensor scale algorithm determines the primary t-vector from the gradient of distance transform image and subsequent tensor scale vectors are computed using differential geometric approaches. At a spel $p \in \mathbb{Z}^n$, the direction the primary t-vector $\boldsymbol{\tau}_1(p)$ is determined as the gradient direction of DT at p and the magnitude of the vector is defined as the DT value at p, i.e.,

$$|\boldsymbol{\tau}_1(p)| = DT(p),$$

and the unit vector $\mathrm{i}_1(\mathrm{p})$ along $\tau_1(\mathrm{p})$ is

$$\mathbf{i}_1(p) = \frac{\boldsymbol{\nabla} DT(p)}{|\boldsymbol{\nabla} DT(p)|}$$

Here, we have used the Sobel gradient operator.

Once, the primary t-vector $\boldsymbol{\tau}_1(p)$ is determined, computation of the secondary t-vector $\boldsymbol{\tau}_2(p)$ in 2-D is straightforward because the vector lies on the straight line L_p perpendicular to $\boldsymbol{\tau}_1(p)$. Thus, $\boldsymbol{\tau}_2(p)$ may be computed by locating the closest partitioning manifold along the straight line L_p. However, a difficulty here is that the edge locations representing partitioning manifold are discrete points in $\mathbb{R}^n$ and therefore, a simple sampling approach along a straight line for locating a manifold may raise the danger of missing the target manifold.

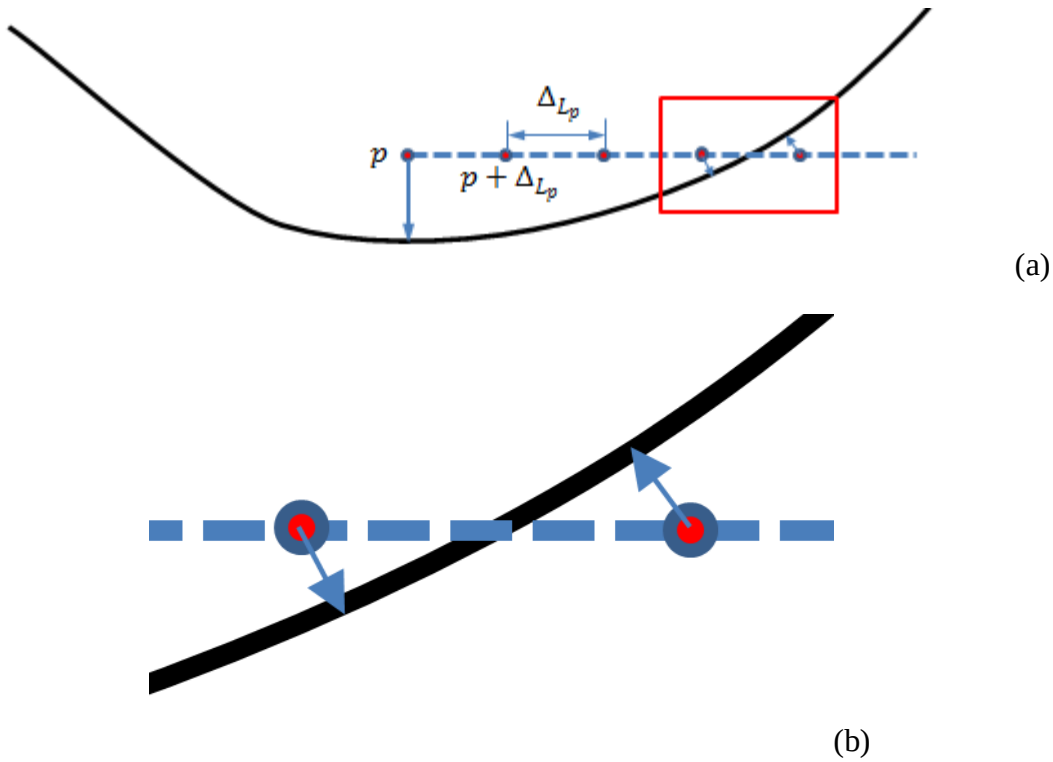

Figure 4 Illustration of the scheme for locating target manifold along specified direction. (a) Distance and primary vector information is investigated at sample points $p + i\Delta_{L_p}$ on a line L_p. (b) Sample point is considered as sufficiently close to the target manifold if distance transform value is sufficiently small and the angular difference for primary vector with its successor is greater than a preset threshold.

This problem is overcome by modifying the search process as illustrated in Figure 4 – let $p + i\Delta_{L_p} | i = 1,2, \ldots$ be the sample points on a line L_p; the jth is sufficiently close to the target manifold along L_p if it satisfies the following two conditions:

1. $DT\left(p + j\Delta_{L_p}\right) \leq \delta_{\text{DT}}$,
2. The angular difference between the two primary t-vectors $\boldsymbol{\tau}_1\left(p + j\Delta_{L_p}\right)$ and $\boldsymbol{\tau}_1\left(p + (j+1)\Delta_{L_p}\right)$ at the two successive sample points $p + j\Delta_{L_p}$ and $p + (j+1)\Delta_{L_p}$ is close to 180° (in this paper, we have use "$\geq 135^{\text{o}}$" to account for errors. It may be noted that, if the angular difference is less than 90°, the two points are on the same side of the partitioning manifold. Thus, the threshold of 135° was picked at the middle of the ideal situation of 180° and 90° when the two points fall on the same side of the partitioning manifold.

The value of δ_{DT} is determined by the density of edges locations and it should also define the sample interval size Δ_{L_p}; in this paper, we have used $\delta_{\text{DT}} = 1$. Finally, the target manifold is located on the line L_p at a distance of $j\Delta_{L_p} + DT\left(p + j\Delta_{L_p}\right)$ from p.

Computation of the secondary t-vector $\boldsymbol{\tau}_2(p)$ is more challenging in 3-D as compared to 2-D. The primary reason behind the difficulty is that, the determination of $\boldsymbol{\tau}_1(p)$ narrows down $\boldsymbol{\tau}_2(p)$ onto a plane P perpendicular to $\boldsymbol{\tau}_1(p)$. However, $\boldsymbol{\tau}_2(p)$ may lie along any direction on the plane. Here, we choose the vector $\boldsymbol{\tau}_2(p)$ along the maximum curvature direction at the closest point r on a partitioning manifold. A challenge is how to compute the maximum curvature direction at r because an analytic expression of the partitioning surface is unknown; instead, discrete sample points (edge locations) on the surface are available. The basic idea behind our algorithm of detecting the maximum curvature direction is to first, determine the primary t-vector $\boldsymbol{\tau}_1$ at every spel in the neighborhood of p. The primary t-vector $\boldsymbol{\tau}_1$ at a neighboring spel of p intersects the partitioning surface at the vicinity of r (see Figure 5). More importantly, the angular inclination of $\boldsymbol{\tau}_1$ with the plane P, perpendicular to $\boldsymbol{\tau}_1(p)$, changes most rapidly along the direction of maximum principal curvature and it changes slowly along the

minimum principal curvature direction. In other words, the projection of the unit vector along $\boldsymbol{\tau}_1$ on P takes larger values along the maximum curvature direction and it takes smaller values along the minimum curvature.

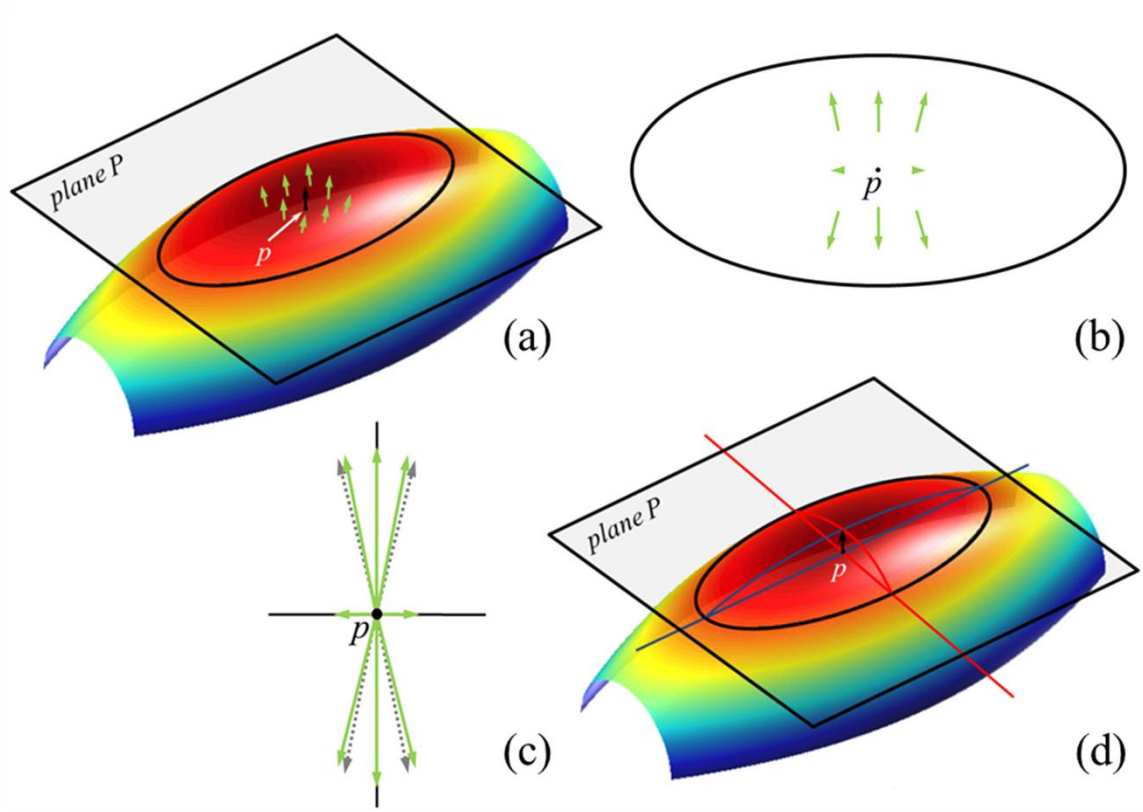

Figure 5 Illustration of the computation of secondary t-vector $\boldsymbol{\tau}_2(p)$ in 3-D. (a) A partitioning surface with primary vector $\boldsymbol{\tau}_1(p)$ (black) and $\boldsymbol{\tau}_1(q)$ (green) for several qs (green dots) in the neighborhood of p (black dot). (b) Projection vectors $\boldsymbol{\tau}_1'(q)$ of normalized vectors $\boldsymbol{\tau}_1(q)/|\boldsymbol{\tau}_1(q)|$ on P along with the curve at the intersection of P and the partitioning surface. (c) Computation of principal directions using $\boldsymbol{\tau}_1'(q)$ (solid) and $-\boldsymbol{\tau}_1'(q)$ (dotted). (d) Projection of principal directions onto partitioning surfaces.

Although our method is primarily based on this theory, to reduce the effect of noise and discretization, we determine the principal curvature direction using principal component analysis (*PCA*) of these projection vectors on P as follows. Let $q_1, q_2, \ldots, q_m$

be m points in the neighborhood of p and let $\mathbf{i}_1'(q)$ (solid vectors on Figure 5(b, c)) be the projection of the unit vector $\boldsymbol{\tau}_1(q)/|\boldsymbol{\tau}_1(q)|$ on P. To enforce axial symmetry of projection vectors, each projection vector $\mathbf{i}_1'(q)$ (solid line, Figure 5(c)) is accompanied with an opposite vector $-\boldsymbol{\tau}_1'(q)$ (dotted line). PCA of the all points represented by these vectors is applied to compute the two principal directions; the eigenvector corresponding to larger eigenvalue gives the direction for maximum principal curvature while the other eigenvector provides the direction of the minimum curvature (see Figure 5(d)).

The secondary t-vector $\boldsymbol{\tau}_2(p)$ is chosen along the maximum curvature direction; the exact value of the t-vector is determined using the same algorithm adopted for detecting $\boldsymbol{\tau}_2(p)$ in 2-D. Finally, once the primary and secondary t-vectors are known, the task of finding the tertiary t-vector in 3-D is equivalent to determining the secondary t-vector in 2-D.

2.3.3 Tensor Scale Smoothing

A smoothing filter is often used to reduce noise in intensity images. However, smoothing of a tensor scale image may not be as trivial as smoothing a scalar image. First, a matrix representation $T(p)$ of tensor scale at p is obtained as described at the beginning of Section 2.2. enabling various tensor operations and statistical analysis. Weickert [29] used component-wise Gaussian convolution on local structure tensors to obtain a smooth representation. To both avoid producing negative eigenvalues in a component-wise averaging that contradicts the basic definition of tensor scale and generating more reliable smoothing result, we have adopted the Log-Euclidean distance (L-E) approach [12]. Effectiveness of the L-E approach in diffusion tensor image (DTI) interpolation has been demonstrated in [12].

Let $A = Q\Lambda Q^{\mathrm{T}} | Q\text{: unitary matrix}, \Lambda\text{: diaginal matrix}$, be a symmetric positive semi-definite matrix. The logarithm and the exponential of this matrix are defined as follows:

$$\log A = Q \log \Lambda \; Q^{\mathrm{T}} = Q \begin{bmatrix} \log \lambda_1 & \cdots & 0 \\ \vdots & \ddots & \vdots \\ 0 & \cdots & \log \lambda_n \end{bmatrix} Q^{\mathrm{T}}$$

$$e^A = Q e^{\Lambda} Q^T = Q \begin{bmatrix} e^{\lambda_1} & \cdots & 0 \\ \vdots & \ddots & \vdots \\ 0 & \cdots & e^{\lambda_n} \end{bmatrix} Q^T.$$

A smoothing function using the L-E approach is defined using a discrete Gaussian kernel $G_\sigma : \mathbb{Z}^n \to \mathbb{R}$

$$G_\sigma(a) = \begin{cases} K \mathrm{e}^{-\frac{|a|^2}{2\sigma^2}}, & \text{if } a \in G_{\text{support}}, \\ 0, & \text{otherwise}, \end{cases}$$

where G_{support} is the support of the kernel and K is the scalar normalizing factor ensuring that $\sum_{a \in G_{\text{support}}} G_\sigma(a) = 1$. Finally, the L-E based tensor smoothing algorithm is defined as:

$$T_{\text{smooth}}(p) = \exp(\log(T) * G_\sigma),$$

where, '$*$' is the convolution operator.

2.3.4 Direct Implementation of the Analytic Definition

The computation solution for tensor scale using differential geometric approaches as presented in Section 2.3.2 is efficient. However, especially in 3-D, it relies on some assumptions while relating principle curvatures of the local manifold to the direction of the secondary t-vector at a candidate point (see Figure 2). Therefore, a direct implementation of the analytic definition of tensor scale is needed to test the accuracy of the efficient computational algorithm. In the direct implementation, the primary t-vector $\boldsymbol{\tau}_1(p)$ is determined from the partitioned image using a sample-line based approach [10] with a high angular density of sample lines (10K lines over the 3-D angular space). Subsequent t-vectors are computed directly following the definition of tensor scale. At a spel $p \in \mathbb{Z}^{\mathrm{n}}$, on the orthogonal plane $W_1^{\perp}(p)$ of $\boldsymbol{\tau}_1(p)$, we will generate a 2-D image $I_1^{\perp}(p)$ as the intersection of original image and plane $W_1^{\perp}(p)$. For $I_1^{\perp}(p)$, following the

same sample-line based approach for 2-D image, we further obtain the secondary and tertiary t-vectors $\boldsymbol{\tau}_2(p)$ and $\boldsymbol{\tau}_3(p)$ for original image.

2.4 Experimental Methods and Results

As outlined in the second specific aim in Chapter 1, the overall objective of our experimental plan is to examine the robustness, accuracy, and efficiency of our tensor scale computation algorithm. Performance of the tensor scale computation algorithm has been examined both qualitatively and quantitatively. We present the results from the algorithm under analytic definition on both 2- and 3-D images. Specifically, the robustness of the algorithm is quantitatively evaluated using a set of phantom images at different noise and blur levels. Accuracy of the method is evaluated using phantom generated from simulated brain MR image and evaluation is performed in comparison with direct spatial sampling implementation. Finally, the efficiency of the method is compared with algorithm under algorithmic definition in terms of computation time.

Performance of the tensor scale computation algorithm is qualitatively illustrated in Figure 6 using 2-D image slices from the BrainWeb MR phantom data and the 3-D pulmonary human CT image. The result of the 2-D tensor scale computation algorithm on a BrainWeb MR phantom image slice randomly selected from mid-brain region is illustrated in Figure 6 (a-d). Results of edge location and gray scale distance transformation are presented in Figure 6 (b). The color coding scheme by Saha [10] was adopted to display the 2-D tensor scale image at a pixel p that represents an ellipse $\boldsymbol{\Gamma}(p)$. A color value is assigned for the tensor scale $\boldsymbol{\Gamma}(p)$ such that the hue component of color indicates its orientation while the saturation and intensity components of the color denote the anisotropy and thickness, respectively. The color coding disk at maximum intensity is shown in Figure 6 (d). Results of 3-D tensor scale computation on the pulmonary CT image are presented in Figure 6 (e-j). 3-D tensor scale at a spel p essentially represent an ellipsoid $\boldsymbol{\Gamma}(p)$.

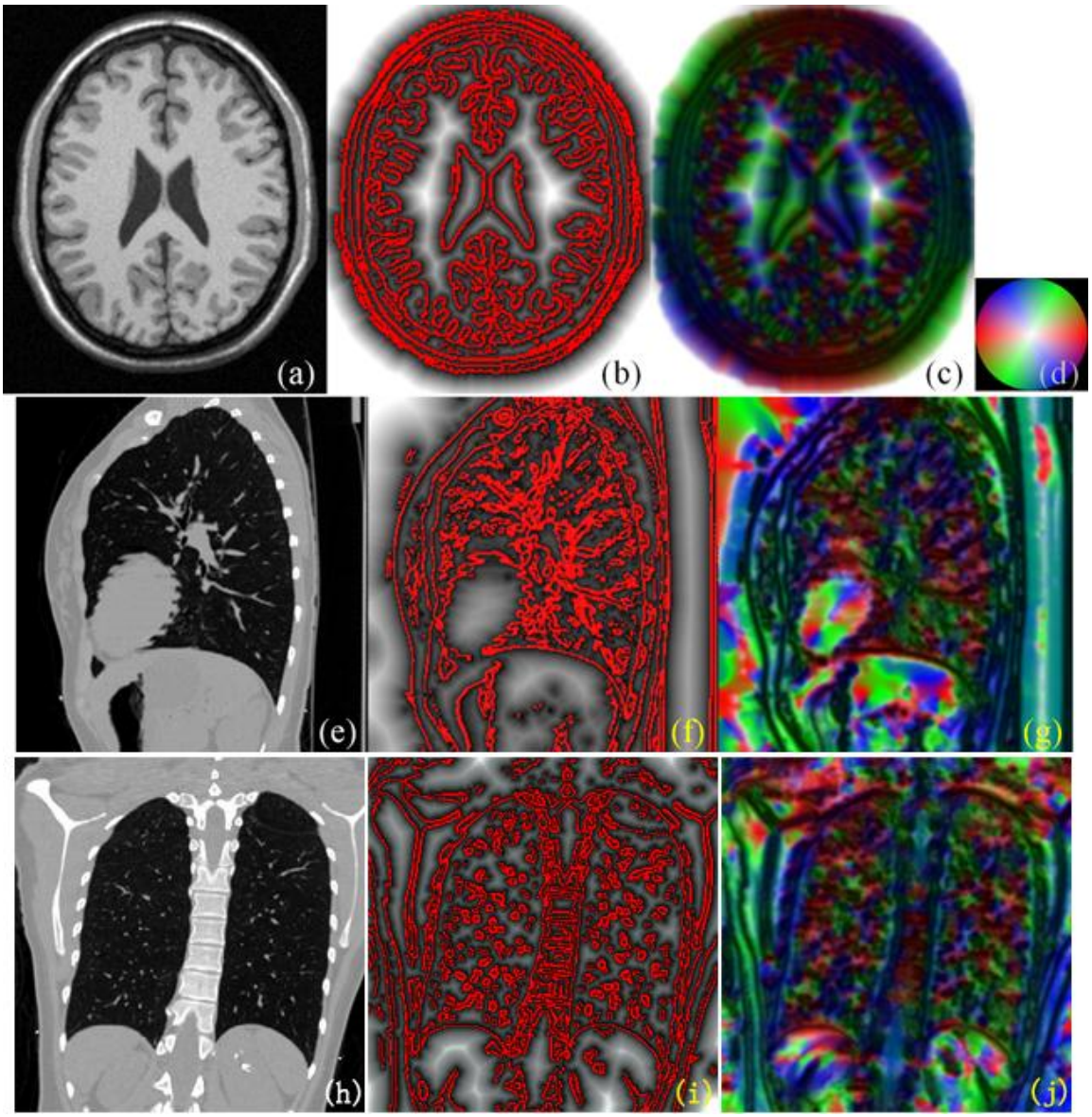

Figure 6 Results of tensor scale computation. (a) A 2-D image slice from the BrainWeb MR brain phantom data. (b) Computed edge locations (red) and gray scale distance transform. (c) A color coded illustration of 2-D tensor scale. (d) Color coding disk at full intensity. (e-g) Same as (a-c) but for 3-D tensor scale computation. Results are shown on one image slice; see text for further explanation. (h-j) Same as (e-g) but from another view.

Using three components of color-space, we may display an ellipse. Therefore, in 3-D, the intersection between $\mathbf{\Gamma}(p)$ and the display plane forming an ellipse is depicted

(Figure 6 (g,j)). In following sections, experimental methods to evaluate robustness, accuracy, and efficiency of our method is described.

2.4.1 Robustness

To evaluate the robustness of 2-D computation under different noise and blur, we follow the same experimental setup described in [10]. Based on ten phantom images generated by manual outlining of while matter and brain parenchymal regions, a set of 250 realistic 2-D phantom images at five different levels of noise and five different levels of blurring were generated from manual segmentations of white matter regions in image slices. Let $\mathcal{C}^{T_i}|_{i=1,2,\cdots,10}$ denote a true phantom image and let $\mathcal{C}_{BN}^{T_i}$ denote the phantom image obtained from $\mathcal{C}^{T_i}$ at the level of blurring B and noise N. Also, let $\mathbf{\Gamma}^{T_i}(p)$ (or, $\mathbf{\Gamma}_{BN}^{T_i}(p)$) denote the tensor scale ellipse computed at an image point p in the image $\mathcal{C}^{T_i}$ (respectively, $\mathcal{C}_{BN}^{T_i}$). In order to evaluate the robustness of a tensor scale computation method under noise and blurring, $\mathbf{\Gamma}^{T_i}(p)$ is considered as the truth because it is computed from $\mathcal{C}^{T_i}$ with no noise and blurring. A "similarity measure" of two concentric ellipses is crucial to compute the robustness of a tensor scale computation algorithm. Unlike scalar and vector quantities, similarity between two ellipses (tensor) is not trivially defined. Here, we have utilized the natural mapping that exists between the set of all ellipses and the RGB color space. Specifically, the disagreement between two ellipses is defined as the difference between their representative RGB vectors (the range of each component of RGB vector is [0, 1]). Let $\mathbf{RGB}\left(\mathbf{\Gamma}^{T_i}(p)\right)$ and $\mathbf{RGB}\left(\mathbf{\Gamma}_{BN}^{T_i}(p)\right)$ denote the RGB vectors onto which the ellipses $\mathbf{\Gamma}^{T_i}(p)$ and $\mathbf{\Gamma}_{BN}^{T_i}(p)$, respectively, are mapped. Thus, $\left(1/\sqrt{3}\right)\left|\mathbf{RGB}\left(\mathbf{\Gamma}^{T_i}(p)\right) - \mathbf{RGB}\left(\mathbf{\Gamma}_{BN}^{T_i}(p)\right)\right|$ captures the difference between true and computed tensor scales at p in terms of their distance in the color-space used here to represent tensor scales. Here, a division by $\sqrt{3}$ is applied to normalize the error measure so that its value lies in the $[0, 1]$ interval. The figure of merit $FOM_{BN}^{T_i}$ (a measure of

similarity) of a tensor scale computation method for a phantom image $\mathcal{C}_{BN}^{T_i}$ is defined as follows:

$$FOM_{BN}^{T_i} = \frac{\|\mathcal{C}^{T_i}\| - \sum_{p\in\mathcal{C}^{T_i}}\left(1/\sqrt{3}\right)\left|\mathbf{RGB}\left(\mathbf{\Gamma}^{T_i}(p)\right) - \mathbf{RGB}\left(\mathbf{\Gamma}_{BN}^{T_i}(p)\right)\right|}{\|\mathcal{C}^{T_i}\|} \times 100$$

In the above equation, $\|\mathcal{C}^{T_i}\|$ denotes the number of pixels in $\mathcal{C}^{T_i}$ and $|\cdot|$ returns the absolute value of its parameter. For a given method, at a given level of noise and blurring, the mean and standard deviation of $FOM_{BN}^{T_i}|i = 1,2,\cdots,10$ values have been computed. Also, at a given level of noise and blurring, a paired t-test has been performed on the $FOM_{BN}^{T_i}$ values obtained by the previous method with improvements [13]and the method under analytic definition discussed in this paper.

The robustness test of 2-D tenor scale computation is performed using the same brain phantoms as in [10] the result is shown in Table 1 and Table 2.

Table 1 Performance of tensor scale computation algorithm based on analytic definition at various levels of noise and blurring.

	B1	*B2*	*B3*	*B4*	*B5*
N1	98.12±0.11	97.47±0.12	96.92±0.18	95.03±0.32	93.58±0.49
N2	97.74±0.12	97.00±0.18	96.16±0.24	94.28±0.34	92.73±0.46
N3	97.35±0.15	96.55±0.19	95.61±0.23	93.77±0.41	92.31±0.52
N4	96.42±0.20	95.40±0.34	94.45±0.40	92.82±0.55	91.82±0.57
N5	95.34±0.40	94.40±0.48	93.67±0.49	92.28±0.61	91.55±0.67

Each row indicates a specific noise level that increases from top to bottom and each column indicates a specific blur level that increases from left to right. Results are reported as mean FOM ± standard deviation.

Table 1 presents the mean (first entry) and standard deviation (second entry) of FOM (figure of merit) values for different phantom images. Here, each cell presents the

statistics of ten phantom images at a specific level of noise and blurring with noise increasing from top to bottom while blurring increases from left to right.

Table 2 Comparison between the performance of the analytic and algorithmic tensor scale computation algorithms at various levels of noise and blurring.

	B1	*B2*	*B3*	*B4*	*B5*
N1	-0.53 (*)	-0.45 (*)	-0.12 (*)	-0.43 (*)	1.22 (*)
N2	-0.68 (*)	-0.56 (*)	-0.38 (*)	-0.06	0.53 (*)
N3	-0.59 (*)	-0.25 (*)	-0.06	0.95 (*)	1.02 (*)
N4	0.14	0.36 (*)	0.76 (*)	1.06 (*)	1.90 (*)
N5	0.91 (*)	1.15 (*)	1.31 (*)	1.84 (*)	1.77 (*)

Each row indicates a specific noise level that increases from top to bottom and each column indicates a specific blur level that increases from left to right. Statistically significant differences are marked by (*) denoting that the two methods has different performance at the significance level of p-value < 0.01. Positive result means the analytic computation outperforms the algorithmic method and vice versa. The two methods were statistically equivalent in the three remaining cases.

Table 2 presents the results of comparison between the analytic method and the improved algorithmic method reported in [13] for ten images at different levels of noise and blurring. It may be noted that the analytic method outperforms the algorithmic method at higher noise and blur level while the algorithmic method performs better for low level. Also, the p-values of paired t-tests for 3 cases with median noise and blur level indicate that the differences between the analytic and algorithmic methods are not statistically significant.

Such result can be explained by the fact that the algorithmic method basically performs a smoothing over the process of feature extraction by ellipse fitting while the analytic method directly finds the nearest partitioning manifolds. Therefore, there is inherently more color variation in the result produced by analytic method (as shown in

Figure 7) and therefore when noise and blur levels are low, both methods produce fairly precise result with regard to the ground truth while there is higher chance that the small difference will get shown by statistics for analytic method. However, from the result, it is clear that the analytic method is more robust under higher noise and blur levels.

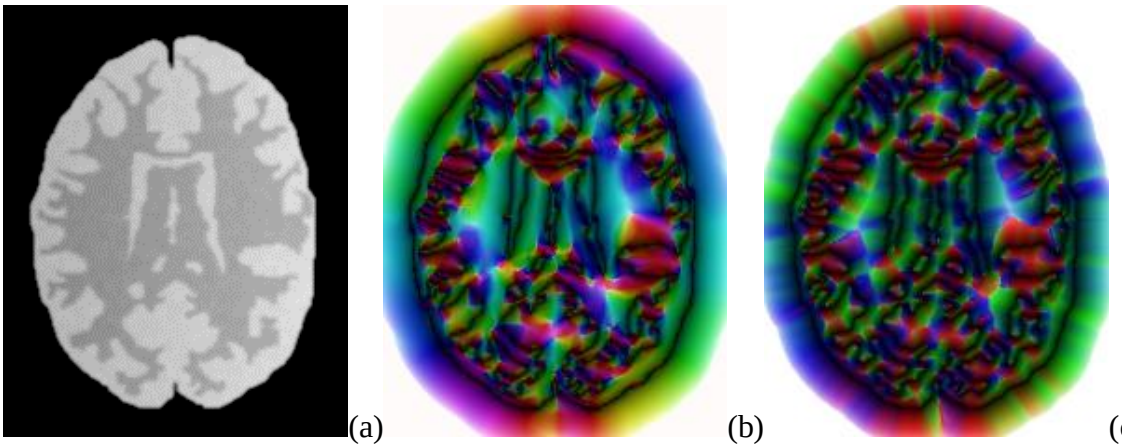

Figure 7 Results of 2-D phantom image computation. (a) An original phantom image (2) Tensor scale result produced by algorithmic method. (c) Tensor scale result produced by analytic method.

2.4.2 Accuracy

The purpose of our 3-D accuracy evaluation study is to examine the difference in tensor scale obtained using the efficient differential geometrical approach of tensor scale computation as compared with the true value directly computed from the definition using spatial sampling method. In order to perform this test, we generated phantom images at five different levels of noise (noise: 8% to 20%) and blurs (σ_{blur}: 0.5 to 2.5) from the BrainWeb simulated brain MR image and a 3-D pulmonary human computed tomography (CT) image.

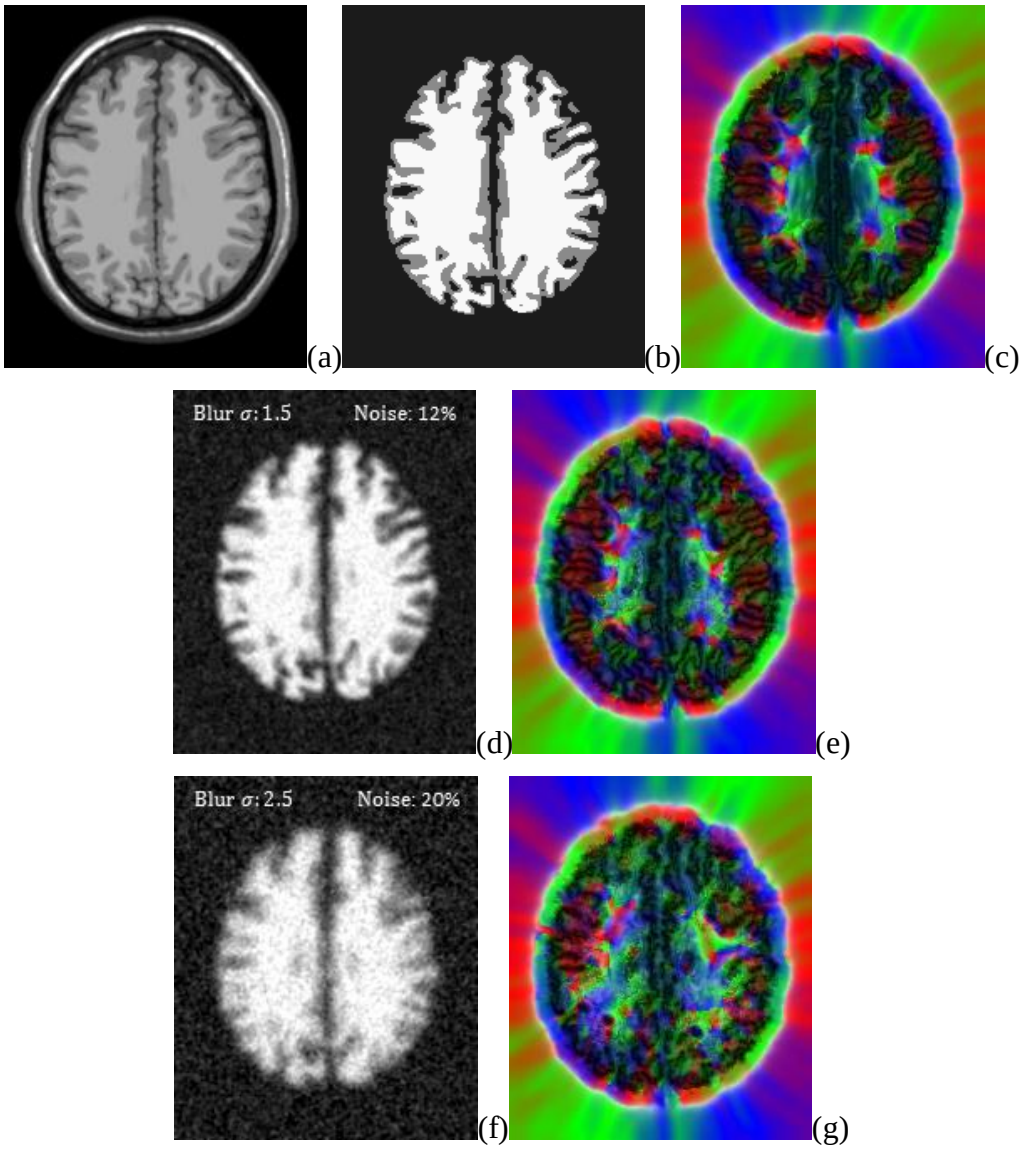

Figure 8 Tensor scale computation result comparison between differential geometric method and spatial sampling method. (a) An original slice from BrainWeb image (2) Image after threshold showing white and grey matter that defines absolute boundary for spatial sampling methods to be considered as ground truth. (c) 3-D tensor scale computation result from spatial sampling method for (b). (d) phantom with blur and noise (e) 3-D tensor scale computation result from differential geometric method for (d). (f, g) same as (d, e) but for another level of blur and noise.

The BrainWeb MR phantom data was downloaded with the following parameters – matrix size: 181×217 pixels, number of slices: 181, isotropic voxel size: 1 mm, noise:

3% and intensity non-uniformity: 20%. The pulmonary CT images was acquired using the following protocol – 120kV, 100 effective mAs, pitch factor: 1.0, nominal collimation: 64x0.6mm, image matrix: 512x512, number of slices: 518, in-plane resolution: $(0.55\text{mm})^2$ and slice thickness: 0.5mm.

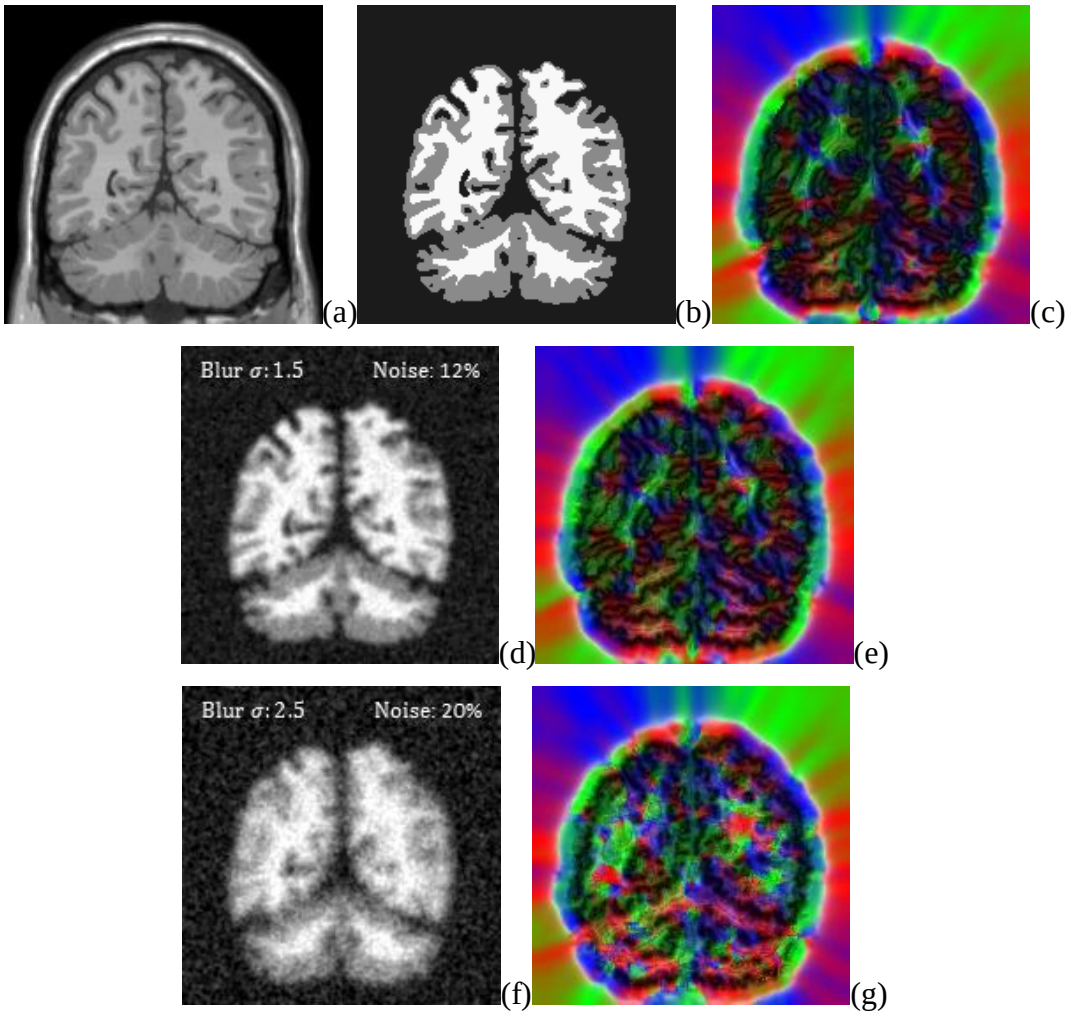

Figure 9 Same as Figure 8 but from another view.

Following the fact that the definition of tensor scale is based on an image representation with partitioning manifold, true tensor scale may not be computed from a

general image. To define the manifolds, we partitioned the image into three regions, namely, white matter, gray matter and background (Figure 8(b) and Figure 9(b)). True measure of tensor scale was obtained as described in Section 2.3.4. Test images for tensor scale computation using the new differential geometrical approach were derived from the partitioned image after adding white Gaussian noise and blur (Figure 8(d, f) and Figure 9(d, f)). Results of accuracy analysis of the efficient tensor scale computation algorithm as compared with the results directly obtained from the analytic definition are qualitatively illustrated in Figure 8 and Figure 9. As observed in both Figures, at moderate blur and noise, the agreement of the efficiently computed tensor scale with the analytic tensor scale computed in absence of noise and blur is visually satisfactory in the color coded illustration. The results match with each other in terms of color (orientation) and intensity (magnitude). However, at high noise and blur, the fine structures are lost.

Quantitative evaluation is designed based on the matrix representation of the true tensor scale at a point p and the tensor scale obtained from a test image by applying the differential geometric algorithm. We designed an error measurement based on Log-Euclidean distance and quantitatively evaluate the accuracy of differential geometric algorithm in tensor scale computation. Let $W_{\mathrm{T}}(p)$ be the true tensor scale matrix at a spel p computed from the partitioned image and let $W_{\mathrm{DG}}(p)$ denote to the tensor scale matrix representation obtained from a test image by applying the differential geometric algorithm. Although, tensor scale computation methods were applied on entire image, the error analysis was confined to white and gray matter regions only to avoid background; better results were obtained when the background region was included in error analysis. Let Ω denote the region over which the error analysis is performed. The error of tensor scale computation is defined as the average normalized Log-Euclidean distance between the true and the computed tensor scales over the target region Ω as follows:

$$error = \frac{2\sum_{p\in\Omega}\left\|\log\left(W_{\mathrm{T}}(p)\right) - \log\left(\mathrm{W}_{\mathrm{DG}}(p)\right)\right\|}{\sum_{p\in\Omega}\left(\left\|\log\left(W_{\mathrm{T}}(p)\right)\right\| + \left\|\log\left(\mathrm{W}_{\mathrm{DG}}(p)\right)\right\|\right)},$$

$\|\cdot\|$ is the Euclidean norm of a positive definite symmetric matrix.

Results of quantitative analysis are presented in Table 3. As observed in the table, the performance of the algorithm decreases, i.e., error increases with noise as well as blur. Based on these results, it may be reasonable to conclude that the computational geometric approach to tensor scale is efficient and produces acceptable tensor scale at moderate blur and noise.

Table 3 Performance of the 3-D tensor scale computation algorithm based on analytic definition at various levels of noise and blurring.

	B1	*B2*	*B3*	*B4*	*B5*
N1	4.07	5.52	6.13	7.20	8.90
N2	4.17	5.63	6.42	7.54	9.11
N3	4.46	5.75	6.59	7.73	9.29
N4	4.62	5.80	6.70	8.21	9.40
N5	5.17	6.10	7.13	8.79	9.78

Each row indicates a specific noise level that increases from top to bottom and each column indicates a specific blur level that increases from left to right. Results are reported as normalize Log-Euclidean difference (%) to the result generated by space sampling method for the original binary phantom.

2.4.3 Efficiency

The new algorithm takes 3 seconds to compute 2-D tensor scale for the BrainWeb phantom image slice running in a desktop with a 2.53 GHz Intel(R) Xeon(R) CPU and Linux OS; the original sample line based tensor scale computation algorithm [10] takes 83 seconds for the same image. Since a 3-D implementation of the original sample line based tensor scale computation algorithm is not available, we calculated the expected computation time as follows. The 2-D sample line based algorithm with 60 sample lines and 60 sample points per line takes approximately one minute for an image of size

256×256. Therefore, in 3-D with 900 sample lines (to maintain a comparable angular sampling rate) the total run time for a $512 \times 512 \times 518$ image should be approximately

$$\left(\frac{512}{256}\right)^2 \times 518 \times \left(\frac{900}{60}\right) \times 2 = 1036 \text{ hours } = \text{ 43 days.}$$

The multiplication by '2' is added to account for tri-linear interpolation in 3-D image instead of bilinear interpolation in 2-D. On the other hand, the new 3-D tensor scale computation algorithm takes approximately fifty minutes to compute tensor scale for the 3-D CT image.

2.5 Conclusion

In this chapter, we have presented an analytic formulation for tensor scale for *n*-D images. Also, we have provided an efficient computational solution for tensor scale in 2- and 3-D that is based on several new methods including gray scale distance transform and computation of local principal curvature directions on the closest partitioning manifold represented by discrete edge points. Experimental results in comparison with theoretical results derived under the ideal condition of object partitions with no noise and blur have demonstrated that the proposed efficient computation method yields acceptable results at moderate noise and blur with image structures being visually apparent.

CHAPTER 3

TENSOR SCALE BASED INTER-SLICE INTERPOLATION

3.1 Introduction

In this chapter, a new slice-interpolation method based on tensor scale is introduced and a closed form solution is presented to determine the interpolation lines in a gray level image using tensor scale information of adjacent slices. At each location on an image slice, the method derives normal vector from its tensor scale that yields trans-orientation of the local structure and points to the closest edge point. Normal vectors at the matching 2-D locations on two adjacent slices are used to compute the interpolation line using a closed form equation. Then experimental plans and results to examine the accuracy performance of the method are discussed. Specifically, the algorithm has been applied to BrainWeb data sets and to several other images from clinical applications and its accuracy and response to noise and other image-degrading factors have been examined and compared with those of current state-of-the-art interpolation methods. Experimental results have established the superiority of the new tensor scale based interpolation method as compared to existing interpolation algorithms. Also, a quantitative analysis based on the paired t-test of residual errors has ascertained that the improvements observed using the tensor scale based interpolation are statistically significant.

In the following, detailed algorithm for inter-slice interpolation will first be presented followed by experimental plans and methods. Finally, results are given and concluding remarks are drawn.

3.2 Tensor Scale Based Inter-Slice Interpolation

The general purpose of medical image interpolation is to increase image resolution along the slice direction using an image processing algorithm. Although classical interpolation methods use neighborhood intensity analysis techniques over adjacent slices, more advanced algorithms follow the approach of detecting “interpolation

lines" [69] using the correspondence of local structures in adjacent slices. Here, we present a new interpolation method that provides a closed form solution for identifying this correspondence using its tensor scale information in adjacent slices, which is used to compute local deformation as well as the interpolation line at the individual image point.

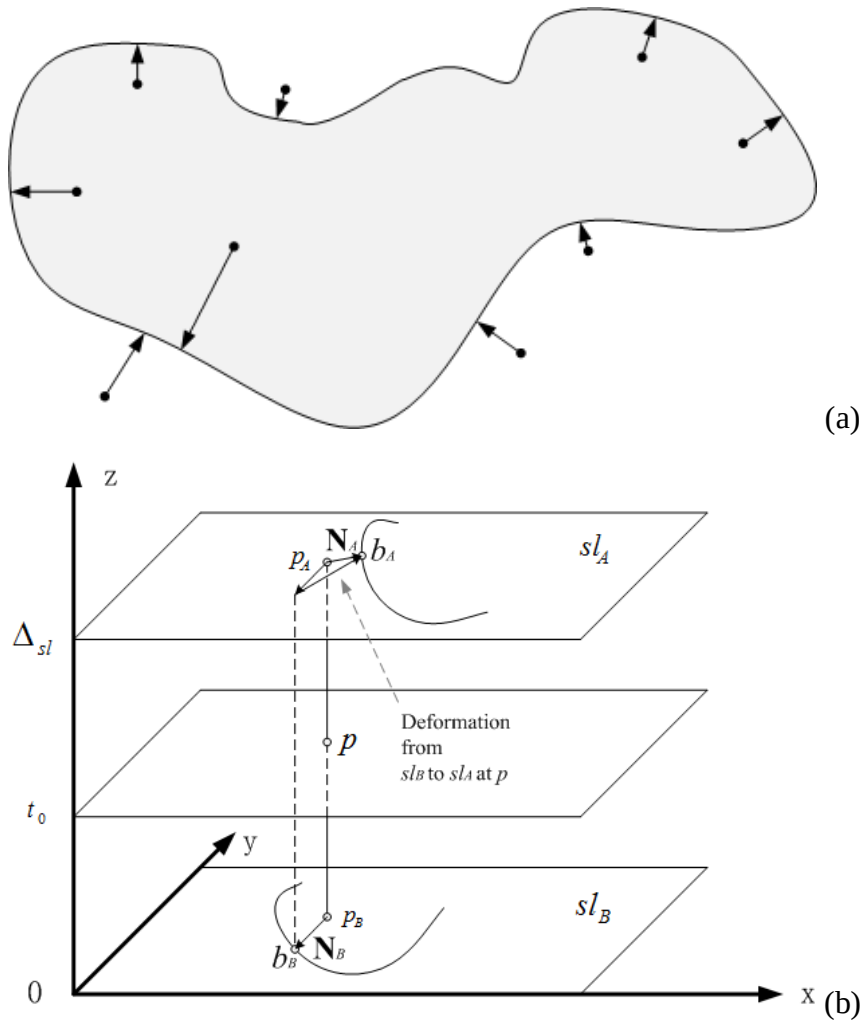

Figure 10 Schematic descriptions of the principle of tensor scale based image interpolation. (a) Examples of normal vectors at different points inside and outside of a shape. (b) A closed form solution exists for computing the deformation vector using normal vectors.

The key idea is to compute the local deformation between two adjacent slices from their tensor scale information which is accomplished in two steps – (1) computation of tensor scale-derived normal vector (Figure 10 (a)) associating each image point on a slice to its nearest edge point and (2) determine local deformation between two adjacent slices using a closed form equation involving normal vectors in two adjacent slices (Figure 10 (b)). Let p_A and p_B be the spatially matching image points on two adjacent slices, namely, sl_A and sl_B; thus p_A and p_B have the same 2-D coordinates, say p, in the two slices. Let $\mathbf{N}_A$ and $\mathbf{N}_B$ be the normal vectors at p_A and p_B, respectively. It is interesting to observe from the Figure that the deformation $\boldsymbol{\tau}(p, sl_B, sl_A)$ from sl_B to sl_A at the 2-D image point p may be determined by subtracting the vector $\mathbf{N}_B$ from $\mathbf{N}_A$, i.e., $\boldsymbol{\tau}(p, sl_B, sl_A) = \mathrm{N_A} - \mathbf{N}_B$.

In the following, we first describe the method of computing normal vectors from local tensor scales and then explain the interpolation method using normal vectors. Finally, we discuss the challenges with the method and offer their solutions.

3.2.1 Computation of Normal Vectors Using Tensor Scale

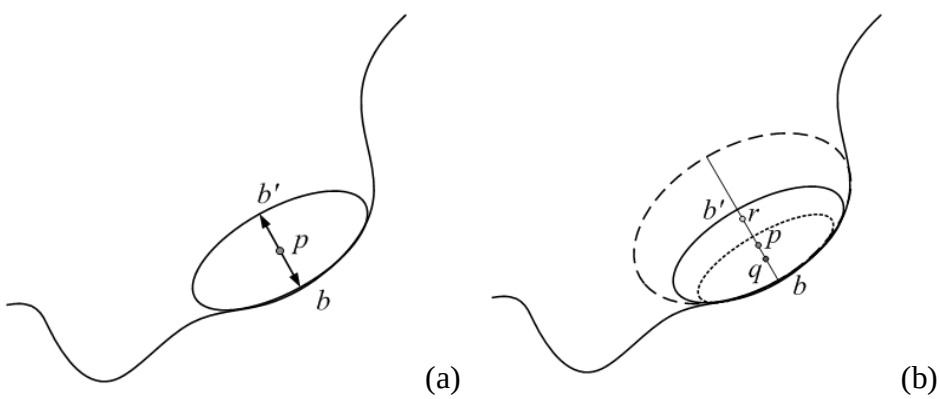

Figure 11 Computation of the normal vector from local tensor scale. (a) An ambiguity in selecting the normal vector between $\overrightarrow{pb}$ and $\overrightarrow{pb'}$ – the opposite vectors along the minor axis of tensor scale. (b) This ambiguity is solved by analyzing tensor scale-derived isotropic scales along the direction of the minor axis bb'.

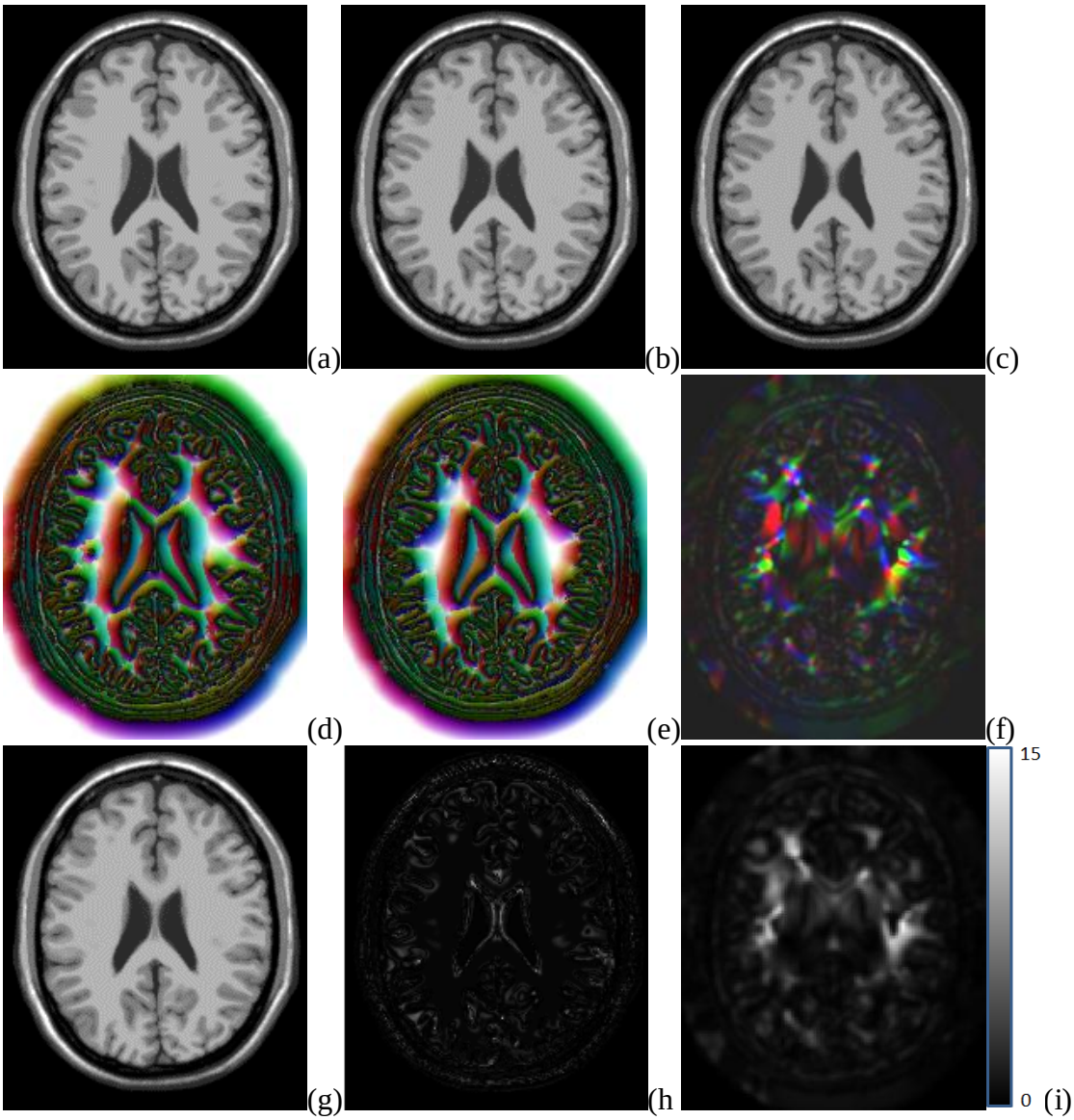

Figure 12 Intermediate results of tensor scale based image interpolation on MR brain data. (a-c) Three successive slices from the BrainWeb MR phantom data. (d,e) Normal vector fields computed from (a,c). (f) Color-coded deformation vector field computed from (d,e) on the slice plane located at the middle of the slice of (a,c). (g) Image interpolated from (a) and (c). Compare the result with (b). (h) Interpolation error computed from (b) and (g). (i) Magnitude of the deformation field.

As mentioned earlier, the purpose of normal vector is to represent the nearest edge point associated with each image point and its direction is orthogonal to the orientation of

the local structure (Figure 10(a)). Following the fact that tensor scale represents the orientation of the local structure along with its size in different directions, the association between normal vector and tensor scale is obvious. Specifically, the normal vector is related to the minor semi-axis of the tensor scale at an image point p. However, as illustrated in Figure 11(a), an ambiguity arises as the tensor scale of a point p fails to directly indicate which of the two vectors $\overrightarrow{pb}$ and $\overrightarrow{pb'}$ points to the nearest boundary. This ambiguity is solved by analyzing tensor scale-derived isotropic scale along the direction of minor axis bb'. As illustrated in Figure 11(b), isotropic scales reduce along the vector $\overrightarrow{pb}$ pointing to the local boundary; therefore, $\overrightarrow{pb}$ represents the normal vector at p. The color coded representation of normal vector map for the image of Figure 12(a, c) is presented in Figure 12(d, e).

3.2.2 Interpolation Algorithm

In the beginning of this section, we have described the basic principle of computing local deformation using tensor scale-derived normal vectors. Here, we describe the new interpolation algorithm.

Let us consider two image slices sl_A and sl_B separated by a distance of Δ_{sl} as shown in Figure 13(a) and we want to interpolate the intensity at a target point $p = (x, y, t_0)$ in between the two slices. Here, the location t_0 of p in the z-direction is defined with respect to the location of the base slice sl_B; thus, $0 < t_0 < \Delta_{sl}$. Also, we assume that x and y are integer valued. The interpolation method essentially computes the interpolation line $l(t)_{0 \le t \le \Delta_{sl}}$ passing through the target point p; the line $l(t)$ gives three dimensional coordinates of a point at the height of t from the base slice. Once the interpolation line $l(t)$ is determined, the two points c_A and c_B at the intersection of the line with respective slices are computed and the intensity at p is determined using linear interpolation of the intensities at c_A and c_B. Thus, to complete the algorithm, we need to describe the method of computing the interpolation line $l(t)$.

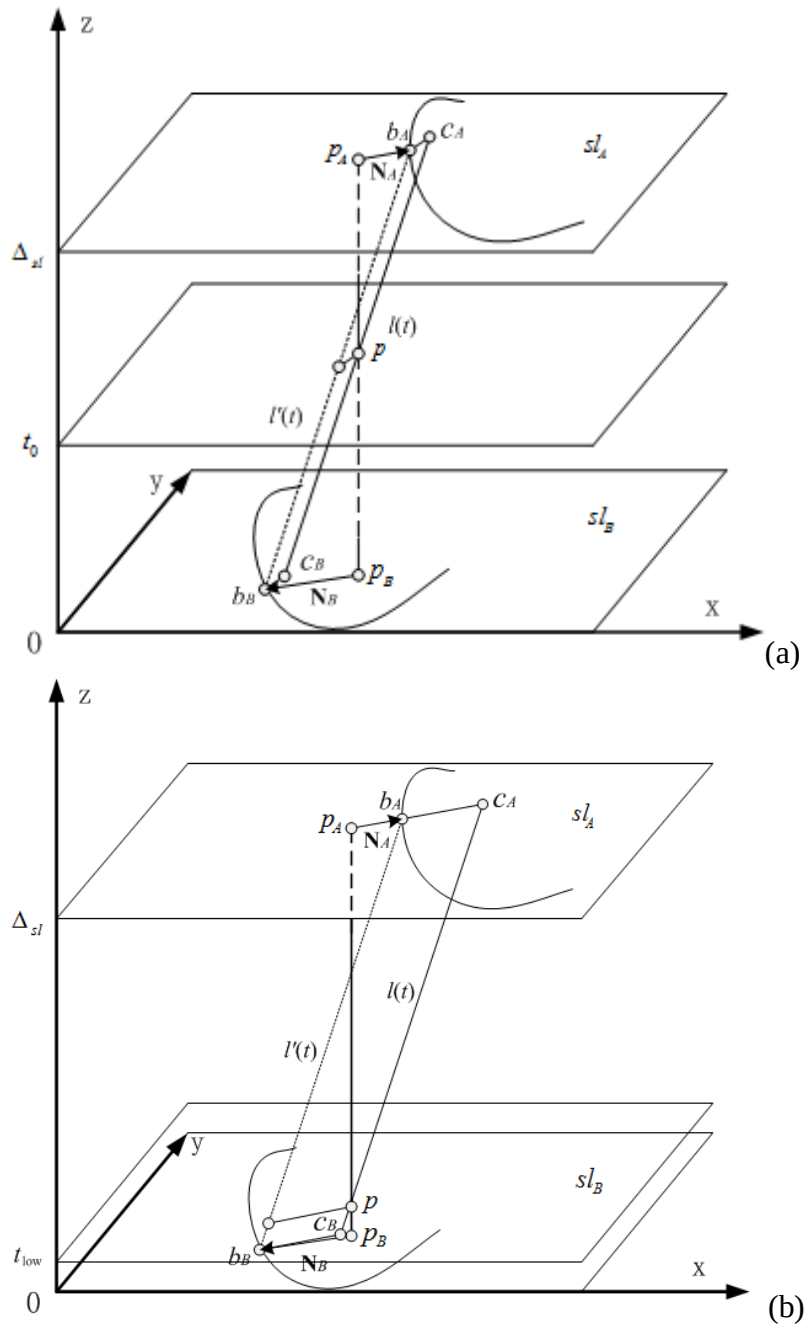

Figure 13 Illustration of computing the interpolation line $l(t)$ associated with an image point p on the interpolation plane with the information from tensor scale in images of sl_A and sl_B. (a) p locates halfway between two slices. (b) Same as (a) except that p is close to the lower slice sl_B. Although, the line $l'(t)$ is same in both (a) and (b), the final interpolation line $l(t)$ is changed due to different shifts required under the two cases. Note that the point c_B is close to p_B in (b).

First, the projections p_A and p_B of the point p on the two slices sl_A and sl_B are determined; thus, $p_A = (x, y, \Delta_{sl})$ and $p_B = (x, y, 0)$. Let $\mathbf{N}_A$ and $\mathbf{N}_B$ be the normal vectors at p_A and p_B with b_A and b_B being the nearest points on respective local boundaries as illustrated in Figure 13(a). It may be noted that the line $l'(t)$ obtained by joining the two points b_A and b_B results in a local 2-D deformation of $\mathbf{N}_A - \mathbf{N}_B$ along the slice plane when the image slice sl_A warped onto sl_B; let $\mathbf{N}_{AB} = \mathbf{N}_A - \mathbf{N}_B$. However, the line $l'(t)$ may not pass through the point p. Therefore, the interpolation line is computed by appropriately shifting the line $l'(t)$ along the slice plane so that it passes through p. The final interpolation line is computed using the following equation:

$$l(t) = \begin{bmatrix} x \\ y \\ t_0 \end{bmatrix} + (t - t_0) \times \begin{bmatrix} \mathbf{N}_{AB} \cdot \mathbf{i}_{\mathrm{x}} \\ \mathbf{N}_{AB} \cdot \mathbf{i}_{\mathrm{y}} \\ \Delta_{sl} \end{bmatrix}.$$

In the above equation, $\mathbf{i}_{\mathrm{x}}$ and $\mathbf{i}_{\mathrm{y}}$ denote the two unit vectors along the x- and y-coordinate axes, respectively. It may be interesting to note that, if the target point p is moved close to lower slice sl_B at (x, y, t_{low}) as illustrated in Figure 13(b), the initial line $l'(t)$ is not changed. However, in this situation, we need to translate the line $l'(t)$ differently so that it passes through the target point, which is now closer to slice sl_B. Thus, the final interpolation line $l(t)$ is changed as illustrated in Figure 13(b); note that in the above equation, t_0 should be replaced by t_{low}. Since, $l(t)$ intersects the line $p_A p_B$ at p, the point c_B should be close to p_B. Again, on the interpolation line $l(t)$, the target point p is much closer to c_B than to c_A. Thus, following linear interpolation, the interpolated intensity at p should be very close to that of the point c_B which is again close to the point p_B. The method works similarly when the target point p is moved close to the upper slice sl_A. Further, it may be pointed out that the shifting of initial interpolation line $l'(t)$ to $l(t)$ to determine the final interpolation line at p essentially assumes that deformation vectors over a small neighborhood are similar and ignores local variations in the deformation field. This assumption is made by most registration-based medical image

interpolation algorithms [120] where the deformation field is represented using a smooth function. It may be noted that, in our algorithm, the shift of an interpolation line is always smaller than one voxel in the slice direction.

3.2.3 Algorithm Challenges and Their Solutions

As discussed above, the basic principle of the method lies in identifying the nearest boundary point at each image point which is represented by its normal vector. A major challenge with this approach is that the normal vector is less stable near the medial axis of a local structure as it may point to any of the two opposite boundaries of the local structure leading to an ambiguity. Depending upon which of the two opposite boundary points is selected, the normal vector will significantly differ thus being a source of errors in the computation of deformation vectors used for interpolation.

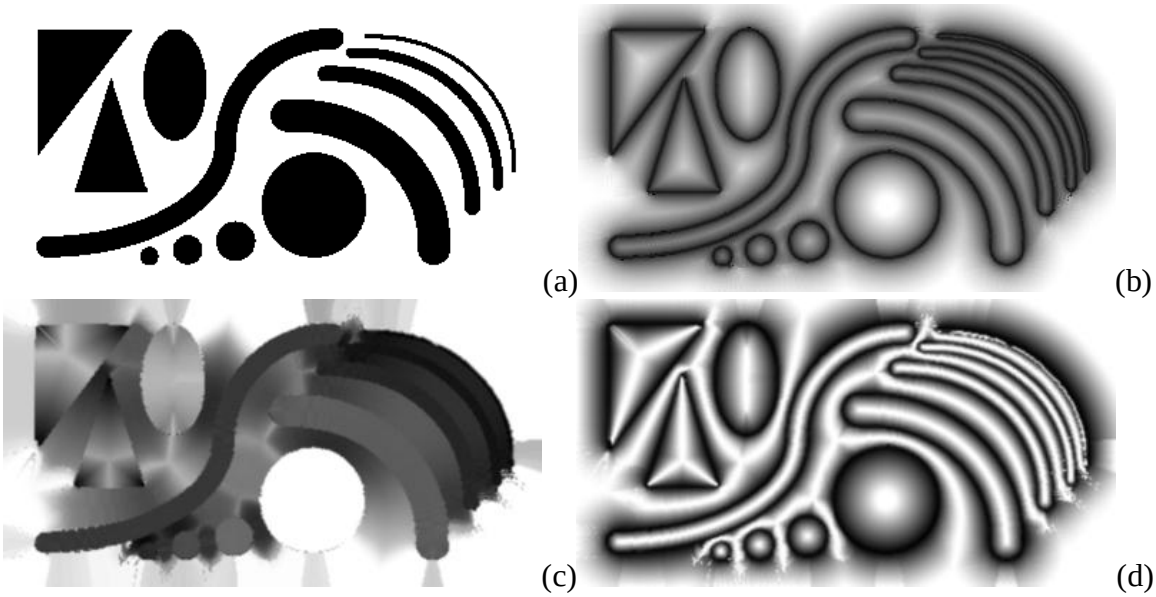

Figure 14 Illustration of tensor scale derived local structure width. (a) A binary phantom image. (b) Tensor scale-derived isotropic scale image. (c) Local structure width map. (d) Computed medialness.

This problem is overcome by detecting local medial points and taking a special care at those points while computing the deformation vector or the interpolation line. The medialness at an image location is determined by comparing its isotropic scale with another tensor scale-derived feature indicating the "local structure width". At any image point p, the *local structure width* denoted by $LSW(p)$ represents the width of the local structure around p and is defined as twice the closest maximal isotropic scale along the direction of the tensor scale minor axis $\boldsymbol{\iota}_2(p)$. Figure 14 illustrates the local structure width map for a phantom image computed using the above definition. Finally, the *medialness* of an image point p, denoted by $M(p)$, is defined as follows:

$$M(p) = \begin{cases} 1, & \text{if } 2|\boldsymbol{\iota}_2(p)| \geq LSW(p), \\ \dfrac{2|\boldsymbol{\iota}_2(p)|}{LSW(p)}, & \text{otherwise.} \end{cases}$$

Here, image points with a medialness value greater than or equal to 0.75 are considered as medial points which are treated separately to avoid the errors due to the ambiguity outlined above. Selection of a threshold close to '1' makes the algorithm vulnerable to noise. On the other hand, a lower value of the threshold leads to exclusion of image points. Here, we have used a threshold of 0.75 to ensure that 75 percent of image points may directly be used in the interpolation algorithm. To solve the problem of ambiguity at medial points, we assume that that the displacement of a structure between two adjacent slices is less than half of the local structure width.

Let us consider the situation of Figure 15 where the projection of the interpolation point p on the slice sl_A is a medial point and let a and a' be the nearest points on the two opposite edges of the structure around p_A. It may be noted from the figure that the point a on the slice sl_A corresponds to the edge point b on the matching structure around p_B on the slice sl_A. Due to the ambiguity near the medial point p_A, it is difficult to say whether $\overrightarrow{p_A a}$ or $\overrightarrow{p_A a'}$ is the true normal vector. However, with the assumption that the local deformation is less than half of the structure width, the magnitude of the deformation

using the correct correspondence of a and b must be less than that of the wrong correspondence of a' and b. Therefore, the 2-D deformation $\mathbf{N}_{AB}$ is computed using the following equation

$$\mathbf{N}_{AB} = \begin{cases} \mathbf{N}_A - \mathbf{N}_B, & \text{if } |\mathbf{N}_A - \mathbf{N}_B| \leq |-\mathbf{N}_A - \mathbf{N}_B|, \\ -\mathbf{N}_A - \mathbf{N}_B, & \text{otherwise.} \end{cases}$$

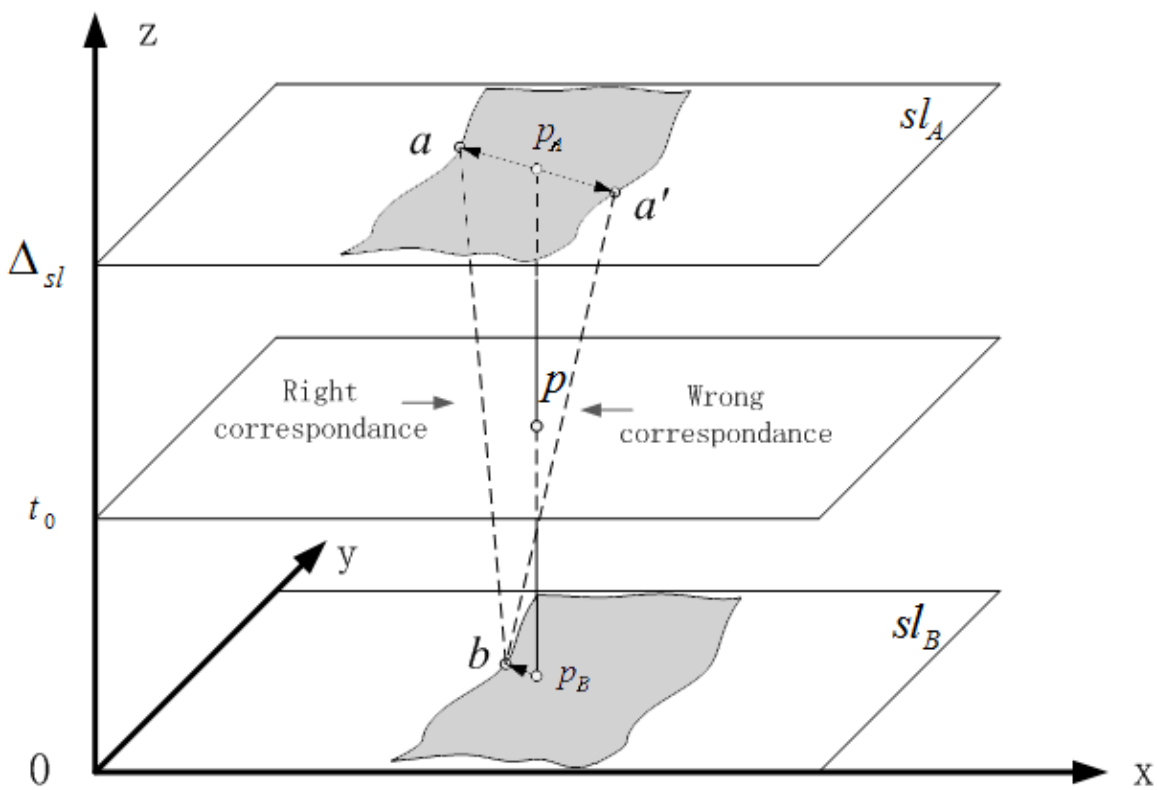

Figure 15 A schematic description to solve ambiguities of selecting normal vectors at medial points. At a medial point p_A, there is an ambiguity of the true normal vector between $\overrightarrow{p_A a}$ and $\overrightarrow{p_A a'}$. With the assumption that a local deformation is less than half the structure width, the magnitude of the deformation using the correct correspondence of a and b must be less than that of the wrong correspondence of a' and b. Therefore, $\overrightarrow{ab}$ is selected as the correct correspondence to generate the interpolation line.

The situation where the projection point p_B is a medial point may be solved similarly. Finally, a Gaussian smoothing filter of kernel size 5×5 is applied on the computed deformation field to capture larger contextual information.

3.3 Experimental Methods and Results

In this section, we describe our experimental approach to examine the performance of the tensor scale based inter-slice interpolation method. We then evaluate the accuracy of the tensor scale based method and compare the performance with current state-of-the-art methods.

The accuracy of the tensor scale based inter-slice interpolation method has been examined both qualitatively and quantitatively on phantom and real images and has been compared with a current state-of-the-art registration based method [120]. For the registration based method, both B-spline and Demons registration techniques, implemented in ITK [121], were used for comparison. For the B-spline registration based algorithm, we used the parameter setting recommended in [120]. Also, for both the B-spline registration based and Demons registration based algorithms, we used the stopping criterion as minimization of the residual errors for known truths. Thus, we experimental results presented here represent the optimum performance for the two methods in terms of iteration number. On the other hand, for the new method, no such stopping criterion or iteration number is needed.

Quantitative evaluation experiments were designed following the conventional approach [120] of evaluating an image interpolation approach. Specifically, for a given 3-D image consisting of k uniformly spaced slices, each slice except the first and the last one were removed one at a time and were regenerated from its two neighboring slices by a given method of interpolation. The error of the specific interpolation method was computed by comparing the original slice and the one obtained by interpolation. The mean absolute difference was used to measure the accuracy of the corresponding

interpolated slice. Let $I_{\text{original}}(x, y, i)$ and $I_{\text{interpolated}}(x, y, i)$, respectively, denote the original and the interpolated image intensities at the in-plane image location (x, y) on the ith slice of image of size $m \times n \times k$. The interpolation error for the ith slice, denoted as MAD_i, is computed as follows:

$$MAD_i = \frac{1}{mn} \sum_{x=1}^{m} \sum_{y=1}^{n} \left| I_{\text{original}}(x, y, i) - I_{\text{interpolated}}(x, y, i) \right|$$

Finally, the interpolation error over the entire image, denoted by MAD, is computed as:

$$MAD = \frac{1}{k-2} \sum_{i=2}^{k-1} MAD_i$$

In our experimental study, we have used both phantom and real medical images. The phantom data set was generated from the simulated brain MRI data from the BrainWeb site (http://www.bic.mni.mcgill.ca/BrainWeb). Specifically, the T1 weighted MR image (in plane size: 181×217; number of slices: 181) of anatomical model for normal brain at 0% noise, 0% intensity non-uniformity and $1 \times 1 \times 1\ \text{mm}^3$ voxel size was used. Two sets of test phantoms were generated from this simulated data. The first dataset was created by adding correlated white Gaussian noise at different SNR values while the other dataset was produced by adding different levels of intensity inhomogeneity. Ten different SNR values ranging between 50 and 10 were selected for the experiment. To examine the robustness of the method with respect to the intensity inhomogeneity, a multiplicative Gaussian inhomogeneity model was used with its center, height, and width chosen randomly. Altogether, fifteen images at different intensity inhomogeneity levels with the width of the inhomogeneity Gaussian varying between 68 and 132 mm and the height varying between 10% and 50% of the image intensity range were used for the experiment. Specifically, three Gaussian inhomogeneity images were randomly generated at varying heights, widths, and locations of the center. Each of these

initial inhomogeneity maps was multiplied by a constant α and added to the original image to obtain a test image at a given percentage of intensity inhomogeneity as defined by the following equation:

$$\text{percentage of inhomogeneity} = \alpha \times \frac{\text{max inhomogeneity intensity}}{\text{max image intensity}}$$

For a given percentage of inhomogeneity and a given initial inhomogeneity map, a test image was generated and was used for the experiment. For a given method, the error MAD_i was computed for each slice $i = 2, 3, \ldots, k-1$ in the test image. Since we used three initial inhomogeneity maps, we got three measures of MAD_i for the i-th slice and a given method at a fixed percentage of inhomogeneity; an average of these three errors was used to compute MAD and for paired t-test while comparing with results from another method.

In addition, sixteen 3-D images from different body regions and different clinical applications were used to examine the performance of our method on real data. Our first data set consists of five abdominal CT datasets from five different subjects with voxel size: $0.59 \times 0.59 \times 1.00\ \text{mm}^3$ and in-plane grid size: 512×512 with the number of slices varying between 64 and 319. For convenience, we will refer to these images as Abdomen1, Abdomen2,…,Abdomen5, respectively. Our next data set included CT images of four cadaveric ankle specimens scanned with a Siemens Sensation 64 Multi-slice CT scanner at 120 kVp and 140 mAs (voxel size: $0.21 \times 0.21 \times 0.3\ \text{mm}^3$) adequately displaying trabecular bone micro-architecture. For these images, the common in-plane image grid size was 512×512 and the number of slices varied between 334 and 336. We will refer to these images as Ankle1, Ankle2, Ankle3, and Ankle4, respectively. The last group consisted of seven pulmonary CT images from seven different subjects scanned on a Siemens Sensation 64 Multi-slice CT scanner at 120 kVp and 200 mAs yielding $0.55 \times 0.55 \times 0.5\ \text{mm}^3$. The in-plane grid size for these images was 512×512 and the numbers of slices varied between 519 and 728. These images will be referred to

as Lung1, Lung2, …, Lung7. Ankle and lung data sets were chosen to evaluate the performance of an algorithm under changing topology and shapes of micro-structures along the slice direction. For each of the phantom as well as medical data, the overall interpolation error was compared by analyzing their MAD values. The errors on individual slices were computed for different methods and paired t-tests were performed to evaluate statistical reliability of differences in overall interpolation errors by different methods. The p-value of 0.01 was considered significant.

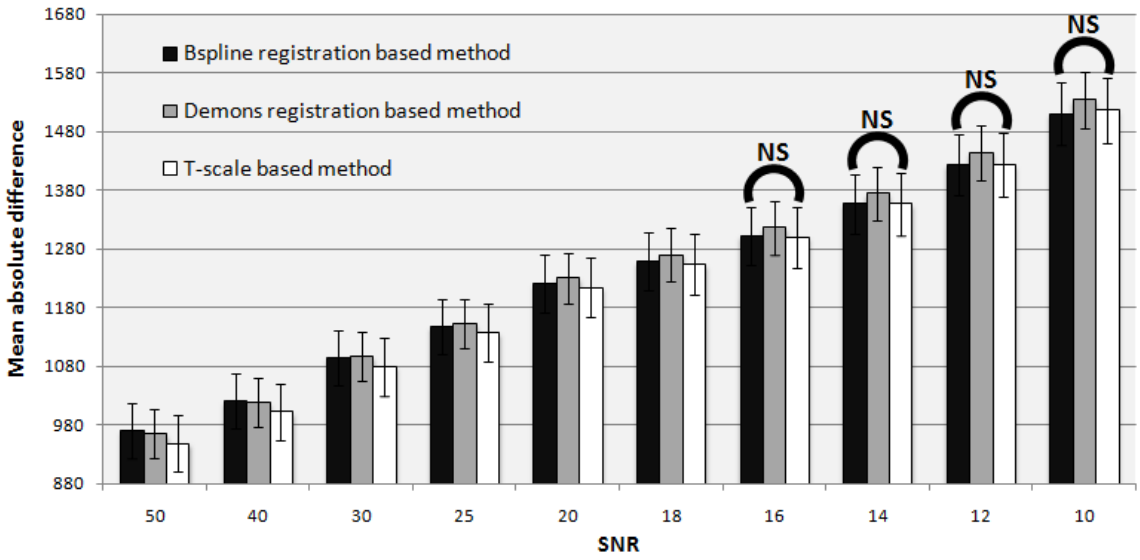

Figure 16 Performance of three interpolation methods on the BrainWeb phantom dataset with additive white Gaussian noise at various levels of signal-to-noise ratio. The mean error was computed as the MAD value over the entire image while the standard deviation of errors was computed as the standard deviation of MAD_i values from individual slices. As compared with the two registration based methods, the new method outperforms both of them except for the four cases for which the differences between the B-spline and the new method are statistically identical - marked with "NS" (non-significant).

Here, we present results of the experiments to compare the new interpolation methods with two registration based methods using B-spline and Demons techniques at

various levels of added noise and intensity inhomogeneity on the BrainWeb phantom dataset. The tensor scale here is based on algorithmic approach as shown in [13]. Results of quantitative analysis for three different methods at various noise levels are presented in Figure 16. At every level of noise, the tensor scale based interpolation method has outperformed the demons registration based method and the results are found to be statistically significant using a paired t-test. As compared with the B-spline registration based method, the new method has outperformed (p-value < 0.01) at all levels of noise except at SNR = 10, 12, 14, and 16 where interpolation errors by the two methods are not statistically different.

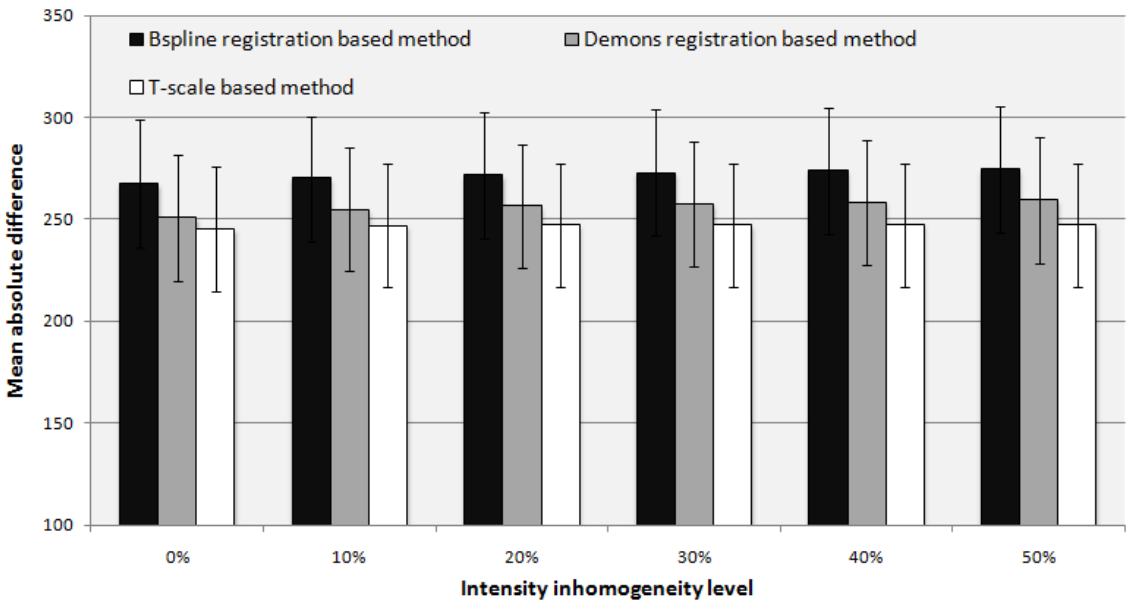

Figure 17 Performance of three interpolation methods on the BrainWeb phantom dataset with different multiplicative Gaussian intensity inhomogeneity added. The mean error was computed as the MAD value over the entire image while the standard deviation of errors was computed as the standard deviation of MAD_i values from individual slices. MAD_i represents the average interpolation errors on the i-th slice for three different inhomogeneity maps at a fixed percentage of inhomogeneity.

These results indicate, that although the tensor scale based method outperforms the two registration based methods, the overall difference in performance is reduced with increasing noise. A possible argument behind the observation is that the closed form equation for the interpolation line in tensor scale based approach uses the tensor scale of only two points, one from each adjacent slice. Thus, the approach has less strength for statistical noise smoothing as compared to the two registration-based methods and the performance of the current tensor scale based registration method on high noisy images may be a limitation. A possible way for improving the performance of the tensor scale based method may be to amalgamate the closed form solution into the registration framework.

Comparative results of the three methods at various levels of image inhomogeneity are presented in Figure 17. It may be noted from these results that effects of image inhomogeneity for all three method are minimal which was expected as intensity inhomogeneity has only limited effects on local structural information in an image. Also, it is important to note that at all examples of inhomogeneity, the tensor scale based interpolation method has outperformed the two registration based methods (p-value < 0.01). Here, it may be observed from Figure 16 and Figure 17 that the standard deviation values are somewhat high as compared to the corresponding differences of MAD values. Yet, the p-values indicated statistical significance of the measured differences in errors which is associated with a proper use of a paired t-test. The results of these experiments suggest that although there are significant variations in interpolation errors from one slice to another, the differences in performance for two methods are consistent from one experiment to another.

Results of applications of the three methods on several medical images are illustrated and visually compared in Figure 18 to Figure 20.

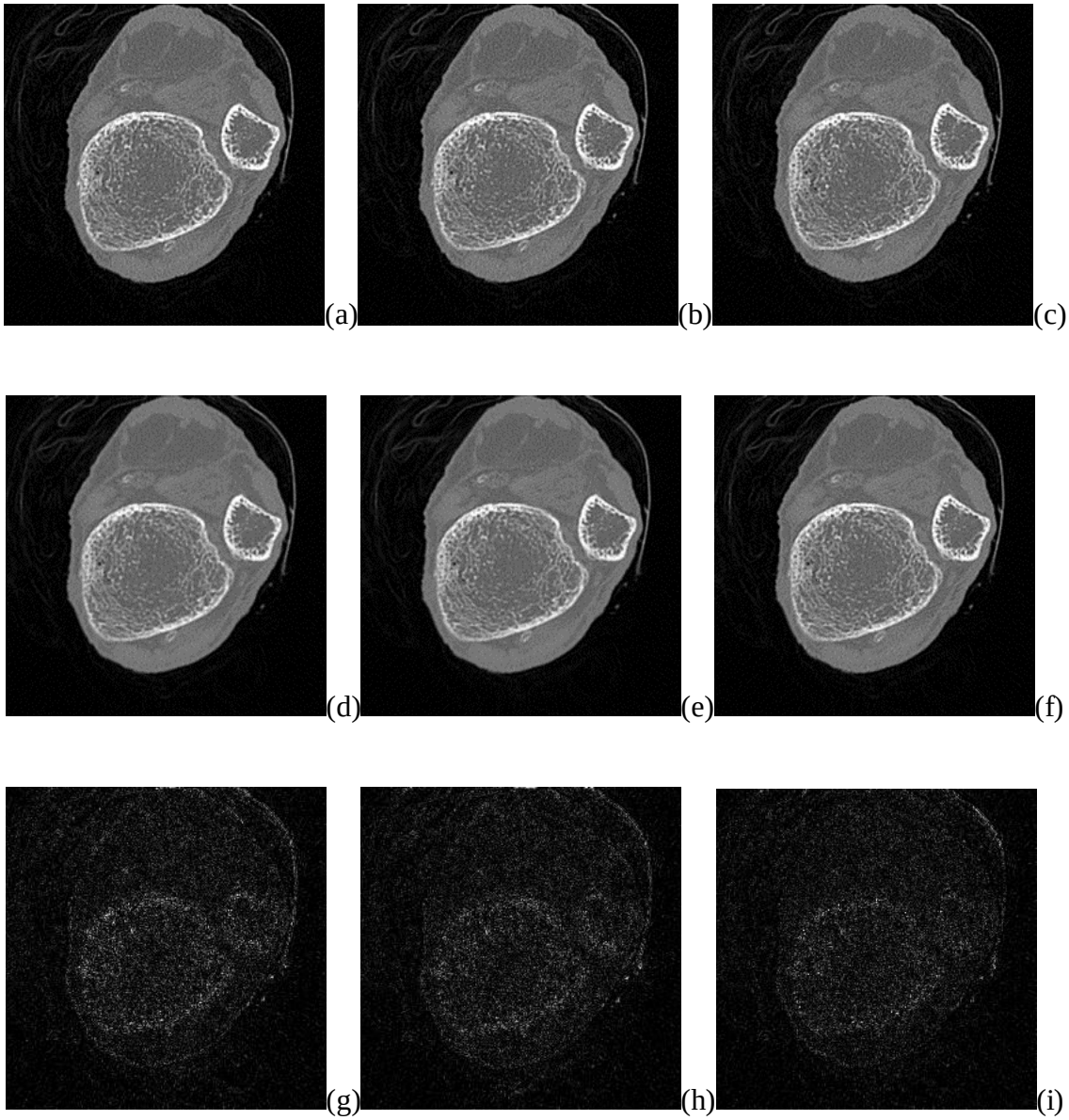

Figure 18 Results of applications of different interpolation methods on the ankle CT data Ankle1. (a-c) Three consecutive image slices from the original data. (d-f) Interpolated results for the central image slice (b) from the two adjacent slices (a,c) using B-spline (d) and Demons (e) based registration methods and the tensor scale based method (f). (g-i) Absolute errors by corresponding interpolation method as computed by comparing with the original image slice. Interpolation error is reduced using the tensor scale method (p-value < 0.01).

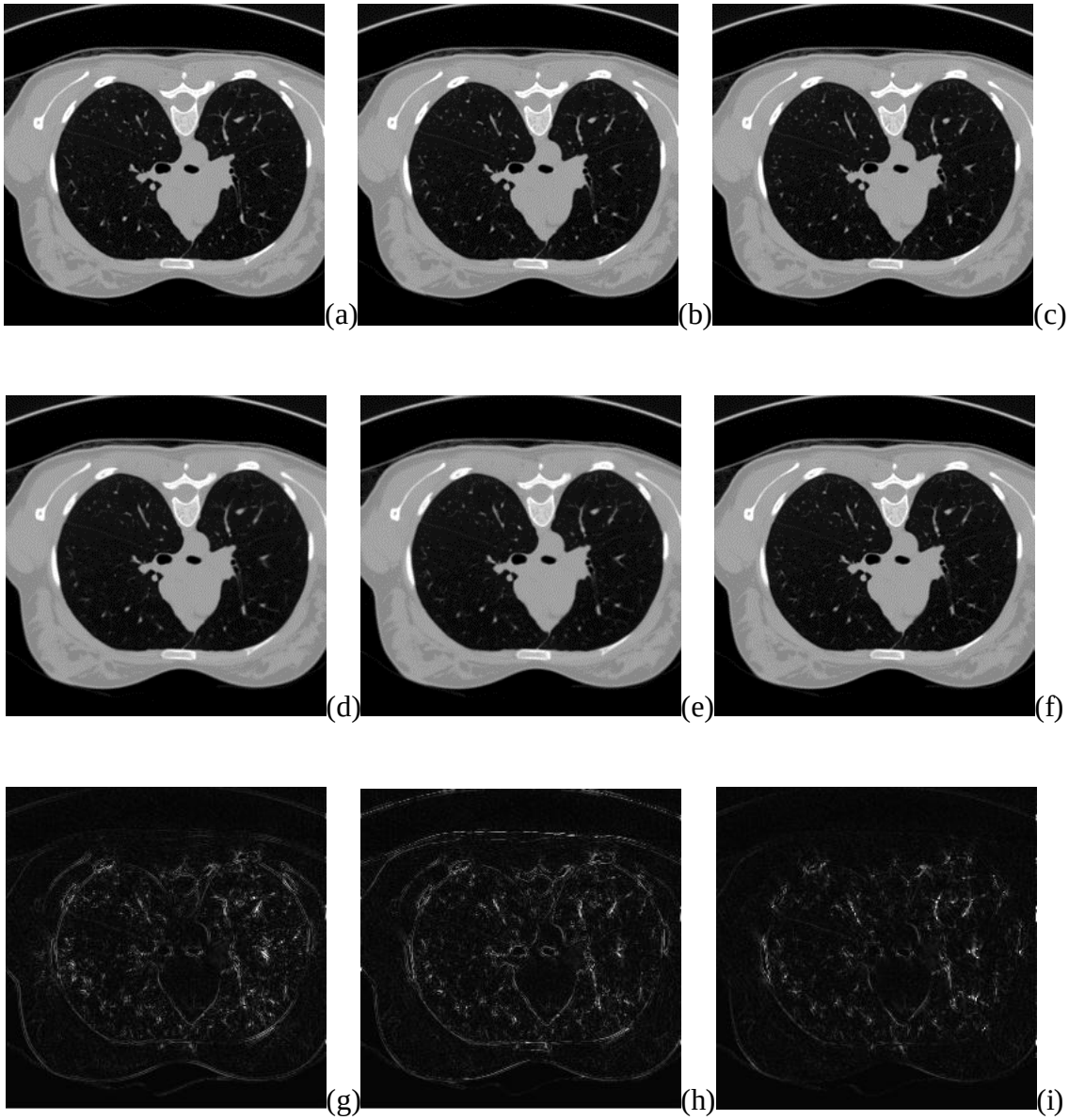

Figure 19 Same as Figure 18 but for three consecutive image slices from the pulmonary CT image Lung1 at 0.5 mm slice thickness.

In each of these Figures, the top row show three consecutive image slices from the specific dataset. The middle row presents the interpolated results for the central slice of the top row computed by three different methods using the left and right image slices of the top row. The last row indicates the absolute error maps for corresponding

interpolated result as compared with the original image slice. In the middle and last rows, the images on the left and central columns represent the results of B-spline and Demons based registration based methods. The right column presents the results of the tensor scale based method.

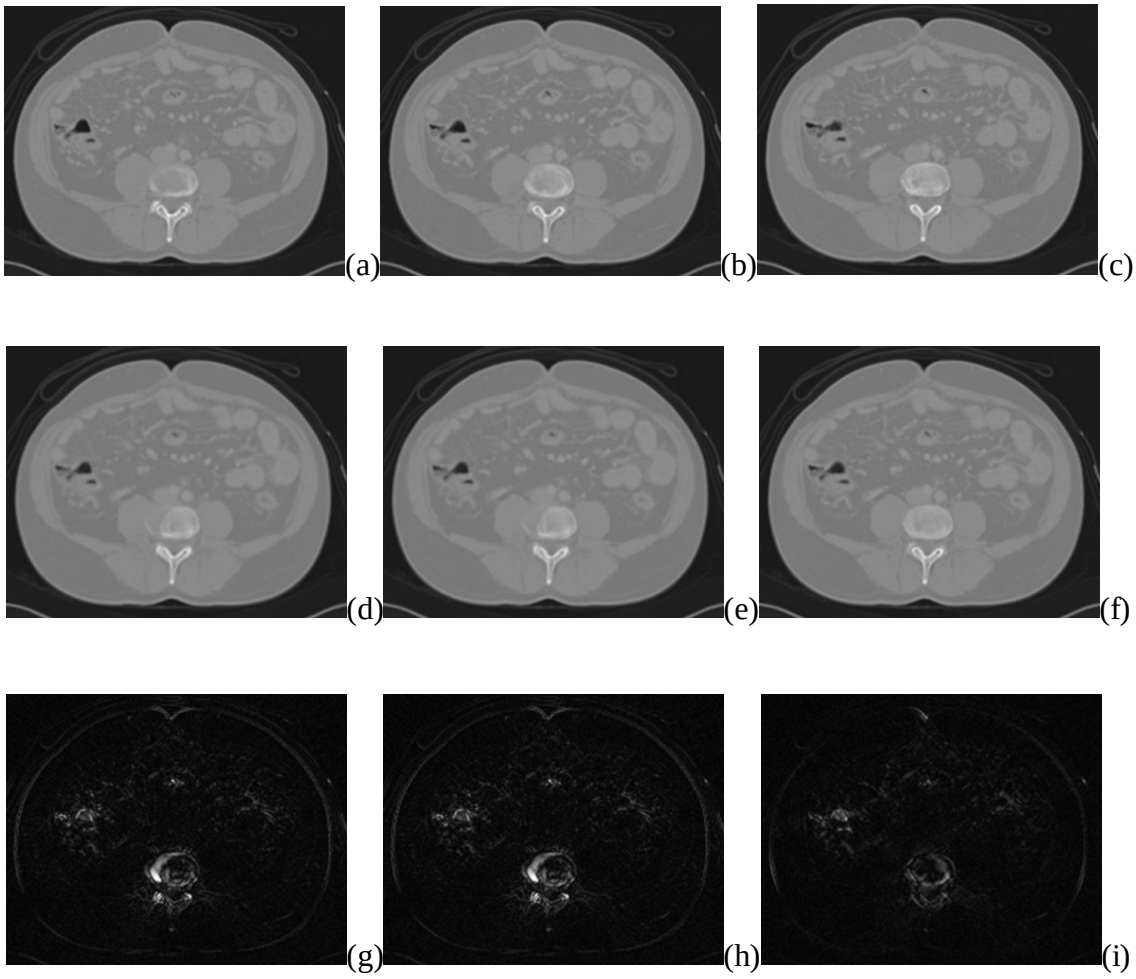

Figure 20 Same as Figure 18 but for three consecutive image slices from the lower abdominal CT image Abdomen1 at 1mm slice thickness.

In all these examples, reduction of interpolation errors by the tensor scale based method is visually notable. For the example of Figure 18, it may be noted that all

methods including the tensor scale based algorithm produce high concentration of interpolations errors in the trabecular bone region. These errors are primarily contributed by the high-frequency changes in trabecular bone topology from one slice to another. Similar to other algorithms, tensor scale based registration method may fail to compensate for large topological variations from one slice to another. A quantitative analysis of the results is presented in Figure 21 which indicates the mean and standard deviation of interpolation errors by three methods for different medical images.

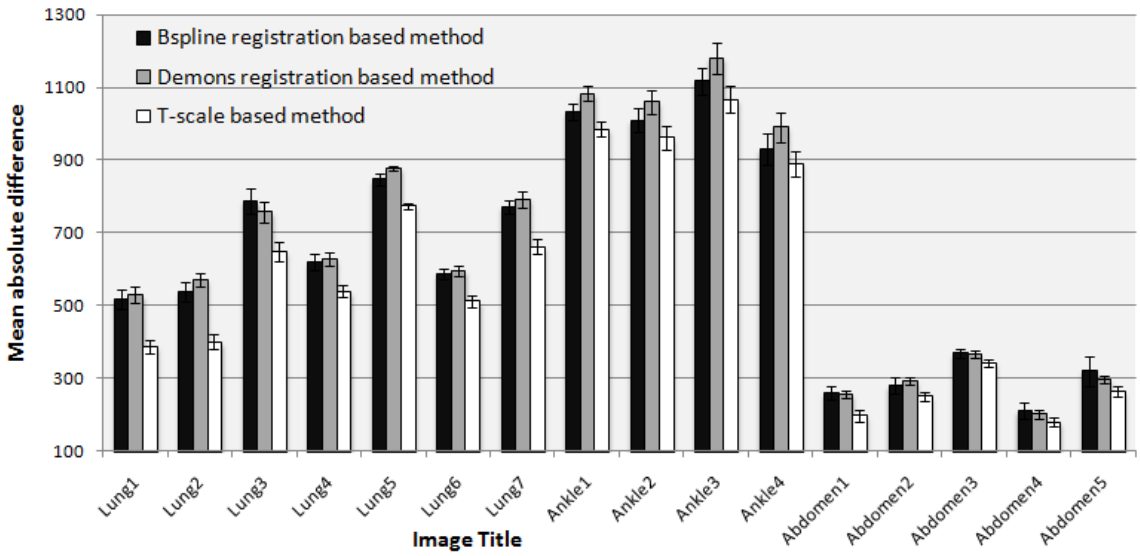

Figure 21 Performance of three interpolation methods on sixteen different medical images selected from different clinical applications. The mean error was computed as the MAD value over the entire image while the standard deviation of errors was computed as the standard deviation of MAD_i values from individual slices. For all examples, the tensor scale based method has outperformed the two registration based methods (p-value < 0.01).

The mean error was computed as the MAD value over the entire image while the standard deviation of errors was computed as the standard deviation of MAD_i values from individual slices. As observed in this figure, the tensor scale based method has always

outperformed the other two methods with a clear margin. It may be interesting to observe from the quantitative results that, across all data and methods, the standard deviation values are small as compared to corresponding mean error. It indicates that the interpolation error is a highly reliable parameter to determine the quality of individual methods. Also, a paired t-test of errors over individual image slices was performed between tensor scale based methods and each of the two registration based methods. The results of every paired t-test comparing the performance of the tensor scale and another method demonstrated the superiority of the tensor scale method p-value < 0.01, see Figure 21. Further, it may be observed that errors for ankle and pulmonary images are relatively larger as compared to abdominal images. Possibly, it is caused by rapid changes in both topology and geometry of trabecular bone in ankle images and both airways and vasculature in pulmonary images.

3.4 Conclusion

In this chapter, we investigated an application of tensor scale to medical image inter-slice interpolation. A closed form solution for computing interpolation lines using tensor scale has been introduced which has contributed to a new tensor scale based interpolation algorithm. Experimental results have demonstrated that the new interpolation method outperforms state-of-the-art registration based interpolation techniques on real clinical images and the statistical significance of the improvements was observed.

CHAPTER 4

TENSOR SCALE BASED DIFFUSION IMAGE FILTERING

4.1 Introduction

In this chapter, we first describe a tensor scale based diffusion filtering that is primarily developed on the theory of anisotropic diffusion originally proposed by Perona and Malik [14] and subsequently, studied by others [9, 122]. The basic objective of our tensor scale based filtering is to govern the diffusion process in a space-variant and orientation-dependent fashion to optimally fit with local image structures captured in the form of tensor scale. Subsequently, experimental plans and results are provided to evaluate the performance of the method. Specifically, the algorithm has been applied to both 2- and 3-D geometric phantoms and real images, and its performance on reducing noise as well as preserving structures is examined and compared with those of gradient and structure tensor based anisotropic diffusion methods. Experimental results have established the superiority of the new tensor scale based method as compared to existing filtering algorithms.

In the following, I will first present detailed algorithm for anisotropic diffusion filtering followed by experimental plans and methods. Finally, results are given and concluding remarks are drawn.

4.2 Tensor Scale Based Diffusion Filtering

4.2.1 Anisotropic Diffusion Filtering

Anisotropic diffusion [14] was originally described to encourage diffusion within a region (characterized by low intensity gradients) while discouraging it across object boundaries (characterized by high intensity gradients). The anisotropic diffusion process at any spel p may be defined as follows:

$$\frac{\partial f}{\partial t} = \operatorname{div} \mathbf{V} = \lim_{\Delta\tau \to 0} \int_s \mathbf{V} \cdot \mathrm{d}\mathbf{s},$$

where f is image intensity function; t is time variable; "div" is divergence operator; $\mathbf{V} = G\mathbf{F}$ is diffusion flow vector; G is diffusion conductance function; $\mathbf{F}$ is intensity gradient vector; $\Delta\tau$ is the volume enclosed by the surface s surrounding p; and $\mathrm{d}\mathbf{s} = \mathbf{u}\,\mathrm{d}s$ where $\mathbf{u}$ is a unit vector which is orthogonal and outward-directed with respect to the infinitesimal surface element $\mathrm{d}s$. The key idea of anisotropic diffusion [14] is to spatially vary the conductance by a nonlinear and non-increasing function of gradient magnitude, e.g. $G = \exp(-|\mathbf{F}|^2/2\sigma^2)$ where σ is the controlling parameter. See Figure 22 for a valid shape of conductance function with gradient magnitude and the resultant relationship between the magnitudes of gradient and flow.

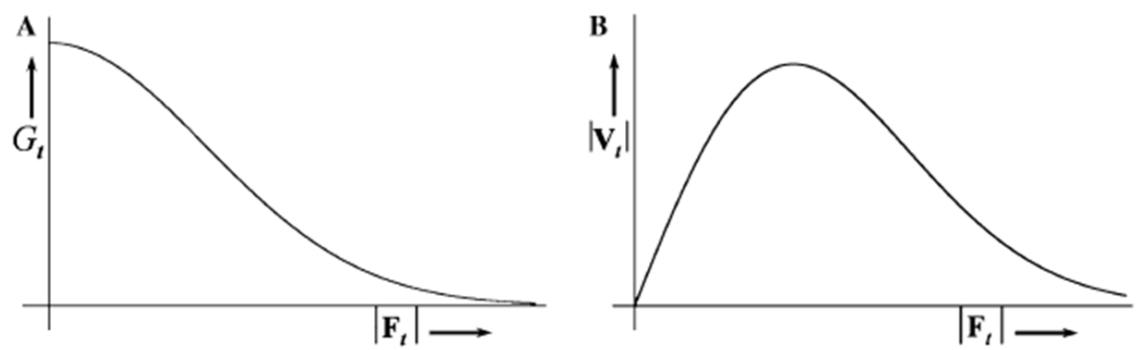

Figure 22 The shapes of diffusion conductance (A) and diffusion flow magnitude (B) functions, respectively, with gradient magnitudes complying with the basic idea behind anisotropic diffusion [14].

Guided by the above theory, a diffusion filtering process in a digital image is formulated as an iterative process as follows:

$$f_t(p) = \begin{cases} f(p), & \text{if } t = 0, \\ f_{t-1}(p) - K_D \sum_{q \in C} \mu_\alpha(p,q)\mathbf{V}_{t-1}(p,q) \cdot \mathbf{D}(p,q), & \text{otherwise,} \end{cases}$$

where, f_t represents image intensity at the tth iteration; μ_α is pixel adjacency relation; K_D is a diffusion constant; $\mathbf{V}_{t-1}$ is intensity flow vector at $(t-1)^{th}$ iteration; and $\mathbf{D}(p,q)$ is unit vector along the direction from p to q; and '·' is the vector dot product operator. Under a uniform pixel adjacency relation, the diffusion constant K_D should satisfy the following inequality to ensure a monotonic intensity variation with iterations:

$$K_D \leq \frac{1}{\sum_{q \in Z^2} \mu_\alpha(p,q)}, \qquad \text{where } p \in Z^2.$$

Using standard 26-adjacency in 3-D, K_D = 1/27. The flow vector V_t is determined by the following equation:

$$\mathbf{V}_t(p,q) = G_t(p,q)\mathbf{F}_t(p,q),$$

where,

$$\mathbf{F}_t(p,q) = \frac{f_t(p) - f_t(q)}{|\mathbf{p} - \mathbf{q}|}\mathbf{D}(p,q),$$

and G_t is an orientation- and space-adaptive conductance function at t^{th} iteration. As mentioned before, G_t should be a nonlinear function (see Figure 22) of local intensity gradient $\mathbf{F}_t$ that eventually leads to a non-monotonic behavior of flow with gradients. Gaussian functions, as follows, have popularly been used for G_t

$$G_t(p,q) = e^{-\frac{|\mathbf{F}(p,q)|^2}{2[\sigma(p,q)]^2}},$$

where σ is the control parameter determining the degree of filtering. When σ is large, the degree of filtering is high and possibilities of blurring across boundaries and of smearing out regions containing fine detail increase. On the other hand, when σ is small, the filtering process performs conservatively and more noise survive after filtering.

4.2.2 Tensor Scale Based Conductance

In conventional diffusion filtering methods [14, 122], diffusion process adapts to local structure orientation using gradient information while the diffusion parameter σ is kept fixed that limits the fine control on and adaptivity to local image structural

properties. Weickert *et al.* [29] introduced the notion of structure tensor to control this parameter and demonstrated its use in along structure smoothing. The motivation of our work is to use geometric tensor information of local structures in filtering that facilitates along structure smoothing while preserving boundary sharpness as shown in Figure 23. Specifically, the controlling parameter σ is determined by local tensor scale in a space- and direction-variant manner as follows:

$$\sigma(p,q) = \sigma_{\min} + \chi\left(\max\left(\zeta_p(q), \zeta_q(p)\right)\right) \times \sigma_\psi.$$

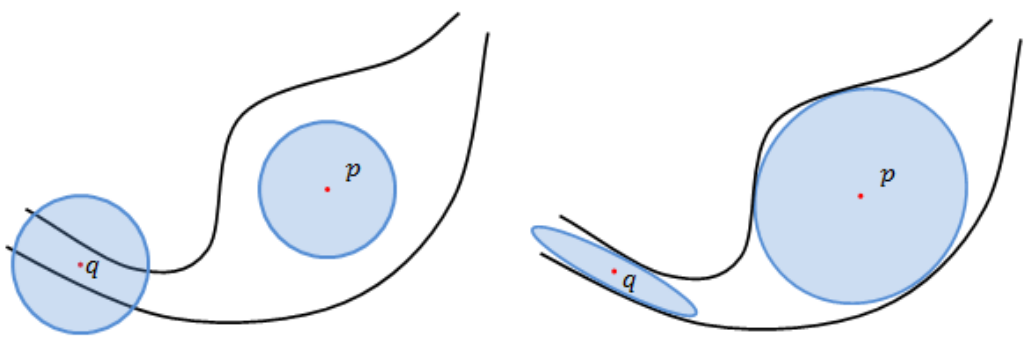

(a) (b)

Figure 23 Behavior of the Gaussian mapping involved in the conductance function calculation: (a) controlling parameter is kept fixed over the entire image and the mapping is isotropic everywhere; (b) tensor scale controlled conductance function helps to achieve anisotropic dynamic conductance value so that the diffusion process is guided in a direction variant manner.

The above formulation ensures a minimum diffusion of $\sigma_{\min}$ during the filtering process; the second component of the expression uses a monotonically non-decreasing function χ to control local diffusion process in a direction-variant manner using the two tensor scale derived parameters $\zeta_p(q)$ and $\zeta_q(p)$. The term σ_ψ determines the sensitivity of the diffusion process with local tensor scale parameters. The tensor scale parameter $\zeta_p(q)$ is defined as follows:

$$\zeta_p(q) = \sqrt{\mathbf{i}_{pq}^{\mathrm{T}} T(p) \mathbf{i}_{pq}},$$

where $\mathbf{i}_{pq}$ is the unit vector along the direction from p to q. Note that, by considering tensor scale $T(p)$ as a co-variance matrix, the parameter $\zeta_p(q)$ gives the square root of the variance of the system along the vector $\mathbf{i}_{pq}$. Here, $\zeta_p(q)$ is treated as an approximate measure of the radial length of the ellipsoid $T(p)$ along the direction $\mathbf{i}_{pq}$. In this paper, we have used the following functional form for χ

$$\chi(x) = e^{-\frac{x^2}{2\sigma_L^2}},$$

where σ_L is the maximum expected radial length of tensor scale ellipse computed as the maximum DT value in the image. In all experimental results presented, the parameters σ_ψ is determined as the overall noise level in the image computed in the same way as described in [9]; the value the parameter $\sigma_{\min}$ is chosen as 25% of the value of σ_ψ. Finally, for all experimental results the filtering process was run for twenty iterations.

4.3 Experimental Methods and Results

In this section, we describe our experimental approach to examine the performance of the tensor scale based anisotropic diffusion filtering method. We then evaluate it in terms of residual noise relative contrast and compare the performance with gradient and structure tensor based anisotropic diffusion method on both 2-D and 3-D images.

The purpose of the experiment is to examine the performance of tensor scale based filtering methods as compared to intensity based and structure tensor based diffusion filtering algorithms. ITK implementation [121] of gradient-based diffusion filtering and their recommended values of 0.125, 3.0 and 5 were used for the time step, conductance parameter and the iteration number for 3-D image. An algorithm was implemented for structure based diffusion filtering in accordance to the description of [29] and the parameter value settings of 0.001 for regularization parameter α, 1 for

threshold parameter C, 0.3 for noise scale σ, 2 for integration scale ρ, and 10 for iteration time t were used as suggested by the author. Three image sets were used in this experiment – (1) one large 3-D phantom image containing different geometric structure at various structure-scales as well as various separations scale, (2) a photographic image of an aquarium and (3) five lung CT images of human subjects. Both phantom and CT images were corrupted with five different levels of noise (8% to 20%) and different filtering algorithms were applied to the noisy images to qualitatively evaluate their performance. A measure of residual noise was used to assess the performance a method and also, a measure of structure blurring was examined for the phantom image since the knowledge of structures is needed define this measure.

Let I be an original phantom or lung image; I was corrupted by adding a zero-mean Gaussian noise n generating a noisy test image $I_n = I + n$. Noise level was defined over the test region Ω in an image as follows:

$$\text{noise\%} = \sqrt{\frac{\sum_{p\in\Omega} n^2(p)}{\sum_{p\in\Omega} I^2(p)}}.$$

It may be noted that percent of noise is essentially an inverse measure of signal to noise ration or SNR widely used as a measure of noise level. Let I_{nF} denote the image obtained by applying a filtering algorithm to the noisy image I_n. Thus the residual noise in the filtered image is $n_r = I_{nF} - I$, and an overall measure of residual noise is defined as follows:

$$\text{noise}_r\% = \sqrt{\frac{\sum_{p\in\Omega} n_r^2(p)}{\sum_{p\in\Omega} I^2(p)}}.$$

Here, measurements are calculated for VOIs in the experimental images, from each pulmonary CT image and phantom image, fifty VOIs, each of size 50×50×50 voxels, will be randomly selected inside a lung region giving a total of 250 VOIs.

Relative contrast is defined for the phantom image to measure structure preserving property of a filtering method in terms of object to background contrast relative to residual noise. Let Oj and Bj denote the set of object and background pixels in a phantom image that are no further than m pixels from the object/background interface. Such pixels are identified in a binary image using standard morphological operations. We did not use the entire object/background regions for measure relative contrast as the notion of structure blurring is absent in deep interior and thus, inclusion of such regions in analysis only reduces the sensitivity of the measurement. The performance of different methods was analyzed for two values of 1 and 2 for m. Finally, the relative contrast in an image I is defined as

$$\mathrm{RC} = \frac{\left|\mu_{Oj} - \mu_{Bj}\right|}{\sqrt{\sigma_{Oj}\sigma_{Bj}}}$$

where μ_{Oj} and σ_{Oj} are the mean and standard deviation of intensities over Oj while μ_{Bj} and σ_{Bj} denote same entities over Bj. Here, relative contrast measurements are calculated along boundaries of geometric structures, background and object regions on either of the boundary are identified with different radius (for our experiment, radius of 1 and 2 voxels are examined) based on original binary phantom data and RC is calculated respectively.

Figure 24 illustrates results of three filtering algorithms on a photographic image of a fish in an aquarium containing visible noise. Results of application of the three filtering algorithms are presented in Figure 24(b-d). As observed in these figures, among the three results, the maximum visual perceptual noise cleaning and boundary sharpening is achieved using the tensor scale based method (Figure 24(d)). This observation is confirmed in enlarged views (Figure 24(e-h)) of a small box selected from the matching region in the original and the three filtered images.

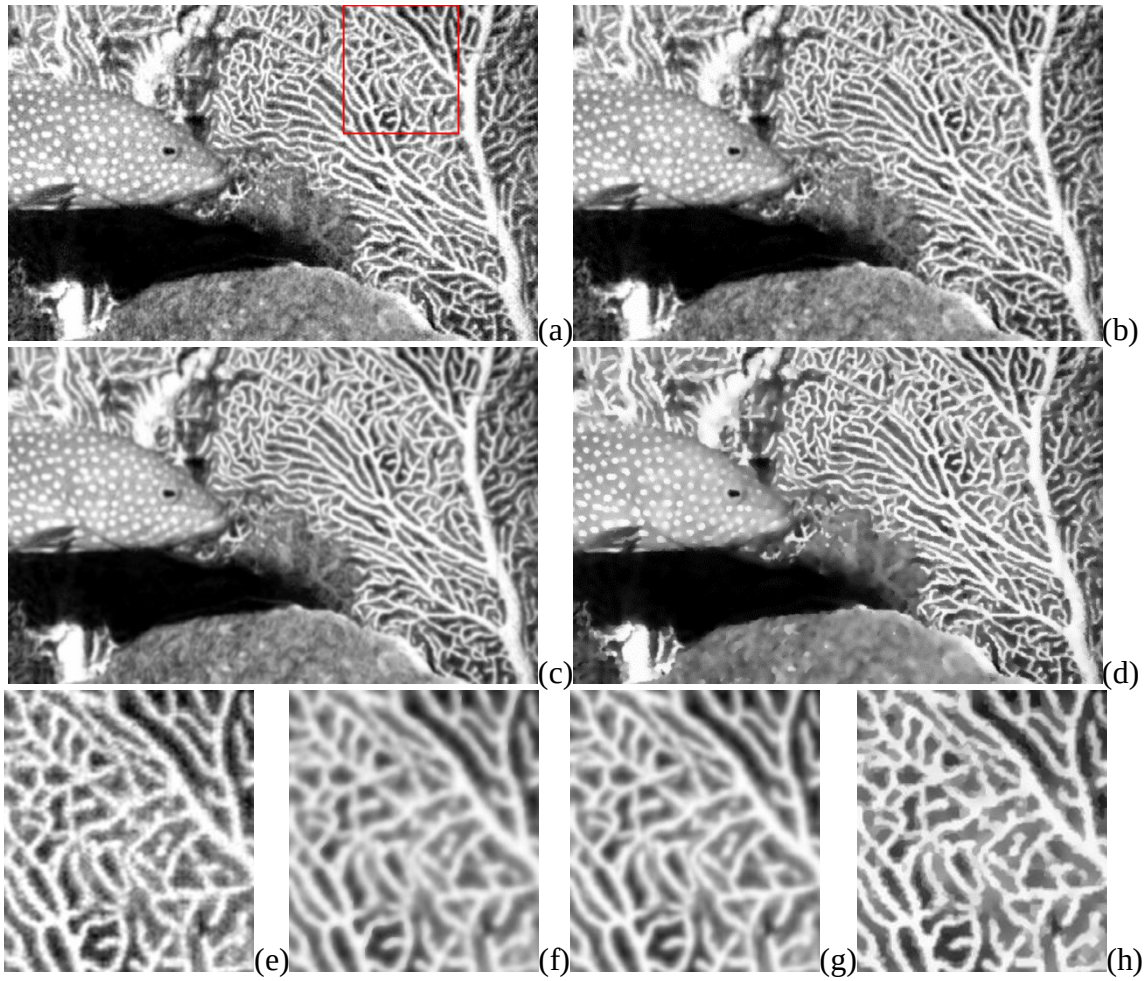

Figure 24 A qualitative comparison among different diffusion filtering methods. (a) The original digital image with natural noise. (b-d) Smooth images obtained by using gradient (b), structure tensor (c) and tensor scale (d) based diffusion filtering methods. (e-h) Zoomed in displays of the matching region cropped from (a-d), respectively. It may be noted that the tensor scale based method has outperformed the other two methods in smoothing along the structures while preserving boundaries and effect is more prominent in the zoomed displays in (e-h).

Figure 25 illustrates results of different filtering methods on a 2-D phantom image. As observed in the Figure, at the finest scale, the gradient and structure tensor based filtering algorithms have failed to maintain the separate identity of the three sinusoidal curves at several locations. On the other hand, the tensor scale based algorithm has

successfully preserved the separation of the three curves at the finest scale while maximally reducing noise over homogenous regions.

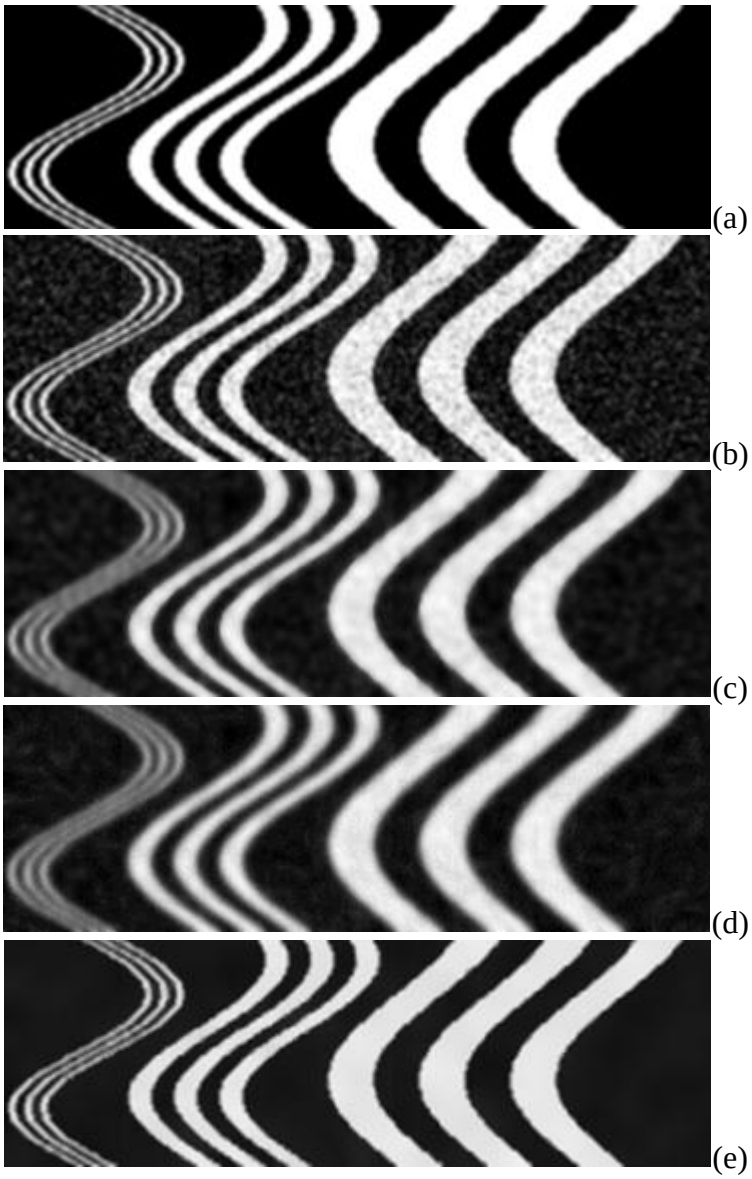

Figure 25 Comparative results of image filtering in a 2-D phantom. (a) The original phantom image. (b) Degraded image after adding Gaussian white noise. (c-e) Results of gradient (c), structure tensor (d) and tensor scale based (e) anisotropic diffusion filtering methods.

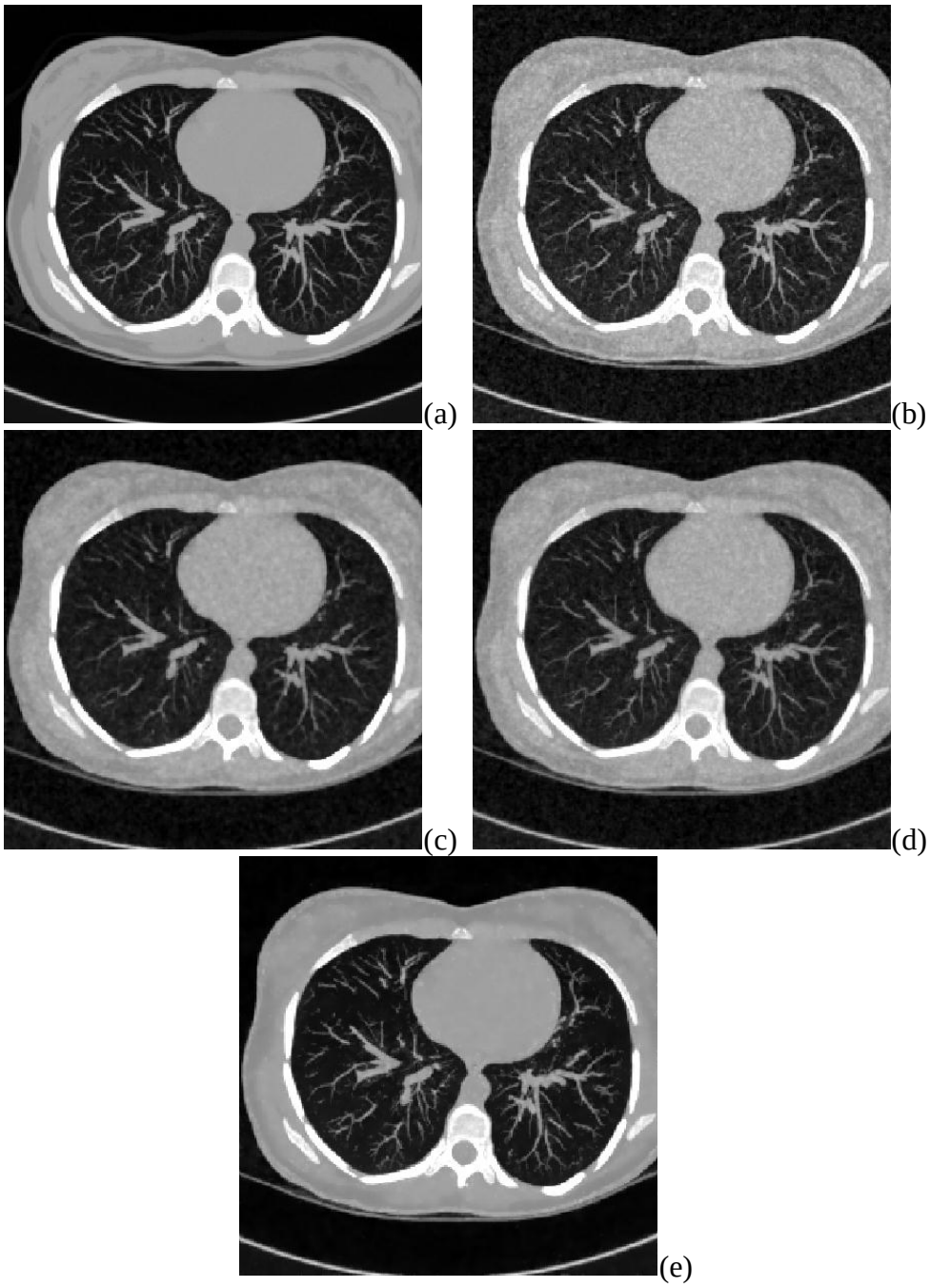

Figure 26 Results of 3-D image filtering. (a) An original image slice from a pulmonary CT image of a patient. (b) Degraded image after adding Gaussian white noise. (c-e) Results of 3-D image filtering using gradient (c), structure tensor (d) and tensor scale (e) based diffusion.

Table 4 Results of quantitative comparison among three different methods in terms of residual noise after filtering on different images.

Image	*Original Noise(%)*	*Residual Noise(%)*		
		G-algorithm	S-algorithm	T-algorithm
3-D Phantom	8.0	7.8	7.7	5.9
	10.0	9.5	9.5	6.8
	12.0	11.1	11.3	7.8
	15.0	13.6	13.7	9.3
	20.0	17.3	17.8	11.4
3-D Lung CT-Data 1	8.0	7.5	8.7	4.4
	10.0	7.7	9.3	5.3
	12.0	9.5	9.9	5.9
	15.0	11.7	10.9	7.0
	20.0	14.8	14.5	9.4
3-D Lung CT-Data 2	8.0	7.3	7.5	4.8
	10.0	9.0	9.4	5.9
	12.0	10.7	11.1	6.5
	15.0	13.5	14.0	9.2
	20.0	17.9	18.0	10.7
3-D Lung CT-Data 3	8.0	7.2	7.5	4.6
	10.0	9.1	9.3	6.0
	12.0	10.8	11.2	6.8
	15.0	13.6	14.1	9.5
	20.0	18.0	18.6	11.7
3-D Lung CT-Data 4	8.0	7.4	7.6	5.0
	10.0	9.1	9.4	5.7
	12.0	10.5	10.9	6.4
	15.0	13.2	13.7	9.0
	20.0	17.7	18.2	10.8
3-D Lung CT-Data 5	8.0	7.3	7.4	4.5
	10.0	8.9	9.2	5.5
	12.0	10.4	10.7	6.3
	15.0	12.9	13.2	8.9
	20.0	17.1	17.6	10.1

Figure 26 illustrates the results of three filtering methods on a 3-D pulmonary CT image. Figure 26(a) presents an axial image slice from the original CT data; here, a maximum intensity projection (MIP) display of the image region covering ±10 image slices around the target slice is used to depict partial 3-D information of the local pulmonary vasculature. The same image region after adding a 12% white Gaussian noise is shown in Figure 26(b) while the results of gradient, structure tensor and tensor scale based filtering algorithms are presented in Figure 26(c-e). As observed in these results, the diffusion filtering algorithm has reduced some noise (Figure 26(c)) although, it has blurred fine structures at several locations and also the residual noise is visually apparent. While the structure blurring is visually less prominent using the structure tensor based method (Figure 26(d)), the presence of residual noise is visible and the peripheral vessels are visually blurred. On the other hand, the tensor scale based filtering algorithm has successfully cleaned noise (Figure 26(e)) while preserving almost every fine structure visible in Figure 26(a).

Table 5 Results of quantitative comparison among three different methods in terms of relative contrast after filtering on 3-D phantom image.

Radius	*Original Relative Contrast*	*Relative Contrast After Filtering*		
		G-algorithm	S-algorithm	T-algorithm
1 voxel	9.1	8.3	8.1	9.5
	8.6	7.1	7.7	9.0
	8.0	7.3	7.3	8.5
	7.1	6.1	6.7	7.8
	6.0	4.9	5.5	6.7
2 voxels	9.8	8.6	8.4	10.5
	9.2	7.3	8.0	10.1
	8.6	7.7	7.7	9.4
	7.7	6.5	7.1	8.8
	6.5	5.3	5.9	7.6

The superiority of the tensor scale based filtering method on the phantom image is further confirmed in the results of quantitative analysis in Table 5 where the tensor scale based method has achieved minimum residual noise and maximum enhancement in relative contrast measures among all three method algorithms. In these tables, G-, S- and T-algorithms are used as abbreviations for gradient, structure tensor and tensor scale based diffusion filtering algorithms. As shown in the result, the fact that the relative contrast result given by tensor scale based method is higher than the value before filtering can be served as the evidence that tensor scale based method is capable of reducing noise in an image while preserve the structure boundary.

4.4 Conclusion

In this chapter, we investigated an application of tensor scale to anisotropic diffusion image filtering. Tensor scale generates an optimal scale parameter that fits with local image structures and governs the diffusion process in a space-variant and orientation dependent fashion. The performance of tensor scale based filtering has been compared with gradient and structure tensor based diffusion filtering algorithms and both qualitative and quantitative results have demonstrated improvements in image filtering using tensor scale.

CHAPTER 5

TENSOR SCALE BASED *N*-LINEAR INTERPOLATION

5.1 Introduction

In this chapter, a new *n*-linear method based on tensor scale is introduced. The basic idea is to bring the notion of an anisotropic space where distance increases slower along the direction of the local structure while it decreases slowly across it. Experimental plans and results to examine the performance of the method are then discussed. Specifically, the algorithm has been applied to 3-D phantom image containing different geometric structure at various structure scales and several 3-D medical images. The performance of tensor scale based *n*-linear interpolation is compared with standard *n*-linear and windowed Sinc interpolation results. Experimental results have shown a clear improvement using tensor scale in *n*-linear interpolation.

In the following, detailed algorithm for tensor scale based *n*-linear interpolation is first presented followed by experimental plans and methods. Finally, results are given and concluding remarks are drawn.

5.2 Tensor Scale Based *n*-linear Image Interpolation

Linear interpolation is a widely used technique for image resampling. In a 1-D discrete signal, the linear interpolation in between two successive sample values is defined by the straight line joining the sample points. In an n-D digital image, image intensity values are known at spels $p \in \mathbb{Z}^n$ with integral co-ordinate values. Following the principle of linear interpolation, the intensity value at a location $p_c \in \mathbb{R}^n$ with unconstrained co-ordinate values is determined as a weighted sum of intensity values at 2^n vertices of the binding box of $p_c = (x_1, x_2, \dots, x_n)$. Let $\lfloor\cdot\rfloor$ and $\lceil\cdot\rceil$ be the floor and ceiling operators, then the vertices of the binding box of p_c are $p_1 = (\lfloor x_1\rfloor, \lfloor x_2\rfloor, \dots, \lfloor x_n\rfloor)$, $, p_2 = (\lceil x_1\rceil, \lfloor x_2\rfloor, \dots, \lfloor x_n\rfloor)$, $\dots, , p_{2^n} = (\lceil x_1\rceil, \lceil x_2\rceil, \dots, \lceil x_n\rceil)$. The estimated intensity value at p_c is given as follows:

$$f(p_c) = \frac{\sum_{i=1}^{2^n} w_i f(p_i)}{\sum_{i=1}^{2^n} w_i},$$

where,

$$w_1 = \prod_{j=1}^{n} (\lceil x_j \rceil - x_j), w_2 = (x_1 - \lfloor x_1 \rfloor) \prod_{j=2}^{n} (\lceil x_j \rceil - x_j), \ldots, w_{2^n} = \prod_{j=1}^{n} (x_j - \lfloor x_j \rfloor).$$

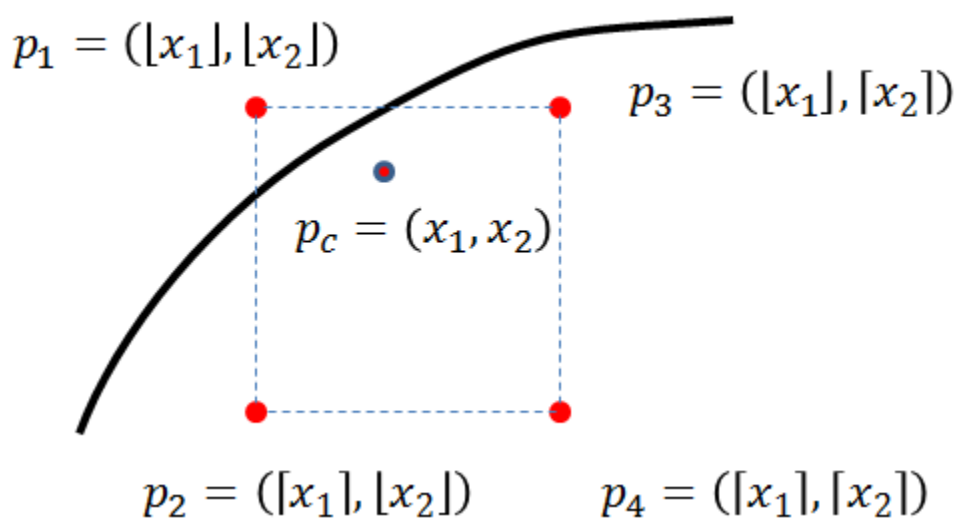

Figure 27 2-D illustration of tensor scale based *n*-linear interpolation algorithm. Conventional linear interpolation calculates the intensity at p_c based on linear distance weight so that p_1 will be assigned with the greatest weight value. From the observation, such weight leads to cross region mixing. By incorporating tensor scale, weight for p_2 and p_4 will be encouraged and smoother structure boundary will be generated.

The basic idea of using tensor scale in linear interpolation as illustrated in Figure 27 is to bring the notion of an anisotropic space where distance increases slower along the direction of the local structure while it decreases slowly across it. A smaller value of $\zeta_{p_i}(p_c)$ indicates that the vertex p_i is close to the partitioning manifold along the vector $\mathbf{i}_{p_i p_c}$ and therefore, the weight of p_i in interpolating the intensity value at p_c should be

discouraged to avoid cross-region mixing. On the other hand, a larger value of $\zeta_{p_j}(p_c)$ means that p_j is relatively far from the partitioning manifold along the vector $\mathbf{i}_{p_j p_c}$ and therefore a generous value of weight for p_j may be used along-the-edge smoothing. Therefore, the tensor scale based weights for linear interpolation are defined as follows:

$$w_i' = w_i \zeta_{p_i}(p_c).$$

Finally, the tensor scale based linear interpolation procedure is defined by the following equation:

$$f(p_c) = \frac{\sum_{i=1}^{2^n} w_i' f(p_i)}{\sum_{i=1}^{2^n} w_i'}.$$

5.3 Experimental Methods and Results

The performance of the tensor scale based n-linear image interpolation method was evaluated using a phantom image and several medical images from different applications and was compared with standard n-linear and windowed Sinc interpolation methods [123]. A 3-D phantom image of size $512 \times 512 \times 512$ was generated a sinusoidal wavy (along the slice direction) pattern of geometric structures with its scales varying from 5 to 10 voxels. Also, the following sets of medical images were used in our experiment: 1) The BrainWeb MR phantom data; 2) Seven human pulmonary multi-Detector CT images with voxel size of $0.55 \times 0.55 \times 0.5$ mm^3 and in-plane matrix grid size of 512×512 with the number of slices varying between 519 to 728; 3)Micro-CT images of four cadaveric distal tibia specimens at 28.8 μm isotropic resolution and 3-D image grid size of $768 \times 768 \times 512$; 4) Five abdominal CT with voxel size of $0.59 \times 0.59 \times 1.00$ mm^{3}and in-plane matrix grid size of 512×512 with the number of slices varying between 64 to 319. From each 3-D medical image, fifty VOIs, each of size $50 \times 50 \times 50$ voxels, will be randomly selected inside a lung/bone/abdomen region giving a total of 250 VOIs. For the phantom image, a total of 200 VOIs of the same will be randomly selected over regions containing geometric structures.

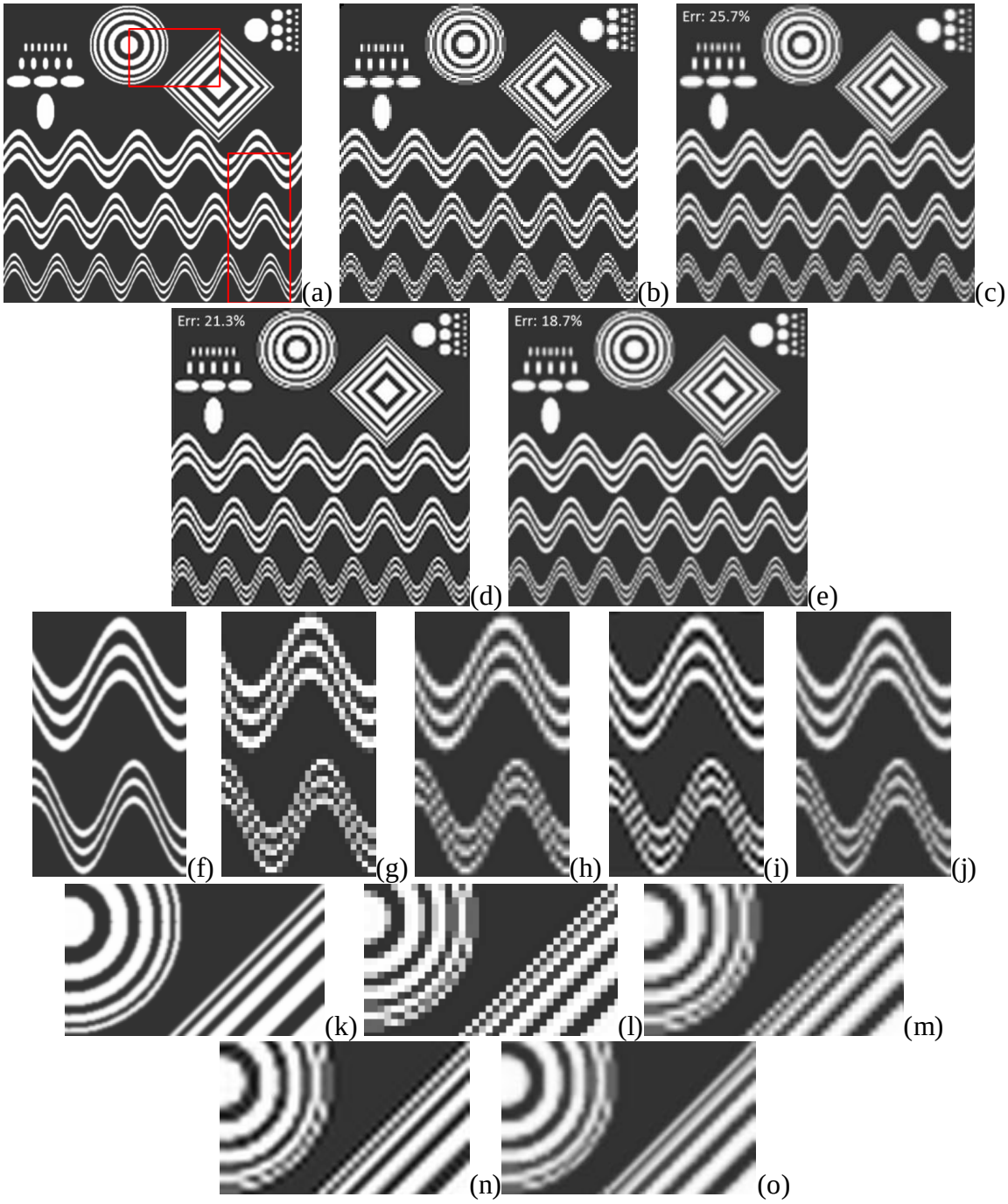

Figure 28 Results of image interpolation on a phantom data. (a) An original image slice. (b) Sub-sampled image at the rate 4. (c-e) Result using standard *n*-linear (c), windowed Sinc (d) and tensor scale based *n*-linear image interpolation. (f-j) Same as (a-e) but for a zoomed part marked in (a). (k-o) Same as (a-e) but for another zoomed region. It may be observed that tensor scale helps preserving small structures and it produces smooth edges without causing ringing artifacts which is visible for result produced by the windowed Sinc method.

Figure 28 show the results of applications of the three interpolation methods on the 3-D phantom image after 4×4×4 down sampling. Improvement in interpolations results using tensor scale based interpolation in terms of structure smoothness is visually apparent.

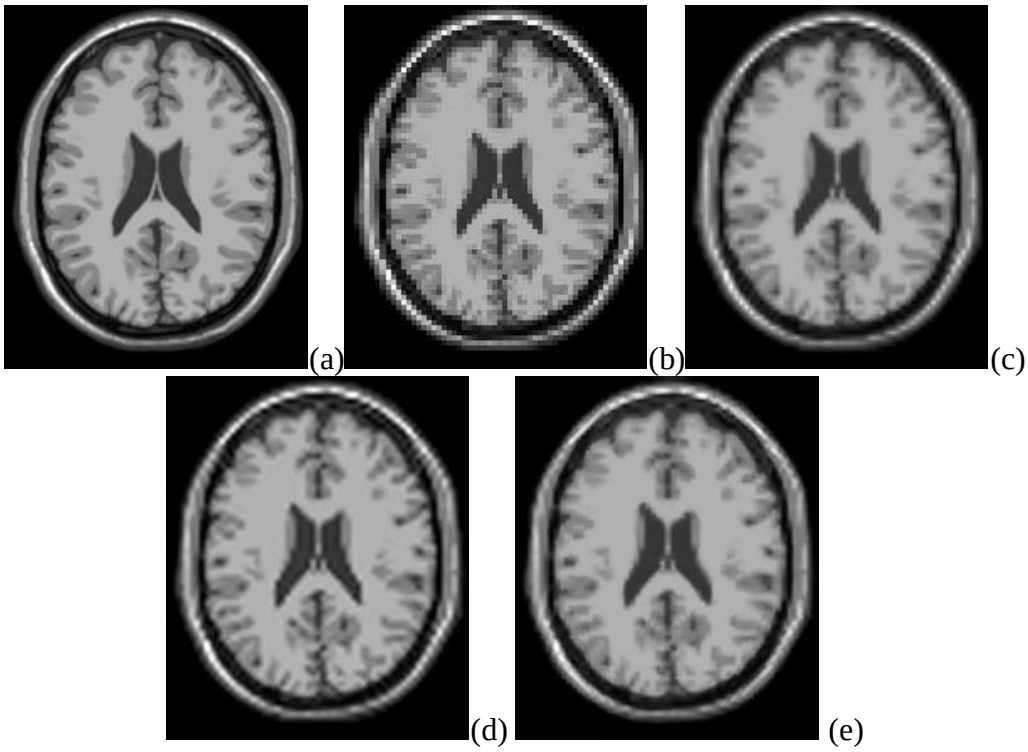

Figure 29 Results of image interpolation on the BrainWeb MR phantom image. (a) An original image slice. (b)An image slice from sub-sampled image at the rate of 3. (c-e) Results using standard *n*-linear (c), windowed Sinc (d) and tensor scale based *n*-linear (e) interpolation methods. It may be observed that tensor scale has produced crisper edges as compared to the standard *n*-linear interpolation without causing ringing artifact associated with the windowed Sinc method.

The results of application of the three interpolation methods on the BrainWeb MR phantom data after 4×4×4 down sampling is shown in Figure 29. It appears in the results the tensor scale based method reduces the blur along object boundaries and also the

ringing effects of windowed sync algorithm is absent in the tensor scale based interpolation results (Figure 29(e)). It may be mentioned that, for all interpolation experiments, tensor scale was computed from the sub-sampled images.

For quantitative analyses, starting from an original image I, a sub-sampled images I_r was obtained with different sub-sample rates of r = 2, 3 or 4. Let $I_{r,\text{method}}$ be the interpolated image at the original resolution obtained by applying a given method on the subsampled image I_r. The performance of the underlying interpolation method is then measured by computing the average normalized absolute difference between the interpolation and the original image for every VOI in a given image. For the ith VOI Ω_i it is computed as:

$$error_{i,r,\text{method}} = \frac{\sum_{p\in\Omega}\left|I_{\text{original}}(p) - I_{r,\text{method}}(p)\right|}{\sum_{p\in\Omega} I_{\text{original}}(p)}.$$

Finally, the interpolation error over the entire image at a given resample rate r, denoted by $MAD_{r,\text{method}}$, is computed as:

$$error_{r,\text{method}} = \frac{1}{K}\sum_{i=1}^{K} error_{i,r,\text{method}}$$

where K is the number of the image VOIs.

The three methods were compared under 2×2×2, 3×3×3, and 4×4×4 down sampling rates and the results are presented in Figure 30, Figure 31 and Figure 32. The tensor scale based interpolation method has improved the interpolation results for datasets at every down sampling rates and the enhancements are statistically significant except for a few cases as indicated in the figures. As compared to windowed Sinc algorithm, the tensor scale based method has improved the interpolation results except for the ankle dataset at 2×2×2 down sampling. However, for the lung and abdomen datasets, the windowed Sinc interpolation method has performed even worse than basic *n*-linear method.

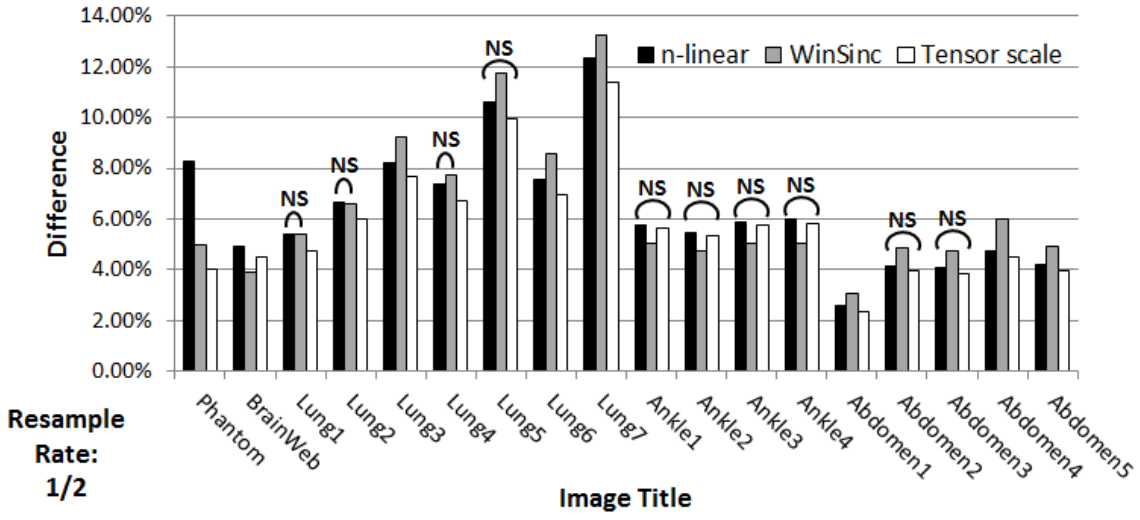

Figure 30 Performance of three interpolation methods on the different phantom and medical images selected from various clinical applications at sub-sampling rate of $2 \times 2 \times 2$. The percentage error was computed over the entire 3-D image while a paired t-test was performed based on the percentage error from individual slices. As compared with the standard *n*-linear and windowed Sinc methods, the tensor scale based *n*-linear method has outperformed the first method while comparative performance with the windowed Sinc method varies for different images. An "NS" (non-significant) mark is used to indicate statistical insignificance of difference in results by two methods.

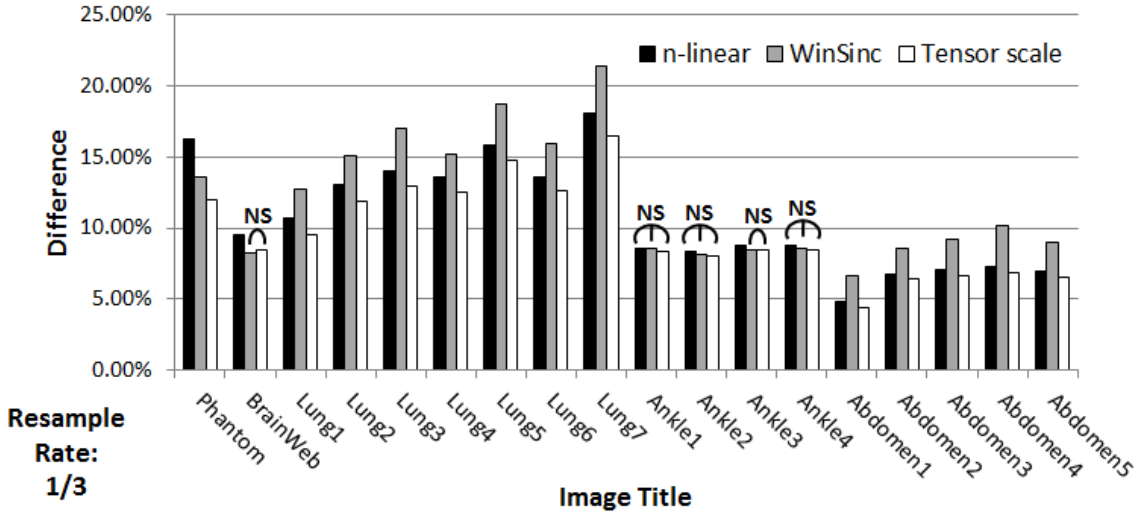

Figure 31 Same as Figure 30 but for subsample rate of $3 \times 3 \times 3$.

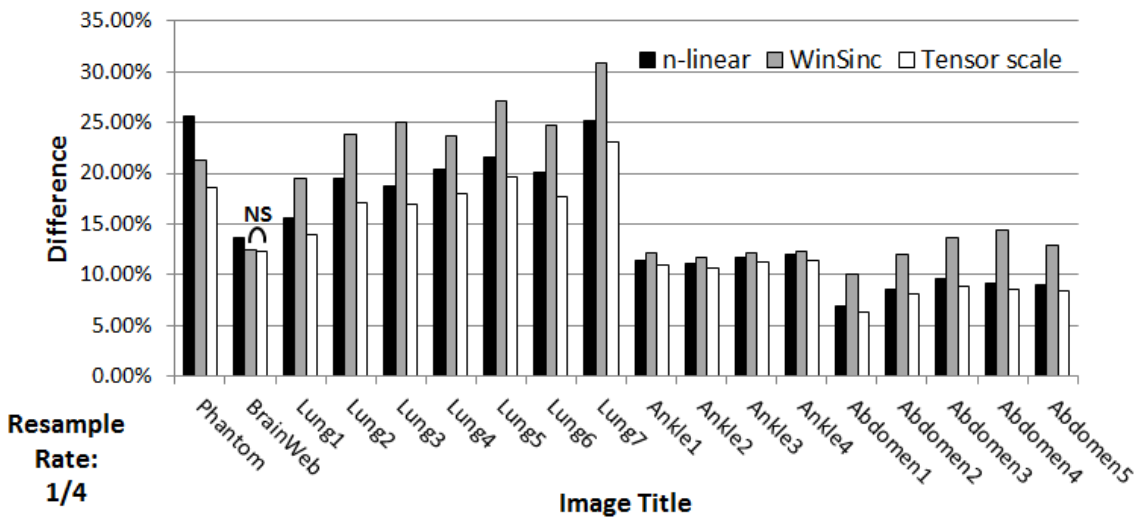

Figure 32 Same as Figure 30 but for subsample rate of $4 \times 4 \times 4$.

It general, it may be observed that, as sample rate gets lower, tensor scale extends its improvement in results as compared to basic *n*-linear interpolation while the results using the windowed Sinc methods get worse. This observation may be explained by the fact that, the use of structure information in the tensor scale method leads to a local context adaptive metric space partially healing for the subsampling loss. On the other hand, for windowed Sinc method, inclusion of a larger neighborhood may not add further meaningful information and may even worsen the results due to influence by locally disconnected structures falling inside the extended neighborhood leading to increase of ringing artifacts.

5.4 Conclusion

In this chapter, we investigated an application of tensor scale to *n*-linear image interpolation. Tensor scale brings the notion of an anisotropic space where distance increases slower along the direction of the local structure while it decreases slowly across it. The performance of tensor scale based *n*-linear interpolation method has been

compared with *n*-linear and windowed Sinc algorithms and both qualitative and quantitative results have demonstrated improvements using tensor scale.

CHAPTER 6

TENSOR SCALE BASED ANISOTROPIC REGION GROWING

6.1 Introduction

In this chapter, we present a new anisotropic region growing segmentation approach for vascular or other elongated structures. A fundamental challenge during tracing vascular structures is broken continuity of structures by noise and other imaging artifacts coupled with leaking through blurring and soft boundaries. Anisotropic region growing solves this problem using tensor scale that captures local structure orientation and geometry using an ellipsoidal model. A new fuzzy connectedness based algorithm is developed that uses tensor scale to facilitate region growing along the local structure while arresting cross-structure leaking. The performance of the method has been quantitatively evaluated on non-contrast human pulmonary CT imaging and the results found are promising.

In the following, detailed algorithm for fuzzy connectedness will be presented first. Subsequently, we introduce the theory and algorithm of a new anisotropic region growing algorithm that combine tensor scale with fuzzy connectedness method to facilitate along-structure growing while constraining cross-structure leaking, as well as techniques for automatic seed generation and vessel enhancement. Finally, experimental plans and methods are described, and results with concluding remarks are given.

6.2 Tensor Scale Based Anisotropic Region Growing

Over decades, segmentation has remained a salient task in most medical imaging applications confronting multi-faced challenges including limited image quality. Several segmentation approaches, including manual outlining, boundary based [88], regio*n*-based [90], and shape and model-based [91] techniques have been introduced and subsequently modified and investigated in different applications. In this application, we develop a new anisotropic region growing algorithm to segment elongated structures. Analysis of

vascular geometry is important in many medical imaging research including pulmonary, cardiac and carotid applications. The most significant challenges for this purpose are 1) high inter-subject variations of vascular shape even for a specific body region, 2) difficulty in generating a general vascular shape model and 3) high complexity of vascular geometry and topology, especially in the presence of fusions among artery, vein, and airway for pulmonary images. Shape or model based method is not well applicable due to the first two challenges and boundary based approach for pulmonary vessel segmentation is discouraged by the third challenge. Therefore, we have adopted region growing method that starts with a set of seeds specified inside a target object and continues growing the object region under a predefined set of rules. Among other region growing approaches [15, 16], fuzzy connectedness [18-20, 98] has become quite popular method where the region growing process is governed by a predefined fuzzy affinity relation.

6.2.1 Fuzzy connectedness Based Region Growing

As illustrated in Figure 33, fuzzy connectedness defines the strength of connectivity between any two points p, q in an image using a symmetric and reflexive 2-ary fuzzy relation referred to as "affinity". *Affinity* between any two points p, q, denoted as $\mu_\kappa(p, q)$, indicates the "hanging-togetherness" between the two points in a target object. More precisely, $\mu_\kappa(p, q)$ is the strength of the link $\langle p, q\rangle$ and its value lie in the interval $[0,1]$. Under a given fuzzy affinity relation κ, *the strength of a path* $\pi = \langle p = p_1, p_2, \cdots, p_l = q\rangle$, denoted as $\mu_{\mathcal{N}}(\pi)$ is defined as the strength of the weakest link on the path, i.e.,

$$\mu_{\mathcal{N}}(\pi) = \min_{1 \le i < l} \mu_\kappa(p_i, p_{i+1}).$$

There are infinitely many paths between two points p, q and let $\mathcal{P}(p, q)$ denote the set of all paths from p to q. The fuzzy connectedness between p, q, denoted as $\mu_K(p, q)$, is defined as the strength of the strongest among all paths in $\mathcal{P}(p, q)$, i.e.

$$\mu_K(p,q) = \max_{\pi \in \mathcal{P}(p,q)} \mu_{\mathcal{N}}(\pi).$$

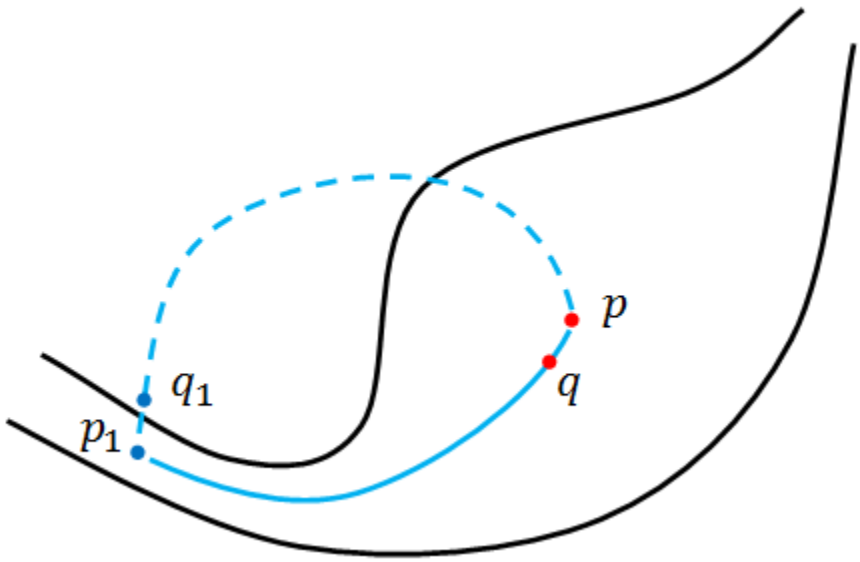

Figure 33 Illustration of fuzzy connectedness computation between two points p and p_1. For affinity, points belongs to the same structure have greater value than points of different structures, which means $\mu_\kappa(p,q) > \mu_\kappa(p_1,q_1)$. There are two paths, solid and dashed shown in the figure, based on the definition of the path strength, $\mu_{\mathcal{N}}(\pi_{\text{solid}}) > \mu_{\mathcal{N}}(\pi_{\text{dashed}})$. Finally, the fuzzy connectedness between p and p_1 is defined as the strength of the strongest path.

Finally, for given set S of seed points, the *fuzzy object* is defined as a fuzzy set $\mathcal{O}$ where the membership values at any point p indicates the maximum strength of fuzzy connectedness to any seed point in S, i.e.,

$$\mu_{\mathcal{O}}(p) = \max_{s \in S} \mu_K(p,s).$$

It has been shown in [98], that fuzzy connectedness is a similitude fuzzy relation and an efficient computational solution was presented in [20].

Effectiveness of fuzzy connectedness is highly dependent on the choice of the affinity relation. A major challenge with application of fuzzy connectedness in pulmonary vessel segmentation emerges from the fact that vessels, the target object in the current application, form a tree-like structure of tubular paths and at fine scales, the diameter of these paths may be comparable to voxel resolution. Therefore, these tubular paths, especially at finer scales, are vulnerable and getting broken by noise and other imaging artifacts and the continuity of vascular structure may get lost using a region growing rules suitable for other regions. On the other hand, softening the rules to capture the broken continuity may cause to leaking at other regions. However, a human expert may capture the broken continuity implicitly using the contextual local structures.

6.2.2 Tensor Scale Based Anisotropic Fuzzy Region Growing

With tensor scale, we develop a constrained region growing algorithm where the growing rules adapt to local structure geometry facilitating growth along a structure while constraining it across local structures.

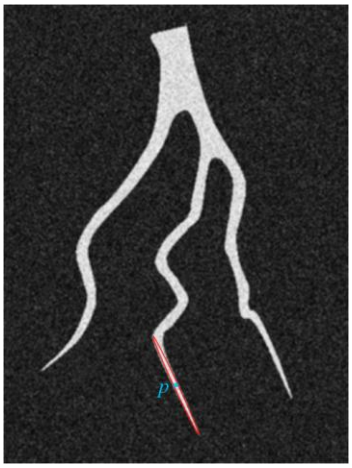

Figure 34 A schematic representation of a vascular tree structure in 2-D. Tensor scale at a point p is indicated by the ellipse in red. The proposed constrained region growing algorithm uses this knowledge to facilitate growth along the structure while restricting growth across the local structure to stop leaking.

For example, consider the example of Figure 34; using the tensor scale at the point p, we know the orientation and geometry of local structures at p. The proposed constrained region growing algorithm uses this knowledge to facilitate growth along the structure while restricting growth across the local structure to stop leaking. In the following paragraph, we formally describe the theory and algorithms.

As described above, the effectiveness of fuzzy connectedness largely depend on the choice of the affinity function μ_κ. A detailed discussion of formulation of affinity function may be found in [10]. However, there is not mention on how to use structure anisotropy and orientation informally to locally adopt the affinity in a direction-dependent fashion. Here, we formulate a local tensor scale defined affinity function to simulate a constrained region growing that facilitates the growth of an object along local structure direction while constraining it across local structure. Following the suggestion of [10], we use the basic underlying formulation of the affinity function:

$$\mu_\kappa(p,q) = \begin{cases} 1, & \text{if } p = q, \\ \mu_\alpha(p,q)\sqrt{\mu_\psi(p,q)\mu_\phi(p,q)}, & \text{otherwise.} \end{cases}$$

where $\mu_\alpha : \mathbb{Z}^3 \times \mathbb{Z}^3 \to \{0,1\}$ is the adjacency function while $\mu_\psi(p,q)$ captures homogeneity between p and q and $\mu_\phi(p,q)$ gives the hanging-togetherness of p, q in the target object based on likeliness of their feature values with respect to the expected feature distribution of the target object. It was also argued in [10] that the function μ_ψ should be chosen to reflect the measure of the fuzzy proposition "x is small" [124] while the other function μ_ϕ should be chosen to reflect the measure of the fuzzy proposition "x is close to an expected value" [124]. In our research work we have used the following functional forms for μ_ψ and μ_ϕ satisfying these properties:

$$\mu_\psi(p,q) = e^{-\frac{|f(p)-f(q)|^2}{2\sigma_\psi^2}}, \quad \text{and} \quad \mu_\phi(p,q) = \min\left(e^{-\frac{|f(p)-m|^2}{2\sigma_\phi^2}}, e^{-\frac{|f(q)-m|^2}{2\sigma_\phi^2}}\right)$$

where σ_ψ and σ_ϕ are two different standard deviation parameters used for homogeneity and object feature distribution and m is the mean object feature value. Although, this formulation immediately extends to vector-valued images, here, we consider only scalar-valued images depending on our application. The key idea of our constrained region growing is to locally adapt the two parameters σ_ψ and σ_ϕ in a direction dependent manner using local tensor scale to enhance growth compliance with local structures.

The control parameters σ_ψ and σ_ϕ determine the growth process for an object. When these parameters are large, the object grows more vigorously and possibilities of leaking through object boundaries increase. On the other hand, when small values are used for these parameters, the growth process works conservatively and the chance of breaking object continuity due to noise and other imaging artifacts increases. In the conventional region growing methods [15, 16], these parameters was kept fixed and fine control on and adaptivity to local structural properties were lacking. These regional control and adaptivity are provided by local scale. The motivation of using tensor scale in region growing is to introduce the local control and adaptivity in an orientation-dependent fashion as illustrated in Figure 34.

Specifically, the two controlling parameter σ_ψ and σ_ϕ are determined by local tensor scale in a space- and orientation-variant manner as follows:

$$\sigma_X(p,q) = \sigma_{X,\text{stationary}} + \chi\left(\max\left(\zeta_p(q), \zeta_q(p)\right)\right)\sigma_{X,\text{adaptive}},$$

where $X \in \{\psi, \phi\}$, $\zeta_p(q)$ is the radius of the tensor scale ellipsoid at p along pq. χ is a monotonically non-decreasing function, e.g.,

$$\chi(x) = \begin{cases} 1, & \text{if } x > x_{\max} \\ \dfrac{1+x}{1+x_{\max}} & \text{otherwise.} \end{cases}$$

The value of $x_{\max}$ is determined as the rough estimate of the maximum scale of the target object. The two parameters $\sigma_{X,\text{stationary}}$ and $\sigma_{X,\text{adaptive}}$ are the stationary and adaptive components in the control parameter; here, we have used one third of the total

control parameter remain stationary while the two-third fraction is varied by local tensor scale; thus, the ratio of $\sigma_{X,\text{stationary}}$ and $\sigma_{X,\text{adaptive}}$ 1:2. Finally, the total value of the control parameter, i.e., $\sigma_{X,\text{stationary}} + \sigma_{X,\text{adaptive}}$is determined following the description in [9]

6.2.3 Vessel Enhancement and Automatic Seeding

For the specific task of pulmonary vessel tree segmentation, a common challenge for region growing techniques is leaking to adjacent anatomical structures including lung parenchyma, fissure, and airway wall. To reduce the influence of these structures, a multi-scale convolutional vessel enhancement algorithm based on eigenvalues of Hessian matrix [125, 126] is first employed to highlight the vessel structures that can be modeled as cylindrical shape. A common procedure for the method is that, firstly, the candidate image is convolved with 3-D Gaussian filters at multiple scales, yielding response for vessels of different radiuses; then the eigenvalues of the Hessian matrix computed at each voxel are analyzed. The eigenvalues are related to structure geometry and are therefore used to indicate the shape of underlying object.

For 3-D lung CT images under investigation here, all three eigenvalues with similar positive values infer isotropic structures such as parenchyma while for tubular vessel structures, the eigenvalues hold a different pattern. For a multi-scale analysis, given that the method will yield maximum response at a scale that approximately matches the size of vessels, the final vesselness measurement is chosen as the maximum value under different scales and with this procedure, the radius is approximated with the scale parameter used for achieving the maximum. An example is given in Figure 35 where we reduced undesired structures such as fissure (as shown within rectangles) and airway wall (as shown within circle) by enhancing the tubular vessel structures.

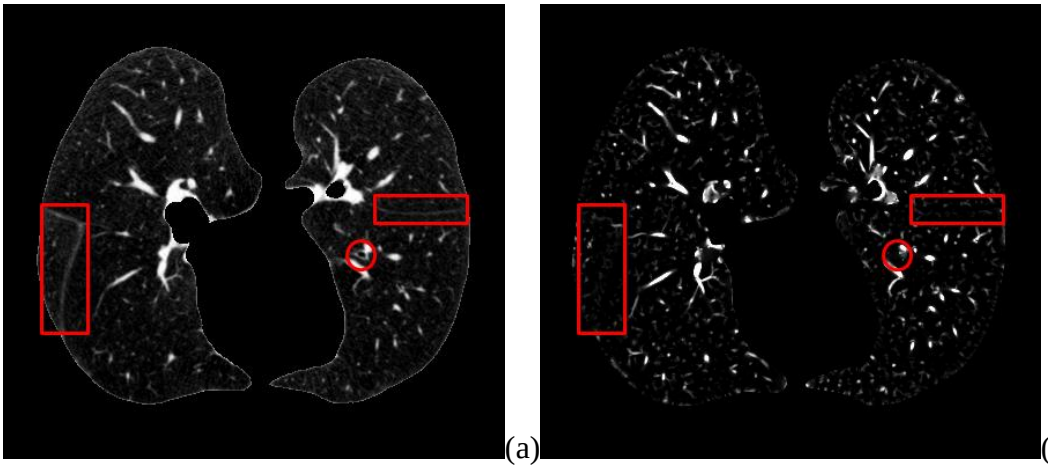

Figure 35 An example of vessel enhancement result in (b) for a pulmonary image (a). It can be observed that we reduce undesired structures such as fissure (as shown within rectangles) and airway wall (as shown within circle) by enhancing the tubular vessel structures.

One important input for fuzzy connectedness based image segmentation method is a set of seed points. Therefore for designing an automatic segmentation algorithm, we need to identify reliable seed positions within the lung vessels. Here, we have combined intensity information, radius estimation and tensor scale based centerline approximation to identify seed points within a CT image. Firstly, a conservative threshold of intensity in Hounsfield Unit is decided to create an initial decision on seed points with a high specificity. Then, seed points closer to centerlines of vessels are selected. This task is accomplished based on analysis of the primary t-vector with observation that the magnitude of primary vector yields local maxima at centerline points. Finally, seed points are further selected based on the radius estimate given by multi-scale filtering. An example of seed point selection is provided in Figure 36. As shown in the figure, seed points are selected approximately along the centerline of vessel structures. Finally, with the set of seed points selected within the whole lung image, the segmentation method described in Chapter 6.2.2 is performed.

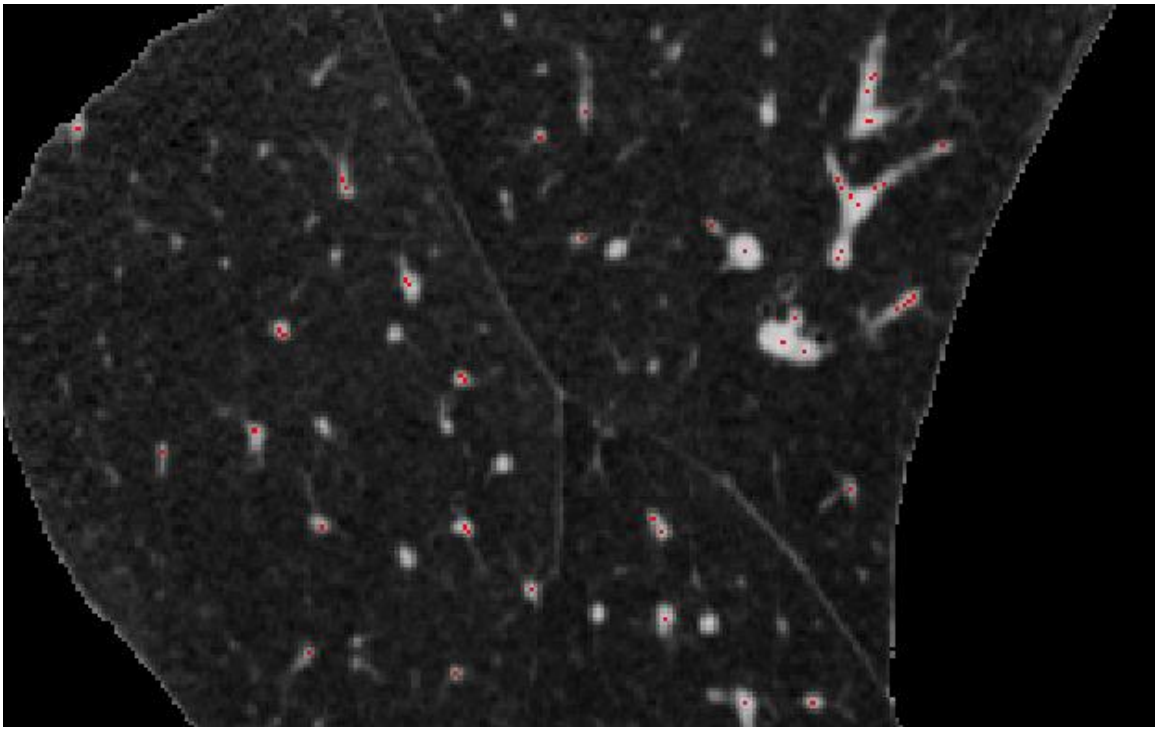

Figure 36 Seed points selected on part of an illustration slice. Seed points (red) locate approximately on the centerline of lung vessels.

6.3 Experimental Methods and Results

Tensor scale based anisotropic region growing method was applied on 2-D image and several 3-D medical images and was compared with both conventional fuzzy region growing algorithm without tensor scale and vesselness based method. For qualitative observation, we first present the results on a 2-D photographic image of a coral reef containing a complex tree-like network of locally elongated fuzzy branch structures. Then, we evaluate our method on four pulmonary CT images. To quantitatively evaluate the performance of our algorithm, we used manually selected points inside and out vascular regions those were used as ground truth for accuracy and error evaluation. Specifically, 1000 points were manually selected by an expert inside the vascular region on randomly picked slices; another set of 1000 points were selected outside the vascular region. Visually confirmed vessels over the entire range of scales were used to select

these points; finally, the points outside the vessels were selected in common leakage regions such as lung parenchyma, fissure, and airway wall as well we near-vessel regions with no further than 3 voxels from the vessel as determined visually. Let V denote the set of points manually selected on vascular region and let B denotes the set of points manually selected outside the vascular region. Let V_{method} and B_{method} denote the set of points on vascular region on its complement derived by applying a given method. The following measures are defined to examine the performance of a given method.

$$True\ Positive_{\text{method}} = \frac{|V \cap V_{\text{method}}|}{|V|}$$

$$True\ Negative_{\text{method}} = \frac{|B \cap B_{\text{method}}|}{|B|}$$

$$False\ Positive_{\text{method}} = \frac{|B \cap V_{\text{method}}|}{|B|}$$

$$True\ Negative_{\text{method}} = \frac{|V \cap B_{\text{method}}|}{|V|}$$

$$Accuracy_{\text{method}} = \frac{|V \cap V_{\text{method}}| + |B \cap B_{\text{method}}|}{|V| + |B|}$$

$$Error_{\text{method}} = \frac{|V \cap B_{\text{method}}| + |B \cap V_{\text{method}}|}{|V| + |B|}$$

Results of several qualitative and quantitative evaluative experiments are presented. Figure 37 presents the results of application of the new method and its comparison with the conventional fuzzy connectedness region growing [20] on a 2-D photographic image of a coral reef containing a complex tree-like network of locally elongated fuzzy branch structures. As shown Figure 37 (a), one seed (red dot) was manually selected on the main trunk of the coral reef tree and the results of application using the conventional and the anisotropic region growing methods are shown in Figure 37 (b,c), respectively.

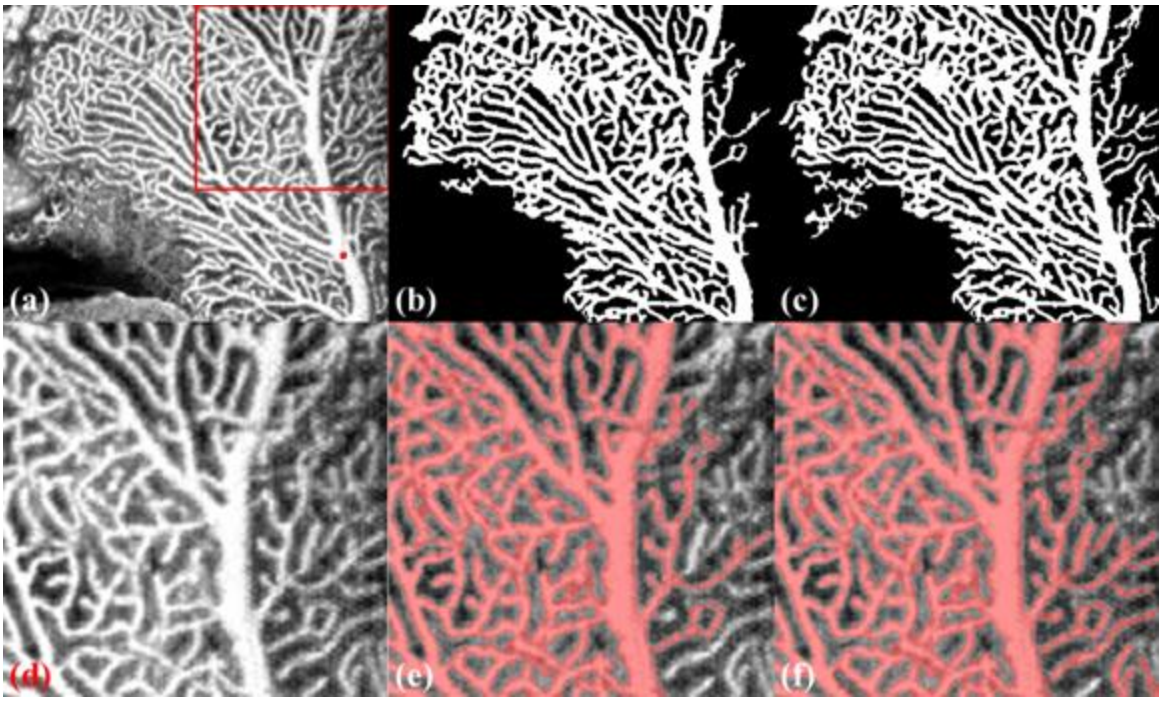

Figure 37 2-D Segmentation results on an image of coral reef (a); the red dot indicates the seed. The new anisotropic region growing has captured more branches (c) as compared to the conventional algorithm (b). (d-f) Zoomed-in display of (a-c) over the regions marked by the red box in (a).

As observed in Figure 37 (b,c), the new method (Figure 37 (c)) captures more branch structures, especially at low-contrast regions where the vessel got broken by imaging artifacts and noise and it is more prominent in the zoomed in displays of Figure 37(d-f).

Figure 38 shows a comparison result for a pulmonary CT image between fuzzy connectedness segmentation method without and with tensor scale information. As shown in the image, tensor scale successfully helped the algorithm to capture more vessel structures that were missed without tensor scale.

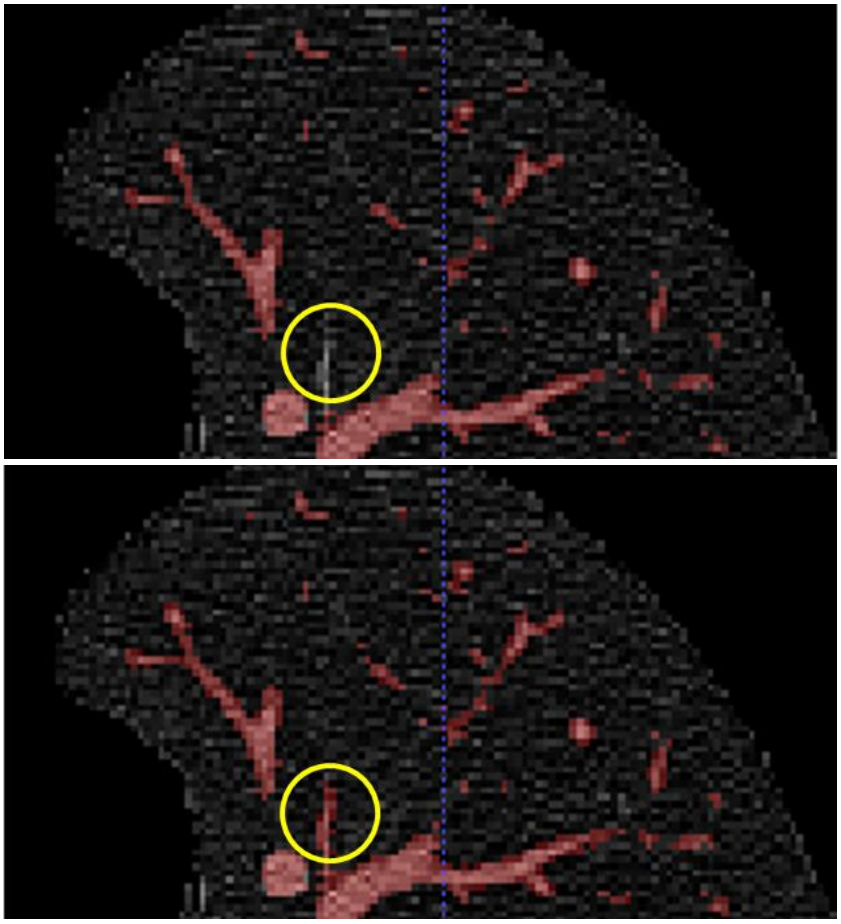

Figure 38 One slice in 3-D Segmentation for pulmonary CT image; as shown within the circle, one branch missed by fuzzy connectedness segmentation method without tensor scale (a) is captured by incorporating tensor scale information (b).

Four non-contrast pulmonary human CT images acquired with voxel size of $0.55 \times 0.55 \times 0.5\ \mathrm{mm}^3$ and in-plane matrix of 512×512 was used to quantitatively evaluate the new method's performance in comparison with Shikata's method [127]. Seed points are automatically generated in the vessel region for applying the new anisotropic diffusion algorithm for vascular segmentation. Initial results of anisotropic region growing are shown in Figure 39(b). The new method has successfully captured structures at a wide range of scales including those at high and small scales. Pulmonary vessel was separated from cardiac and other tissue regions by putting a separator on

pulmonary trunk and separating the pulmonary vasculature from the rest of the tissue using the multi-scale opening algorithm [128]. Results of pulmonary vasculature by region growing without and with tensor scale are shown in Figure 39 (d) and (e). Results of vascular segmentation using Shikata's method are shown in Figure 39 (a) and (c).

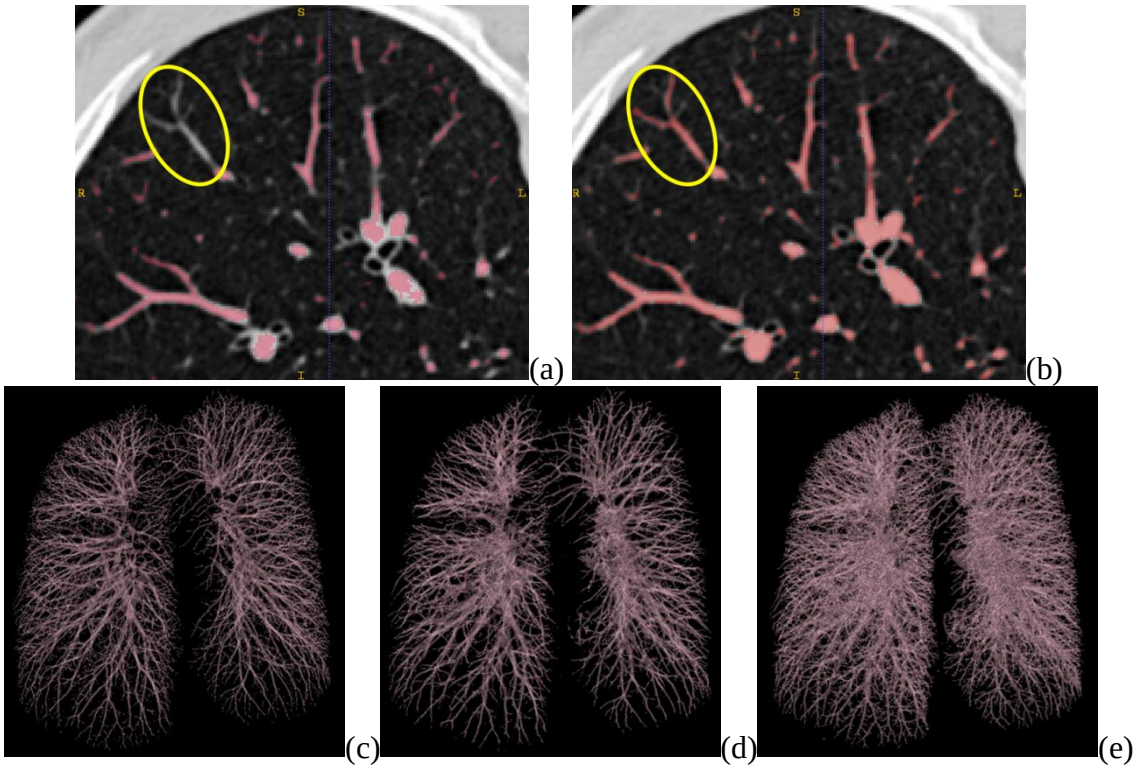

Figure 39 Results of vascular segmentation in non-contrast human pulmonary CT imaging. (a) A 2-D CT image slice with overlapped vessel segmentation result using Shikata's method. (b) Matching slice with overlapped vessel segmentation result using tensor scale (c-e) 3-D renditions of vasculature using Shikata's (c), conventional region growing (d) and the tensor scale (e) methods.

Although, the method by Shikata was able to capture medium scale vessels, its performance was somewhat compromised at fine and large scale.

3-D rendition of vasculature using our method and Shikata's method are presented in Figure 39 (c-e), respectively, confirming our observations in 2-D. Vessel segmentation results using anisotropic region growing algorithm capture more details at large and small scales and also maintain better vascular topology around the pulmonary entry region as compared to Shikata's method due to the compromised behavior of the later method at large scales.

Table 6 Results of accuracy analyses of vessel segmentation by the two methods.

	Data set 1			*Data set 2*		
	Shikata	Fuzzy w/o tensor scale	Fuzzy w/ tensor scale	Shikata	Fuzzy w/o tensor scale	Fuzzy w/ tensor scale
True Positive	0.840	0.874	0.979	0.619	0.851	0.973
True Negative	0.999	0.994	0.973	0.994	0.988	0.964
False Positive	0.001	0.006	0.027	0.006	0.012	0.036
False Negative	0.160	0.126	0.021	0.381	0.149	0.027
Accuracy	0.915	0.931	0.976	0.789	0.913	0.969
Error	0.085	0.069	0.024	0.211	0.087	0.031
	Data set 3			*Data set 4*		
	Shikata	Fuzzy w/o tensor scale	Fuzzy w/ tensor scale	Shikata	Fuzzy w/o tensor scale	Fuzzy w/ tensor scale
True Positive	0.809	0.870	0.975	0.735	0.859	0.963
True Negative	0.998	0.990	0.968	0.992	0.987	0.959
False Positive	0.002	0.010	0.032	0.008	0.013	0.041
False Negative	0.191	0.130	0.025	0.265	0.141	0.037
Accuracy	0.904	0.930	0.972	0.864	0.923	0.961
Error	0.096	0.070	0.028	0.136	0.077	0.039

Performance measures for the two methods as well as the performance of fuzzy region growing without tensor scale information on four different datasets are presented in Table 6. The accuracy is quite high for all data sets. The True Positive and True Negative here are defined as the accuracy for detection of vascular region and background, which turn to be values close to 1. The False Positive is the percent of voxels outside vascular region are falsely detected vessel, which is a small value for both data sets. The False Negative is the percent of voxels inside vascular region are falsely detected as non-vessel, which is a small value for both data sets. The new method has produced high accuracy for all datasets while the method without tensor scale and Shikata's method produced significantly lower accuracy for the second dataset which was caused by missing an entire vascular branch due to its compromised performance at large scales. It may be pointed out that, following our definition, the sum of accuracy and error measures is always '1' here.

6.4 Conclusion

In this chapter, we investigated an application of tensor scale to fuzzy connectedness based anisotropic region growing algorithm. The method combines tensor scale with fuzzy connectedness facilitating region growth along local structures while arresting cross-structure leaking. By incorporating tensor scale information, the algorithm locally adapts and governs the fuzzy segmentation process so that it can capture vascular structures more robustly in the presence of noise and other imaging artifacts. Application of the method to pulmonary images with multi-scale vessel enhancement and automatic seed generation demonstrates promising quantitative results.

CHAPTER 7

CONCLUSION AND FUTURE DIRECTIONS

7.1 Conclusion

Tensor scale is a local morphometric parameter using an ellipsoidal model that yields a unified representation of local structure size, orientation, and anisotropy. It captures local structural information and is widely applicable to multiple image processing and analysis tasks. The computation and application of tensor scale is challenging for 3-D images and the overall aim of the Ph.D. research project was to establish an analytic definition of tensor scale in *n*-D images, develop an efficient computational solution and investigate its role in various medical imaging applications including image interpolation, filtering and segmentation. The overall objective was structured in six specific aims as follows:

Aim 1: Establish an analytic approach to define tensor scale in *n*-D images with objects formed by pseudo-Riemannian partitioning manifolds.

Aim 2: Develop an efficient computational algorithm for 2- and 3-D images combining Euclidean distance transform and several novel differential geometric approaches. Perform experiments to evaluate the accuracy of the computational algorithm.

Aim 3: Design and develop an inter-slice interpolation algorithm based on tensor scale. Perform experiments to evaluate the performance of the method in comparison with to existing interpolation algorithms.

Aim 4: Design and develop an anisotropic diffusion filtering algorithm based on tensor scale. Perform experiments to evaluate the performance of tensor scale guided anisotropic diffusion filtering method in comparison with conventional gradient and structure tensor based diffusion filtering algorithms.

Aim 5: Design and develop a tensor scale based *n*-linear interpolation method. Perform experiments to evaluate the performance of tensor scale based interpolation

method in comparison with standard linear interpolation and windowed Sinc interpolation methods.

Aim 6: Design and develop a new anisotropic constrained region growing method locally controlled by tensor scale for vessel segmentation. Perform experiments to evaluate the accuracy of tensor scale guided region growing method for vasculature segmentation.

In Chapter 2, we presented an analytic formulation for tensor scale for *n*-D images together with an efficient computational solution in 2- and 3-D (Aim 1 and 2). The computational solution is based on several techniques including gray scale distance transform and computation of local principal curvature directions on the closest partitioning manifold represented by discrete edge points. Experimental results for both 2- and 3-D images were presented. Robustness and accuracy of the computation framework is examined in comparison with theoretical results derived under the ideal condition of object partitions with no noise and blur have demonstrated that the proposed efficient computation method yields acceptable results at moderate noise and blur with image structures being visually apparent.

In Chapter 3, we investigated the application of tensor scale to medical image slice interpolation (Aim 3). A closed form solution for computing interpolation lines using tensor scale has been introduced which has contributed to a new tensor scale based interpolation algorithm. Experimental results have demonstrated that the new interpolation method outperforms state-of-the-art registration based interpolation techniques on real clinical images and the statistical significance of the improvements was observed.

In Chapter 4, we applied tensor scale to anisotropic diffusion image filtering (Aim 4). Tensor scale generates an optimal scale parameter that fits with local image structures and we utilized this parameter to design a new conductance function governing the diffusion process in a space-variant and orientation dependent fashion. The performance

of tensor scale based filtering has been compared with that of gradient and structure tensor based diffusion filtering algorithms and both qualitative and quantitative results have demonstrated improvements in image filtering using tensor scale.

In Chapter 5, tensor scale based *n*-linear image interpolation algorithm is designed. Tensor scale brings the notion of an anisotropic space where distance increases slower along the direction of the local structure while it decreases slowly across it. Therefore, cross region mixing is avoided by incorporating tensor scale information to the method. The performance of tensor scale based *n*-linear interpolation method has been compared with conventional *n*-linear and windowed Sinc algorithms and both qualitative and quantitative results have demonstrated improvements using tensor scale.

In Chapter 6, we designed and developed a tensor scale based anisotropic fuzzy region growing algorithm. The method combines tensor scale with fuzzy connectedness facilitating region growth along local structures while arresting cross-structure leaking. By incorporating tensor scale information, the algorithm locally adapts and governs the fuzzy segmentation process so that it can capture vascular structures more robustly in the presence of noise and other imaging artifacts. Application of the method to pulmonary images with multi-scale vessel enhancement and automatic seed generation demonstrates promising quantitative results comparing with vesselness based method and fuzzy method without tensor scale.

7.2 Future Directions

The general tensor scale frameworks presented in this thesis have a number of potential applications and extensions that have been preliminarily investigated. Here, we discuss three interesting future directions in related areas.

7.2.1 Tensor Scale Based Features in Computer Vision Applications

In this thesis, we have shown mostly the use of tensor scale in locally control for various medical image processing tasks. Since tensor scale extracts rich structural

information for every point in an image, a natural idea is to derive features from tensor scale and apply them to computer vision and pattern recognition applications.

Feature extraction is an important step for computer vision and pattern recognition tasks. It generate a feature vector that is of lower dimension than original data while preserving useful information contained in the data for a specific job. Basic features are often computed on intensity and local operations such as gradient given by Gaussian convolution at different scales, histogram of local neighborhood, and detection of contour and corner points. Tensor scale provides structure information not only at salient points but also within homogenous regions and can therefore potentially serve in feature extraction.

A preliminary experiment has been performed on retinal image mosaicking where a mosaic image is generated by combining several fundus images with different field of view to the object in order to facilitate the diagnosis process. Mosaic synthesis generally contains multiple pairwise registration as shown in Figure 40 which combines two partially overlapped images to form a new image with larger field of view. Such process faces many problems such as different illumination during imaging, limited overlap region, radial distortion due to sphere nature of human eye, and limited vessel width.

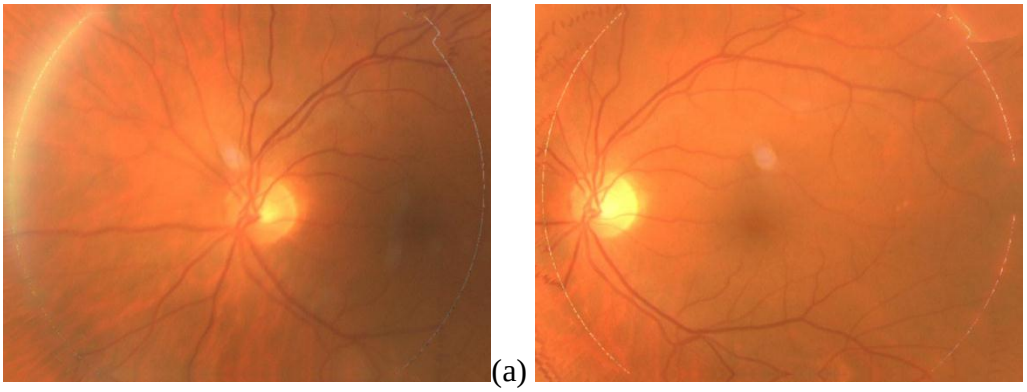

Figure 40 Two retinal fundus images with different field of view to a single object

Tensor scale is capable of extracting structure features that are consistent under image rotation, varying pixel size, and background inhomogeneity. Also, it is independent of local intensity change due to illumination or other artifacts. Therefore, it is useful in this application.

Several features including distance to edges, local structure size, anisotropy and orientation and convexity of distance map as illustrated in Figure 41.

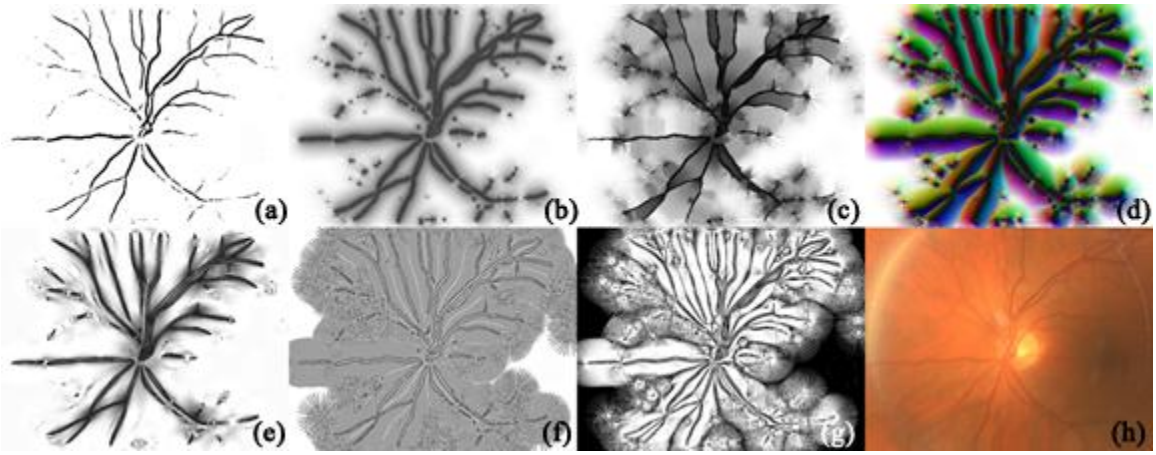

Figure 41 Features extracted from tensor scale from vessel map (a) of the original image (h): distance to edges (b), local structure size (c), local structure orientation (d), local anisotropy (e), center/edge point label (f) and convexity of distance map (g)

Based on these features, correspondences between points within two images are identified and a transformation is estimated for final mosaic result is shown in Figure 42. The performance of the preliminary experiment is limited by the simple transformation model and basic correspondence detection algorithm, while the potential of structural features derived from tensor scale is illustrated. In the future, it can be incorporated with more sophisticated methods such as salient point detection, advanced matching techniques and complex transformation models.

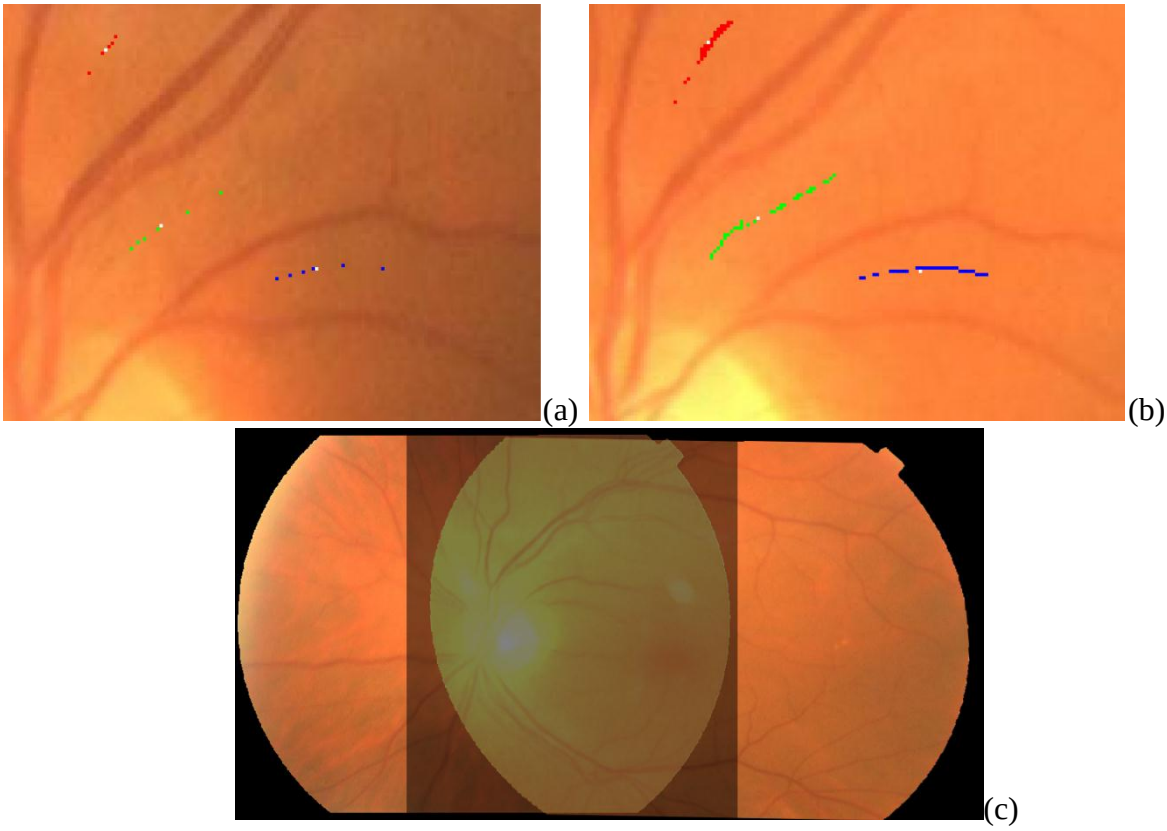

Figure 42 Correspondence between two images, a set of points are selected in (a) and their correspondent point is identified in (b). Correspondent points are then clustered for estimation of transformation between images and final result is shown in (c).

7.2.2 Tensor Scale Based Shape Analysis Algorithms

Tensor scale extracts useful information regarding shape of structures in the images. For medical image analysis tasks, orientation, scale and anisotropy features are often of significant value in estimating pose, size as well as approximate shape of the anatomical structures for more accurate recognition, segmentation and evaluation purposes.

For example, anisotropy and scale information provided by tensor scale can be used for assessment of plate and rod structures for CT trabecular bone images. A preliminary result is provided in Figure 43 where we evaluate the different structures

within the bone based on the scale and anisotropy information extracted by tensor scale. This work is currently under investigation in our lab.

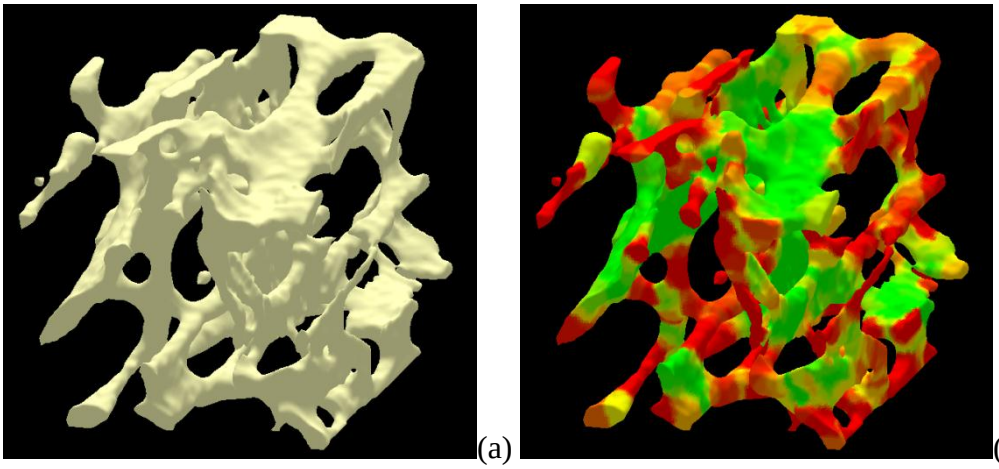

Figure 43 Tensor scale based shape analysis, a trabecular bone structure with rods and plates is shown in (a) and the structure evaluation result is provided in (b).

7.2.3 Tensor Scale Based Similarity Measurements for Image Registration

Image registration has played an important role in medical applications such as atlas based image segmentation, motion modeling, and multi-modality fusion. The fundamental assumption in these applications is that a correspondence mapping between anatomical structures can be identified by image registration. Specifically, for deformable registration method, the primary objective is to compute a deformation vector field that warps a target image onto a reference image. In other words, for each point in the target image, we need to determine its correspondence in the reference image.

Tensor scale is shown to be invariant with regard to rotation and scaling, and it is independent of background inhomogeneity with robust performance under different levels of noise. Also, it captures structural information that does not rely on specific

intensity value for certain anatomical structures. Therefore, it has the potential to be applied in designing similarity measurement for image registration.

A preliminary result is provided in Figure 44, where a geometric Y-like shape is registered onto a disk via an intermediate shape.

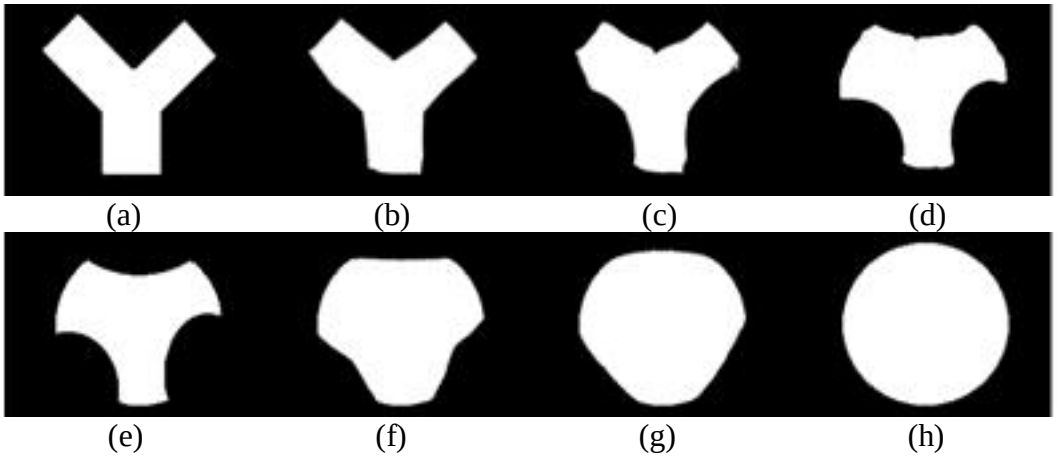

Figure 44 Illustrations of different shapes during deformation of a Y-like target shape (a) onto a disk (h) via an intermediate shape (e) using the tensor scale based method. Intermediate shapes during warping from (a) to (e) are shown in (b-d) while (f-g) illustrate intermediate shapes between (e) and (h).

The above result has illustrated the potential of tensor scale in image registration, while for further development there are two major challenges to be addressed. Firstly, we need to appropriately design the similarity measurement based on tensor scale information, since current tensor matrix based similarity is not efficient and accurate for registration purpose; and secondly, it is critical to find the solution for accurate estimation of the change in tensor scale due to the deformation during registration process so that optimization techniques can be applied to the proposed similarity measurement.

REFERENCES

[1] T. Lindeberg, *Scale-Space Theory in Computer Vision*. Boston, MA: Kluwer Academic Publishers, 1994.

[2] R. C. Gonzalez and R. E. Woods, *Digital Image Processing*. Reading, MA: Addison-Wesley, 1992.

[3] M. Sonka, V. Hlavac, and R. Boyle, *Image Processing, Analysis, and Machine Vision*, 3rd ed. Toronto, Canada: Thomson Engineering, 2007.

[4] M. Tabb and N. Ahuja, "Multiscale image segmentation by integrated edge and region detection," *IEEE Transactions on Image Processing,* vol. 6, pp. 642-655, 1997.

[5] S. M. Pizer, D. Eberly, and D. S. Fritsch, "Zoom-invariant vision of figural shape: the mathematics of core," *Computer Vision and Image Understanding,* vol. 69, pp. 55-71, 1998.

[6] J. H. Elder and S. W. Zucker, "Local scale control for edge detection and blur estimation," *IEEE Transactions on Pattern Analysis and Machine Intelligence,* vol. 20, pp. 699-716, 1998.

[7] P. Liang and Y. F. Wang, "Local scale controlled anisotropic diffusion with local noise estimate for image smoothing and edge detection," presented at the International Conference in Computer Vision, Bombay, India, 1998.

[8] P. K. Saha, J. K. Udupa, and D. Odhner, "Scale-based fuzzy connected image segmentation: theory, algorithms, and validation," *Computer Vision and Image Understanding,* vol. 77, pp. 145-174, 2000.

[9] P. K. Saha and J. K. Udupa, "Scale based image filtering preserving boundary sharpness and fine structures," *IEEE Transactions on Medical Imaging,* vol. 20, pp. 1140-1155, 2001.

[10] P. K. Saha, "Tensor scale: a local morphometric parameter with applications to computer vision and image processing," *Computer Vision and Image Understanding,* vol. 99, pp. 384-413, 2005.

[11] P. K. Saha and Z. Xu, "An Analytic Approach to Tensor Scale with an Efficient Algorithm and Applications to Image Filtering," in *Digital Image Computing: Techniques and Applications (DICTA), 2010 International Conference on*, 2010, pp. 429-434.

[12] V. Arsigny, P. Fillard, X. Pennec, and N. Ayache, "Log-euclidean metrics for fast and simple calculus on diffusion tensors," *Magnetic Resonance in Medicine,* vol. 56, pp. 411-421, Aug 2006.

[13] Z. Xu, M. Sonka, and P. K. Saha, "Improved tensor scale computation with application to medical image interpolation," *Computerized Medical Imaging and Graphics,* vol. 35, pp. 64-80, Jan 2011.

[14] P. Perona and J. Malik, "Scale-space and edge detection using anisotropic diffusion," *IEEE Transactions on Pattern Analysis and Machine Intelligence,* vol. 12, pp. 629-639, 1990.

[15] Y. L. Chang and X. Li, "Adaptive image region growing," *IEEE Transactions on Image Processing,* vol. 3, pp. 868-873, 1994.

[16] S. Chu and A. Yuille, "Region competition: unifying snakes, region growing and bayes/MDL for multiband image segmentation," *IEEE Transactions on Pattern Analysis and Machine Intelligence,* vol. 18, pp. 884-900, 1996.

[17] E. A. Hoffman, J. M. Reinhardt, M. Sonka, B. A. Simon, J. Guo, O. Saba, D. Chon, S. Samrah, H. Shikata, J. Tschirren, K. Palagyi, K. C. Beck, and G. McLennan, "Characterization of the interstitial lung diseases via density-based and texture-based analysis of computed tomography images of lung structure and function," *Acad Radiol,* vol. 10, pp. 1104-18, Oct 2003.

[18] A. Rosenfeld, "Fuzzy digital topology," *Information and Control,* vol. 40, pp. 76--87, 1979.

[19] A. Rosenfeld, "The fuzzy geometry of image subsets," *Pattern Recognition Letters,* vol. 2, pp. 311-317, 1984.

[20] J. K. Udupa and S. Samarasekera, "Fuzzy connectedness and object definition: theory, algorithms, and applications in image segmentation," *Graphical Models and Image Processing,* vol. 58, pp. 246-261, 1996.

[21] D. Marr, *Vision*. San Francisco, CA: W. H. Freeman and Company, 1982.

[22] A. P. Witkin, "Scale-space filtering," presented at the 8th International Joint Conference Artificial Intelligence, Karlsruhe, West Germany, 1983.

[23] J. J. Koenderink, "The structure of images," *Biological Cybernatics,* vol. 50, pp. 363-370, 1984.

[24] T. Lindeberg, "Scale-space for discrete signals," *IEEE Transactions on Pattern Recognition and Machine Intelligence,* vol. 12, pp. 234-254, 1990.

[25] K. L. Vincken, A. S. E. Koster, and M. A. Viergever, "Probabilistic multiscale image segmentation," *IEEE Transactions on Pattern Analysis and Machine Intelligence,* vol. 19, pp. 109-120, 1997.

[26] Y. Leung, J. S. Zhang, and Z. B. Xu, "Clustering by scale space filtering," *IEEE Transactions on Pattern Analysis and Machine Intelligence,* vol. 22, pp. 1396-1410, 2000.

[27] B. C. Lovell and A. P. Bradley, "The multiscale classifier," *IEEE Transactions on Pattern Analysis and Machine Intelligence,* vol. 18, pp. 124-137, 1996.

[28] M. Ferraro, G. Bocclgnone, and T. Caell, "On the representation of image structures via scale space entropy conditions," *IEEE Transactions on Pattern Analysis and Machine Intelligence,* vol. 21, pp. 1190-1203, 1999.

[29] J. Weickert, *Anisotropic Diffusion in Image Processing*. Stuttgart, Germany: ECMI Series, Teubner-Verlag, 1998.

[30] B. Burgeth, M. Breuß, L. Pizarro, and J. Weickert, "PDE-driven adaptive morphology for matrix fields," in *Scale Space and Variational Methods in Computer Vision, Lecture Notes in Computer Science*, Berlin, 2009, pp. 247-258.

[31] P. K. Saha and J. K. Udupa, "Tensor scale-based fuzzy connectedness image segmentation," in *SPIE: Medical Imaging*, San Diego, CA, 2003, pp. 1580-1590.

[32] P. K. Saha, J. C. Gee, Z. Xie, and J. K. Udupa, "Tensor scale-based image registration," in *SPIE: Medical Imaging*, San Diego, CA, 2003, pp. 743-753.

[33] P. K. Saha and F. W. Wehrli, "A robust method for measuring trabecular bone orientation anisotropy at in vivo resolution using tensor scale," *Pattern Recognition*, vol. 37, pp. 1935-1944, 2004.

[34] P. K. Saha and F. W. Wehrli, "In vivo assessment of trabecular bone architecture via three-dimensional tensor scale," in *SPIE: Medical Imaging*, San Diego, CA, 2004, pp. 750-760.

[35] F. A. Andalo, P. A. V. Miranda, R. d. S. Torres, and A. X. Falcao, "A new shape descriptor based on tensor scale," in *the 8th International Symposium on Mathematical Morphology*, Rio de Janeiro, Brazil, 2007, pp. 141–152.

[36] F. A. Andalo, P. A. V. Miranda, R. d. S. Torres, and A. X. Falcao, "Detecting contour saliences using tensor scale," presented at the IEEE International Conference on Image Processing, 2007.

[37] M. P. d. Carmo, *Differential geometry of curves and surfaces*. Englewood Cliffs, N.J.: Prentice-Hall, 1976.

[38] L. A. Riggs, "Curvature Detectors in Human Vision," *Science*, vol. 184, pp. 1200-1201, 1974.

[39] P. Parent and S. W. Zucker, "Trace Inference, Curvature Consistency, and Curve Detection," *IEEE Transactions On Pattern Analysis And Machine Intelligence*, vol. 11, pp. 823-839, Aug 1989.

[40] N. Kehtarnavaz and R. J. P. Defigueiredo, "A 3-D Contour Segmentation Scheme Based on Curvature and Torsion," *IEEE Transactions On Pattern Analysis And Machine Intelligence*, vol. 10, pp. 707-713, Sep 1988.

[41] E. Trucco and R. B. Fisher, "Experiments in Curvature-Based Segmentation of Range Data," *IEEE Transactions On Pattern Analysis And Machine Intelligence*, vol. 17, pp. 177-182, Feb 1995.

[42] F. Zana and J. C. Klein, "Segmentation of vessel-like patterns using mathematical morphology and curvature evaluation," *IEEE Transactions on Image Processing*, vol. 10, pp. 1010-1019, Jul 2001.

[43] O. Soldea, G. Elber, and E. Rivlin, "Global segmentation and curvature analysis of volumetric data sets using trivariate B-spline functions," *IEEE Transactions On Pattern Analysis And Machine Intelligence*, vol. 28, pp. 265-278, Feb 2006.

[44] E. K. Hodson, D. R. Thayer, and C. Franklin, "Adaptive Gaussian Filtering and Local Frequency Estimates Using Local Curvature Analysis," *IEEE Transactions on Acoustics Speech and Signal Processing,* vol. 29, pp. 854-859, 1981.

[45] A. I. ElFallah and G. E. Ford, "Mean curvature evolution and surface area scaling in image filtering," *IEEE Transactions on Image Processing,* vol. 6, pp. 750-753, May 1997.

[46] B. E. Chapman and D. L. Parker, "3D multi-scale vessel enhancement filtering based on curvature measurements: application to time-of-flight MRA," *Medical Image Analysis,* vol. 9, pp. 191-208, Jun 2005.

[47] D. B. Goldgof, T. S. Huang, and L. Hua, "A Curvature-Based Approach to Terrain Recognition," *IEEE Transactions On Pattern Analysis And Machine Intelligence,* vol. 11, pp. 1213-1217, Nov 1989.

[48] F. Mokhtarian, "Silhouette-Based Isolated Object Recognition through Curvature Scale-Space," *IEEE Transactions On Pattern Analysis And Machine Intelligence,* vol. 17, pp. 539-544, May 1995.

[49] M. Shi, Y. Fujisawa, T. Wakabayashi, and F. Kimura, "Handwritten numeral recognition using gradient and curvature of gray scale image," *Pattern Recognition,* vol. 35, pp. 2051-2059, Oct 2002.

[50] E. M. Friets, J. W. Strohbehn, and D. W. Roberts, "Curvature-Based Nonfiducial Registration for the Frameless Stereotaxic Operating Microscope," *IEEE Transactions on Biomedical Engineering,* vol. 42, pp. 867-878, Sep 1995.

[51] B. Fischer and J. Modersitzki, "Curvature based image registration," *Journal of Mathematical Imaging and Vision,* vol. 18, pp. 81-85, Jan 2003.

[52] P. J. Besl and R. C. Jain, "Invariant surface characteristics for 3D object recognition in range images," *Comput. Vision Graph. Image Process.,* vol. 33, pp. 33-80, 1986.

[53] F. P. Ferrie and M. D. Levine, "Deriving coarse 3D models of objects," in *Computer Vision and Pattern Recognition,* Ann Arbor, MI , USA 1988, pp. 345 - 353

[54] B. C. Vemuri, A. Mitiche, and J. K. Aggarwal, "Curvature-based representation of objects from range data " *Image and Vision Computing,* vol. 4, pp. 107-114 1986.

[55] P. J. Flynn and A. K. Jain, "On reliable curvature estimation," in *Computer Vision and Pattern Recognition, 1989. Proceedings CVPR '89., IEEE Computer Society Conference on,* 1989, pp. 110-116.

[56] G. Taubin, "Estimating the tensor of curvature of a surface from a polyhedral approximation," presented at the Proceedings of the Fifth International Conference on Computer Vision, 1995.

[57] T. Chi-Keung and G. Medioni, "Curvature-augmented tensor voting for shape inference from noisy 3D data," *Pattern Analysis and Machine Intelligence, IEEE Transactions on,* vol. 24, pp. 858-864, 2002.

[58] M. Unser, A. Aldroubi, and M. Eden, "Fast B-spline Transforms for Continuous Image Representation and Interpolation," *IEEE Transactions on Pattern Analysis and Machine Intelligence,* vol. 13, pp. 277-285, 1991.

[59] T. M. Lehmann, C. Gonner, and K. Spitzer, "Survey: interpolation methods in medical image processing," *IEEE Transactions on Medical Imaging,* vol. 18, pp. 1049 -1075, 1999.

[60] G. J. Grevera and J. K. Udupa, "An objective comparison of 3-D image interpolation methods," *IEEE Transactions on Medical Imaging,* vol. 17, pp. 642 -652, 1998.

[61] G. T. Herman, S. W. Rowland, and M.-M. Yau, "A comparative study of the use of linear and modified cubic spline interpolation for image reconstruction," *IEEE Transactions on Nuclear Science,* vol. 26, pp. 2879-2894, 1979.

[62] M. R. Stytz and R. W. Parrott, "Using Kriging for 3d Medical Imaging," *Computerized Medical Imaging and Graphics,* vol. 17, pp. 421-442, Nov-Dec 1993.

[63] S. P. Raya and J. K. Udupa, "Shape-based interpolation of multidimensional objects," *IEEE Transactions on Medical Imaging,* vol. 9, pp. 32-42, 1990.

[64] G. T. Herman, J. Zheng, and C. A. Bucholtz, "Shape-based interpolation," *IEEE Computer Graphics and Applications,* vol. 12, pp. 69-79, 1992.

[65] W. E. Higgins, C. Morice, and E. L. Ritman, "Shape-Based Interpolation of Tree-Like Structures in 3-Dimensional Images," *IEEE Transactions On Medical Imaging,* vol. 12, pp. 439-450, Sep 1993.

[66] G. J. Grevera and J. K. Udupa, "Shape-based interpolation of multidimensional grey-level images," *IEEE Transactions on Medical Imaging,* vol. 15, pp. 881 -892, 1996.

[67] T. Y. Lee and C. H. Lin, "Feature-guided shape-based image interpolation," *IEEE Transactions On Medical Imaging,* vol. 21, pp. 1479-1489, Dec 2002.

[68] T.-Y. Lee and W.-H. Wang, "Morphology-based three-dimensional interpolation," *IEEE Transactions on Medical Imaging,* vol. 19, pp. 711-721, 2000.

[69] G. P. Penney, J. A. Schnabel, D. Rueckert, M. A. Viergever, and W. J. Niessen, "Registration-based interpolation," *IEEE Transactions On Medical Imaging,* vol. 23, pp. 922-926, Jul 2004.

[70] G. Gerig, O. Kubler, R. Kikinis, and F. A. Jolesz, "Nonlinear Anisotropic Filtering of Mri Data," *IEEE Transactions On Medical Imaging,* vol. 11, pp. 221-232, Jun 1992.

[71] D.-S. Luo, M. A. King, and S. J. Glick, "Local geometry variable conductance diffusion for post-reconstruction filtering," in *Nuclear Science Symposium and Medical Imaging Conference, 1993., 1993 IEEE Conference Record.*, 1993, pp. 1667-1671 vol.3.

[72] G. Sapiro and D. L. Ringach, "Anisotropic diffusion of multivalued images with applications to color filtering," *IEEE Transactions on Image Processing,* vol. 5, pp. 1582-1586, Nov 1996.

[73] G. J. M. Parker and J. A. Schnabel, "Enhancement of anisotropic diffusive filtering using approximate entropy," in *International Society of Magnetic Resonance in Medicine,* Philadelphia, PA, 1999, p. 175.

[74] J. Weickert, "Coherence-enhancing diffusion filtering," *International Journal of Computer Vision,* vol. 31, pp. 111-127, Apr 1999.

[75] A. S. Frangakis, A. Stoschek, and R. Hegerl, "Wavelet transform filtering and nonlinear anisotropic diffusion assessed for signal reconstruction performance on multidimensional biomedical data," *IEEE Transactions on Biomedical Engineering,* vol. 48, pp. 213-222, Feb 2001.

[76] G. E. Ford, "Space scale analysis for image sampling and interpolation," in *IEEE International Conference on Acoustics Speech and Signal Processing*, 1992, pp. 165-168.

[77] M. M. Orkisz, C. Bresson, I. E. Magnin, O. Champin, and P. C. Douek, "Improved vessel visualization in MR angiography by nonlinear anisotropic filtering," *Magnetic Resonance in Medicine,* vol. 37, pp. 914-919, Jun 1997.

[78] Y. L. You and M. Kaveh, "Blind image restoration by anisotropic regularization," *IEEE Transactions on Image Processing,* vol. 8, pp. 396-407, Mar 1999.

[79] L. Atzori, G. B. De Natale, and F. Granelli, "Adaptive anisotropic filtering (AAF) for real-time visual enhancement of MPEG-Coded video sequences," *IEEE Transactions on Circuits and Systems for Video Technology,* vol. 12, pp. 285-298, May 2002.

[80] O. Demirkaya, "Anisotropic diffusion filtering of PET attenuation data to improve emission images," *Physics in Medicine and Biology,* vol. 47, pp. N271-N278, Oct 21 2002.

[81] B. H. Miao, R. Jeraj, S. L. Bao, and T. R. Mackie, "Adaptive anisotropic diffusion filtering of Monte Carlo dose distributions," *Physics in Medicine and Biology,* vol. 48, pp. 2767-2781, Sep 7 2003.

[82] Y. J. Yu and S. T. Acton, "Speckle reducing anisotropic diffusion," *IEEE Transactions on Image Processing,* vol. 11, pp. 1260-1270, Nov 2002.

[83] M. Aleman-Flores, L. Alvarez, and V. Caselles, "Texture-oriented anisotropic filtering and geodesic active contours in breast tumor ultrasound segmentation," *Journal of Mathematical Imaging and Vision,* vol. 28, pp. 81-97, May 2007.

[84] K. Krissian and S. Aja-Fernandez, "Noise-Driven Anisotropic Diffusion Filtering of MRI," *IEEE Transactions on Image Processing,* vol. 18, pp. 2265-2274, Oct 2009.

[85] Q. Xu, A. W. Anderson, J. C. Gore, and Z. H. Ding, "Efficient anisotropic filtering of diffusion tensor images," *Magnetic Resonance Imaging,* vol. 28, pp. 200-211, Feb 2010.

[86] I. C. Rodrigues and J. M. R. Sanches, "Convex Total Variation Denoising of Poisson Fluorescence Confocal Images With Anisotropic Filtering," *IEEE Transactions on Image Processing,* vol. 20, pp. 146-160, Jan 2011.

[87] C. Johnson, R. MacLeod, and J. Schmidt, "Software tools for modeling, computation, and visualization in medicine," in *Comp Med 94*, 1995.

[88] M. Kass, A. Witkin, and D. Terzopoulos, "Snakes: active contour models," *International Journal of Computer Vision,* vol. 1, pp. 321-331, 1988.

[89] A. X. Falcão, J. K. Udupa, S. Samarasekera, and S. Sharma, "User-steered image segmentation paradigms: live wire and live lane," *Graphical Models and Image Processing,* vol. 60, pp. 233-260, 1998.

[90] J. K. Udupa, P. K. Saha, and R. A. Lotufo, "Relative fuzzy connectedness and object definition: theory, algorithms, and applications in image segmentation," *IEEE Transactions on Pattern Analysis and Machine Intelligence,* vol. 24, pp. 1485-1500, 2002.

[91] T. F. Cootes, C. J. Taylor, D. Cooper, and J. Graham, "Active shape models - their training and application," *Computer Vision and Image Understanding,* vol. 61, pp. 38-59, 1995.

[92] T. F. Cootes, G. J. Edwards, and C. J. Taylor, "Active appearance models," presented at the European Conference on Computer Vision, 1998.

[93] J. J. Buckley and E. Eslami, "Fuzzy plane geometry I: Points and lines," *Fuzzy Sets and Systems,* vol. 86, pp. 179-187, 1997.

[94] S. Dellepiane, F. Fontana, and G. L. Vernazza, "Nonlinear image labeling for multivalued segmentation," *IEEE Transactions on Image Processing,* vol. 5, pp. 429-446, 1996.

[95] S. Dellepiane and F. Fontana, "Extraction of intensity connectedness for image processing," *Pattern Recognition Letters,* vol. 16, pp. 313--324, 1995.

[96] P. K. Saha and J. K. Udupa, "Relative fuzzy connectedness among multiple objects: theory, algorithms, and applications in image segmentation," *Computer Vision and Image Understanding,* vol. 82, pp. 42-56, 2001.

[97] P. K. Saha and J. K. Udupa, "Iterative relative fuzzy connectedness and object definition: theory, algorithms, and applications in image segmentation," in *IEEE Workshop on Mathematical Methods in Biomedical Image Analysis*, Hilton Head, South Carolina, 2000.

[98] P. K. Saha and J. K. Udupa, "Fuzzy connected object delineation: axiomatic path strength definition and the case of multiple seeds," *Computer Vision and Image Understanding,* vol. 83, pp. 275-295, 2001.

[99] G. T. Herman and B. M. Carvalho, "Multiseeded segmentation using fuzzy connectedness," *IEEE Transactions on Pattern Analysis and Machine Intelligence,* vol. 23, pp. 460-474, 2001.

[100] B. M. Carvalho, C. J. Gau, G. T. Herman, and T. Y. Kong, "Algorithms for fuzzy segmentation," *Pattern Analysis and Applications,* vol. 2, pp. 73-81, 1999.

[101] L. G. Nyúl, A. X. Falcão, and J. K. Udupa, "Fuzzy-connected 3D image segmentation at interactive speeds," *Graphical Models and Image Processing,* vol. 64, pp. 259-281, 2003.

[102] S. Samarasekera, J. K. Udupa, Y. Miki, and R. I. Grossman, "A new computer-assisted method for enhancing lesion quantification in multiple sclerosis," *Journal of Computer Assisted Tomography,* vol. 21, pp. 145--151, 1997.

[103] J. K. Udupa, L. Wei, S. Samarasekera, Y. Miki, M. A. v. Buchem, and R. I. Grossman, "Multiple sclerosis lesion quantification using fuzzy connectedness principles," *IEEE Transactions on Medical Imaging,* vol. 16, pp. 598--609, 1997.

[104] Y. Miki, R. I. Grossman, J. K. Udupa, M. A. v. Buchem, L. Wei, M. D. Philips, U. Patel, J. C. McGown, and D. L. Kolson, "Differences between relapsing remitting and chronic progressive multiple sclerosis as determined with quantitative MR imaging," *Radiology,* vol. 210, pp. 769-774, 1999.

[105] Y. Miki, R. I. Grossman, J. K. Udupa, L. Wei, M. Polansky, L. Mannon, and D. L. Kolson, "Relapsing-remitting multiple sclerosis: longitudinal analysis of MR images - lack of correlation between changes in T2 lesion volume and clinical findings," *Radiology,* vol. 213, pp. 395-399, 1999.

[106] Y. Ge, R. Grossman, J. K. Udupa, L.Wei, L. Mannon, M. Polansky, and D. L. Kolson, "Brain atropy in relapsing-remitting multiple sclerosis and secondary progressive multiple sclerosis: longitudinal quantitative analysis," *Radiology,* vol. 214, pp. 665-670, 2000.

[107] R. He and P. A. Narayana, "Automatic delineation of Gd enhancements on magnetic resonance images in multiple sclerosis," *Medical Physics,* vol. 29, pp. 1536-1546, 2002.

[108] A. Kumar, W. Bilker, Z. Jin, J. K. Udupa, and G. Gottlieb, "Age of onset of depression and quantitative neuroanatomic measures: absence of specific correlations," *Psych. Res. Neuroimag.,* vol. 91, pp. 101-110, 1999.

[109] A. Kumar, W. Bilker, Z. Jin, and J. K. Udupa, "Atropy and high intensity lesions: complementary neurobiological mechanisms in late-life major depression," *Neuropsychopharmacology,* vol. 22, pp. 264-274, 2000.

[110] T. Lei, J. K. Udupa, P. K. Saha, and D. Odhner, "Artery-vein separation via MRA - an image processing approach," *IEEE Transactions on Medical Imaging,* vol. 20, pp. 689-703, 2001.

[111] B. L. Rice(Jr.) and J. K. Udupa, "Clutter-free volume rendering for magnetic resonance angiography using fuzzy connectedness," *International Journal of Imaging Systems and Technology,* vol. 11, pp. 62--70, 2000.

[112] J. M. Abrahams, P. K. Saha, R. W. Hurst, P. D. LeRous, and J. K. Udupa, "Three dimensional bone-free rendering of the crebral circulation using computed tomographic angiography and fuzzy connectedness," *Neurosurgery,* vol. 51, pp. 264-269, 2002.

[113] P. K. Saha, J. K. Udupa, and J. M. Abrahams, "Automatic bone-free rendering of cerebral aneurysms via 3D-CTA," in *SPIE: Medical Imaging*, San Diego, CA, 2001, pp. 1264-1273.

[114] P. K. Saha, J. K. Udupa, E. F. Conant, D. P. Chakraborty, and D. Sullivan, "Breast tissue glandularity quantification via digitized mammograms," *IEEE Transactions on Medical Imaging,* vol. 20, pp. 792-803, 2001.

[115] J. Canny, "A computational approach to edge detection," *IEEE Transactions on Pattern Analysis and Machine Intelligence,* vol. 8, pp. 679-698, 1986.

[116] R. Medina-Carnicer, R.Munoz-Salinas, E.Yeguas-Bolivar, and L.Diaz-Mas, "A novel method to look for the hysteresis thresholds for the Canny edge detector," *Pattern Recognition,* vol. 44, pp. 1201-1211, 2011.

[117] P. K. Saha, B. Das, and F. W. Wehrli, "An object class-uncertainty induced adaptive force and its application to a new hybrid snake," *Pattern Recognition,* vol. 40, pp. 2656-2671, 2007.

[118] P. K. Saha, F. W. Wehrli, and B. R. Gomberg, "Fuzzy distance transform: theory, algorithms, and applications," *Computer Vision and Image Understanding,* vol. 86, pp. 171-190, 2002.

[119] G. J. Grevera, "The dead reckoning signed distance transform," *Computer Vision Image Understanding,* vol. 95, pp. 317-333, 2004.

[120] G. P. Penny, J. A. Schnable, D. Rueckert, M. A. Viergever, and W.J.Niessen, "Registration-based interpolation," *IEEE Transactions on Medical Imaging,* vol. 23, pp. 922-926, 2004.

[121] L. Ibanez and W. Schroeder, *The ITK Software Guide*: Kitware, Inc. , 2005.

[122] G. Gerig, O. Kubler, R. Kikinis, and F. A. Jolesz, "Nonlinear anisotropic filtering of MRI data," *IEEE Transactions on Medical Imaging,* vol. 11, pp. 221-232, 1992.

[123] R. C. Gonzalez and P. Wintz, *Digital Image Processing*. Reading, MA: Addison-Wesley, 1987.

[124] A. Kaufmann, *Introduction to the Theory of Fuzzy Subsets* vol. 1. New York: Academic Press, 1975.

[125] Y. Sato, S. Nakajima, H. Atsumi, T. Koller, G. Gerig, S. Yoshida, and R. Kikinis, "3D multi-scale line filter for segmentation and visualization of curvilinear structures in medical images," *Cvrmed-Mrcas'97,* vol. 1205, pp. 213-222, 1997.

[126] A. F. Frangi, W. J. Niessen, K. L. Vincken, and M. A. Viergever, "Multiscale vessel enhancement filtering," *Medical Image Computing and Computer-Assisted Intervention - Miccai'98,* vol. 1496, pp. 130-137, 1998.

[127] H. Shikata, E. A. Hoffman, and M. Sonka, "Automated segmentation of pulmonary vascular tree from 3D CT images," in *SPIE: Medical Imaging*, San Diego, CA, 2004, pp. 107-116.

[128] P. K. Saha, Z. Gao, S. K. Alford, M. Sonka, and E. A. Hoffman, "Topomorphologic separation of fused isointensity objects via multiscale opening: separating arteries and veins in 3-D pulmonary CT," *IEEE Transactions on Medical Imaging*, vol. 29, 2010.